Synthesis and Characterization of BNT based Magnetoelectric Composites

A

Ph.D. Thesis

Submitted for the award of the degree of

Doctor of Philosophy

By
Parminder Singh
(Registration No. 901812011)

Under the supervision of

Dr. Jayant Kolte
Assistant Professor
TIET, Patiala

Dr. Puneet Sharma
Professor & Dean Sciences
IILM University, Greater Noida

Department of Physics & Materials Science
Thapar Institute of Engineering & Technology, Patiala
Punjab-147004

February 2024

Table of Contents

Dedicated to my parents

CERTIFICATE

This is to certify that the thesis entitled **"Synthesis and Characterization of BNT based Magnetoelectric Composites"** which is being submitted by Parminder Singh in the fulfilment of the requirement for the award of the degree Doctor of Philosophy in the Department of Physics & Materials Science, Thapar Institute of Engineering & Technology (TIET), is an authentic record of candidate's own work carried out by him under our supervision and guidance. The matter presented in this thesis has not been submitted in part or full for the award of any degree in any other University or Institute.

Date: 26/02/24

Place: Patiala

Dr. Jayant Kolte
Assistant Professor
Department of Physics & Materials Science
Thapar Institute of Engineering & Technology
Patiala -147004, India

Dr. Puneet Sharma
Professor & Dean of Sciences
IILM University
Greater Noida - 201306, India

Acknowledgement

"We should always pause to express gratitude to those whose presence and actions leave an indelible mark on our journey."

First and foremost, I would like to express my sincere gratitude to my both supervisors, **Dr. Jayant Kolte** (Assistant Professor, Thapar Institute of Engineering and Technology, Patiala) and **Dr. Puneet Sharma** (Professor & Dean Sciences, IILM University, Greater Noida) for their unconditional support, patience, motivation, enthusiasm, and vast knowledge. Their advice was invaluable throughout my thesis research and writing. This thesis would not have been possible without their skilled supervision. I will be eternally grateful to them for their continuous support.

I wish to express my sincere appreciation to **Dr. Kulvir Singh** (Head, Department of Physics & Materials Science, Thapar Institute of Engineering & Technology, Patiala). His invaluable support in making all the essential departmental facilities available is deeply acknowledged. I also want to extend my heartfelt gratitude to my doctoral committee members (**Dr. Bhupendra Kumar Chudasama**, **Dr. Bhaskar Chandra Mohanty** and **Dr. Bonamali Pal)** and the entire faculty of DPMS for their unwavering support and encouragement throughout my journey. I also would like to acknowledge **Dr. Manoj Kumar Sharma**, **Dr. Prabal P. Singh Bhadauria** and **Dr. Sanjay Kashyap** for their exceptional guidance and assistance.

I am thankful to my seniors **Dr. Anoop Pratap Singh, Dr. Chhavi Pahwa, Dr. Santhoshkumar Mahadevan**, **Dr. Shivani Jindal** and labmates **Ms. Neha Thakur, Ms. Sonal Singh, Ms. Taranveer Kaur, Ms. Anupriya Chaudhary, Mr. Raj Ankit Pandey, Ms. Aditi Sharma, Mr. Anurag Kamboj, Ms. Pretty Singla and Ms. Jahnvi Goel.** My special thanks to **Ms. Aditi Sharma** for her kind support in experimental activities during my research.

I would like to thank MCF Lab, Thapar Institute of Engineering & Technology for XRD, FE-SEM, RAMAN and Multiferroic facility.

I am grateful to all non-teaching staff of Department of Physics & Materials Science who never turn me down whenever I approached for any help.

I gratefully acknowledge the Defence Research and Development Organization (DRDO) (grant no. ERIP/ER/201709007/M/01/1731) for the financial support in the form of Junior Research Fellow (JRF) and Senior Research Fellow (SRF).

I would like to convey my sincere gratitude to my friends **Dr. Manish Kumar Singla, Dr. Surbhi Sharma, Dr. Aanchal Rathi, Geetika Bansal, Aayushi Kundu, Mohit Dhuria, Ankush Sharma, Shelly Singla and Pritam Haith** for creating cheerful atmosphere during my stay. I would like to express my profound gratitude to **Dr. Neeraj** for the exceptional kindness and unwavering moral support that she extended to me throughout the journey. Her consistent encouragement and guidance were invaluable, especially during challenging times, serving as a constant source of strength. Her steadfast belief in me significantly contributed to my resilience and determination to overcome obstacles.

Most of all, I would like to thank my parents **(Sh. Hardev Singh and Smt. Ritu Devi)** for their love, moral support and inconvenience experienced by them during my study. Special thanks to my brother **Davinder Singh** and sister-in-law **Tanu** who have always been a source of incessant support. A heartfelt expression of gratitude to my nephew, **Shiva Thakur**, whose presence has the remarkable ability to dispel the negativity around me.

And above all, I pay my profound gratitude to The Almighty GOD for giving me strength, love and blessings.

Parminder Singh

List of Figures

List of Tables

List of Symbols

α_E or α_{ME}	Direct magnetoelectric coupling coefficient
α_H	Converse magnetoelectric coupling coefficient
d_{33}	Direct piezoelectric coefficient
d_{33}^*	Converse piezoelectric coefficient
P_r	Remanent polarization
P_s	Saturation polarization
E_c	Coercive electric field
P	Polarization
E	Electric field
I	Polarization current
S	Electro-strain
J	Leakage current density
M	Magnetization
M_s	Saturation magnetization
H	Magnetic field
H_{ac}	AC magnetic field
H_{dc}	DC magnetic field
q_s	Piezomagnetic coefficient
λ_s	Magnetostrictive coefficient
ε_r	Dielectric constant
f	Frequency
f_r	Resonant frequency
tanδ	Dielectric loss
μ	Permeability
μ_i	Initial permeability
μ_B	Bohr's magneton
t	Thickness
V_{out}	Output voltage

Abbreviations used

P-E	Polarization *vs* Electric field
S-E	Electro-strain *vs* Electric field
J-E	Leakage current density *vs* Electric field
M-H	Magnetization *vs* Magnetic field
XRD	X-ray diffraction
SEM	Scanning electron microscope
ME	Magnetoelectric
PE	Piezoelectric
FE	Ferroelectric
PM	Piezomagnetic
FM	Ferromagnetic
VSM	Vibrating sample magnetometer
Hz	Hertz
nm	nanometer
cm	centimeter
RT	Room temperature
dM^2/dH	Qualitative piezomagnetic coefficient
BNT	$Bi_{0.5}Na_{0.5}TiO_3$
BKT	$Bi_{0.5}K_{0.5}TiO_3$
BMT	$BiMg_{0.5}Ti_{0.5}O_3$
BNKMT	72.5BNT-22.5BKT-5BMT
NFO	$NiFe_2O_4$
CFO	$CoFe_2O_4$
MFO	$MgFe_2O_4$
NZ_xFO	Zn substituted NFO
FWHM	Full width at half maxima
0-3 composite	Particulate composite
2-2 composite	Laminate composite

Preface

The magnetoelectric (*ME*) composites has gained great deal of attention over to single phase multiferroics due to its strain mediated coupling between piezoelectric and magnetostrictive phases. Such composites with high coupling have paved the way for practical device application in meRAMs, sensors, and low frequency energy harvesters etc. The resultant *ME* coupling depends upon the type of magnetic and piezoelectric phase, their relative fraction, and type of geometry. Amongst lead-free piezoelectric materials, BNT-based ternary solid-solution, i.e., $72.5Bi_{0.5}Na_{0.5}TiO_3$-$22.5Bi_{0.5}K_{0.5}TiO_3$-$5BiMg_{0.5}Ti_{0.5}O_3$ (BNKMT) is prominent due to its excellent piezoelectric coefficient. On the other hand, $NiFe_2O_4$ or $Ni_{1-x}Zn_xFe_2O_4$ (x = 0 - 0.5) exhibit high piezomagnetism. Therefore, in this work, the main focus is to study the influence of relative weight fraction and geometry on the magnetoelectric coupling of their composites. The work is organized into seven chapter, where the content of each chapter is shown below.

Chapter 1 (Introduction): This chapter provides a concise introduction about magnetoelectric (*ME*) properties in multiferroic materials. Further, an overview of *ME* coupling in single-phase multiferroics and composites is given. Some basic definitions and terminology used in the thesis are given along with their important role in *ME* properties are discussed. The factors that influence the *ME* coupling in composites are discussed in detail. At last, applications of *ME* composites in several areas are highlighted.

Chapter 2 (Literature review): This chapter is mainly focused on the factors that have influence on the *ME* coupling of composites. Initially, the impact of substitution and doping on the BNT-based solid solutions is reviewed followed by the effect of substitution on magnetostrictive phase. The *ME* coupling in particulate and laminates has been discussed. The effect of phase fraction and applied *f* of *H* on *ME* coupling among particulates and laminates is also presented. Based on these studies, the literature gap is discussed followed by the objectives for the research work.

Chapter 3 (Experimental and characterization techniques): This chapter includes the synthesis method for developing PE phases (BNT and BNKMT), magnetostrictive phases (NZ_xFO) and their 0-3 and 2-2 composites. A brief detail of novel direct diffusion bonding technique is given for synthesizing 2-2 composite. Further, several material characterization techniques have been explained in the final section of this chapter.

Chapter 4 (Results and discussion: Pure Phases): In this chapter, the synthesis and optimization of both PE and magnetostrictive are discussed. This chapter is categorized into four sections. In first two sections, the effect of sintering temperature on the structural and electrical properties of PE BNT and BNKMT phases has been investigated. In the third section, the influence of sintering temperature on the structural and magnetic properties of NFO is presented. In the last section, effect of Zn substitution on the magnetic properties of the optimized NFO has been discussed.

Chapter 5 (Results and discussion: Magnetoelectric 0-3 composites): In this chapter, the phase, structural, electrical, magnetic and *ME* properties of 0-3 composites has been investigated. The chapter is divided into four sections. In the first section, the *ME* coupling in (1-*x*)BNT-*x*NFO composites are examined. Second section is focused on the *ME* coupling of (1-*x*)BNKMT-*x*NFO composite. These two sections demonstrate the effect of PE phase on *ME* coupling. In third section, the effect of magnetostrictive phase on the *ME* coupling has been studied by varying Zn substitution in NFO coupled with BNKMT in a fixed weight proportion, i.e., explore the *ME* coupling in 0.8BNKMT-0.2NZ_xFO composite. The last section emphasizes on the *ME* coupling based on the suitable PE (BNKMT) and magnetostrictive ($NZ_{0.3}$FO) in variation of relative weight fraction.

Chapter 6 (Results and discussion: Magnetoelectric 2-2 composites): In this chapter, the structural, FE, magnetic and *ME* properties of the laminate composite has been examined. The bilayer and trilayer laminate composites of BNKMT and $NZ_{0.3}$FO are synthesized via novel direct diffusion bonding technique.

Chapter 7 (Conclusions): A summary of the results from the diverse experiments discussed in the previous chapters are presented in this chapter. Initially, the effect of varying relative weight fraction on *ME* coupling in 0-3 composites is outlined. The impact of bilayer and trilayer laminates on the *ME* coupling has been concluded. At the end, the potential avenues for further research are discussed in the future scope section.

Chapter 1

Introduction

Overview

This chapter provides a concise introduction about magnetoelectric (*ME*) properties in multiferroic materials. Further, an overview of *ME* coupling in single-phase multiferroics and composites is given. Some basic definitions and terminology used in the thesis are given along with their important role in *ME* properties are discussed. The factors that influence the *ME* coupling in composites are discussed in detail. At last, applications of *ME* composites in several areas are highlighted.

1.1 Multiferroics

Traditionally, humans have dependence on the easily accessible resources. Over the last two centuries, there has been an increasing demand for new materials which shows multifunctional properties. Considerable advancements have been made in the development of materials that are easy to fabricate and assemble in the complex devices. Currently, solid-state electronics is the foundation for various scientific disciplines, faces challenges in meeting its requirements using existing materials. Therefore, researchers are exploring entirely new types of multifunctional materials that has low power consumption and better performance.

Multiferroics are a group of materials that demonstrate a long-range order in at least two macroscopic properties viz., ferromagnetic (FM), ferroelectric (FE), ferroelastic (FEI), and ferrotoroidic (FT) ordering [1,2]. The first multiferroic material has been discovered by Pierre Curie in 1894 [3]. He observed the phenomenon of simultaneous ferromagnetism and ferroelectricity in certain crystals, which laid the foundation for the field of multiferroics. However, progress in the field remained limited for many years due to the scarcity of known examples. It gain popularity when Hans Schmid invented the term ‘multiferroic’ in 1994 in Ascona, enhancing Aizu's prior categorization of ferroic materials [4]. Multiferroic material often shows coupling between the electric and magnetic ordering and therefore exhibit change in polarization (*P*) with applied magnetic field (*H*) (termed as direct *ME* effect) or change in magnetization (*M*) with external electric field (*E*) (known as converse *ME* effect) [5,6]. It is important to note that a multiferroic material do not necessarily demonstrate the linear *ME* effect (e.g., hexagonal $YMnO_3$), and not all materials exhibiting the linear *ME* effect are considered multiferroic (e.g., Cr_2O_3) as shown in the schematic of **Figure 1.1**. The versatility of *ME* multiferroic materials enables the design of innovative electronic devices with various functionalities including sensors, transducers, energy harvesters and memory devices [7–9].

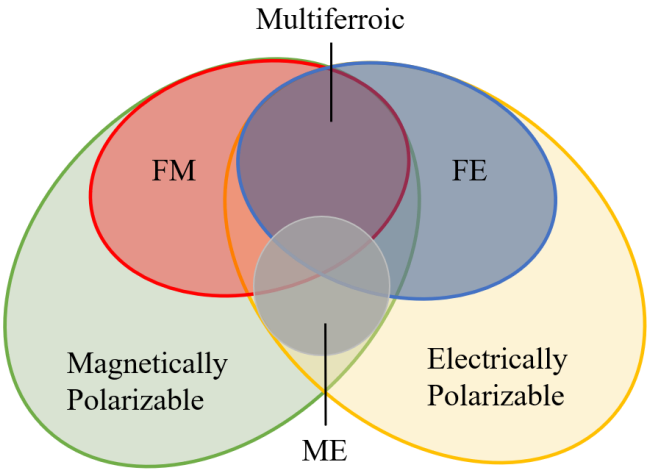

Figure 1.1. Schematic of *ME* effect demonstrating correlation with both electric and magnetic properties.

ME multiferroic materials are categorized into two types as single phase and composites and discussed in upcoming sub-sections.

1.1.1 Single phase multiferroics

Single phase multiferroics possess inherent *ME* effect due to simultaneous existence of magnetic and electric orders that are inextricably coupled [1]. $BiFeO_3$, $YMnO_3$, $DyFeO_3$, $LuFe_2O_4$ and $HoMnO_3$ are its few examples [1,2]. The *ME* coupling in such materials is weak at room temperature, which limit its use in practical devices. In single phase multiferroics, the FE and FM ordering simultaneously exists mostly below room temperature. The FE order typically arises from the displacement of ions, while the FM order originates from the alignment of magnetic moments. Achieving strong coupling between these two orders requires precise control of the crystal structure and symmetry, which is challenging to achieve in a single-phase.

1.1.2 ME Composites

ME composites are the multi-phase materials that consist of FE and FM phases [10,11]. In 1972, Van Suchtelen proposed that the *ME* effect recognized as a product tensor of the multiple orderings in the combination of two phases [12], i.e.,

$$\alpha_E = \frac{\textbf{Electric order}}{\textbf{Mechanical strain}} \times \frac{\textbf{Mechanical strain}}{\textbf{Magnetic order}} \tag{1.1}$$

$$\alpha_H = \frac{\textbf{Magnetic order}}{\textbf{Mechanical strain}} \times \frac{\textbf{Mechanical strain}}{\textbf{Electric order}} \tag{1.2}$$

where, α_E and α_H are the direct and converse *ME* coupling coefficient respectively. These equations demonstrate that the composites exhibit strain mediated (mechanical strain) *ME* coupling. In direct *ME* effect, the magnetic phase induces strain in an external *H* whereas in converse *ME* effect, electric phase exhibits strain in an applied electric field (*E*). Therefore, *ME* coupling in composites is extrinsic, which depends upon the type of FE or FM, relative phase fraction and connectivity between them [13–15]. The FE materials also possess PE property and FM material possess magnetostrictive property which is used to quantify *ME* coupling.

1.2 Piezoelectricity

FE materials are well-known for exhibiting piezoelectricity (i.e., induction of voltage in an applied stress or induction of strain in external *E*) [16]. The piezoelectricity arises from the non-centrosymmetry of crystal structure [17]. The non-centrosymmetry allows the displacement of positive and negative charges within the crystal lattice when mechanical stress or *E* is applied.

A typical hysteresis loop of FE material is shown in **Figure 1.2**. The electric domains of FE material are initially randomly oriented in an absence of external *E*. When an *E* is applied, they start to orient in the direction of an applied *E*. Above threshold *E* (E_{th}) limit, all domains are aligned themselves and exhibit saturation polarization (P_s). After the removal of *E*, the domains start randomizing but not retain their original orientation and therefore exhibit significant spontaneous *P* that termed as remanent polarization (P_r). The P_r determines the tendency of a FE material to exhibit direct piezoelectric (PE) effect which can be quantified by the piezoelectric charge coefficient d_{33} (generation of voltage in an applied stress). On the other hand, the switching rate of the domains depicts about the converse PE effect which is quantified by inverse piezoelectric charge coefficient d_{33}^* (induction of strain in external *E*). Thus, the switching of *P* with the applied stress or *E* is directly related to PE coefficients. This reversible nature enables them to produce an alternating electric charge in response to oscillating mechanical stress, making them ideal for applications such as sensors, actuators, and transducers [18]. The FE materials exhibit PE coefficients (d_{33} and d_{33}^*), which quantify their ability to convert mechanical energy into electrical energy or vice versa. These coefficients indicate the efficiency with which a material can generate an electric charge or strain in response to applied stress or *E* respectively. In order to achieve high α_E, the d_{33} of FE material should be high. The materials with ABO_3-perovskite structure exhibit high d_{33}.

The d_{33} is often used to assess the quality of piezoelectric material. The coefficient is related to three significant properties of materials in accordance to:

$$d_{33} = k_{33}*(\varepsilon_0 k_3^T S_{33}^T)^{1/2} \quad (1.3)$$

where k and ε_0 are the electro-mechanical coupling coefficient and absolute permittivity in free space respectively, whereas k_3^T denotes relative dielectric constant at a constant stress, and S_{33}^T is elastic compliance at fix E. It is important to note that significant values of the d_{33} are associated with substantial mechanical displacements, a quality often desired in motional transducer devices. In contrast, the charge accumulated on the electrodes can possibly read in terms of the applied mechanical stress. Specifically, the d_{33} arises when the force aligns with the three-direction (parallel to the polarization axis) and is exerted on the same surface from which the charge is gathered.

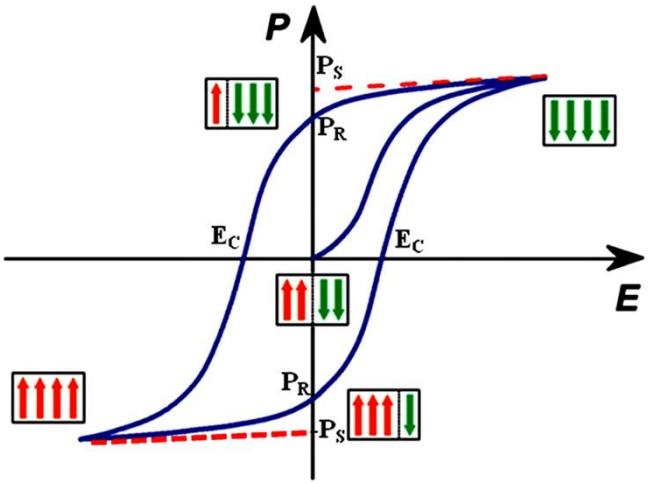

Figure 1.2. Typical hysteresis loop of FE material with their domains movement with external E [19].

1.3 Magnetostriction

The magnetostrictive materials are an intriguing class of materials that exhibit change in dimensions when subjected to external H [20]. The effect has been first observed by James Joule in 1842 when the change in dimensions of iron rod in an applied H is observed [21]. The term "magnetostriction" has been coined by Lord Kelvin in 1875 to describe this effect [22]. It has been observed that single crystals show stronger influence than the polycrystalline materials. Later in 19th century and earlier in 20th century, scientist Pierre Weiss and William Thomson developed theoretical models to explain the magnetostrictive behavior in such

materials [23]. They hypothesized that the change in dimensions is a consequence of the interaction between magnetic moments and lattice strain, which established the framework for understanding magnetostriction phenomenon.

In the 1970s, Terfenol-D, an alloy primarily composed of terbium, dysprosium, and iron has been fabricated, which exhibit remarkable magnetostriction coefficient, λ_s ~ 650 ppm [24]. However, there are some limitations with Terfenol-D, i.e., they are operable at high H (~ 30 kOe), composed of rare earth metals, has low electrical resistivity and costly [25]. These limitations restrict its use in low H operable devices. Further, these limitations are suppressed with the advancement of spinel ferrite. The spinel ferrites are the class of FM materials with chemical formula AB_2O_4, where A and B are metal cations [26,27]. The magnetostrictive characteristics in spinel ferrites have been traced in the early 20th century. However, it gained importance in 1940s during the World War-II to make acoustic devices [28]. After the World War, researchers made substantial efforts to improve its magnetostriction. These days, several techniques viz. doping, nano-structuring, and cations substitutions are adopted to further enhance their magnetostriction. It is noted that good *ME* coupling in composites requires high λ_s at low H for the magnetostrictive phase, which is determined by piezomagnetic coefficient (q_s) as

$$q_s = \frac{d\lambda}{dH} \tag{1.4}$$

As magnetostriction depicts the change in dimensions of the materials upon magnetization and its non-liner relationship can be expressed as

$$\lambda \propto M^2 \tag{1.5}$$

Therefore, q_s can be written as

$$q_s \propto \frac{dM^2}{dH} \tag{1.6}$$

So, it is possible to determine the trend of q_s *vs* H by examining the variation of dM^2/dH *vs* H. The dM^2/dH is also be referred as qualitative piezomagnetic coefficient.

1.4 Connectivity

The connectivity among the distinct phases of composite is a key factor that affects the *ME* coupling. The term "connectivity" emphasizes the inter-connections between various

components or phases of the composite. Usually, two types of connectivity are used for synthesizing *ME* composites as discussed in next subsections.

1.4.1 0-3 Connectivity

The 0-3 composites also refer to particulate composites. In such composites, piezoelectric phase is present in continuous form and magnetic phase is present in the form of discrete particles. In other words, one phase is dispersed in the continuous matrix of another phase as shown in **Figure 1.3**.

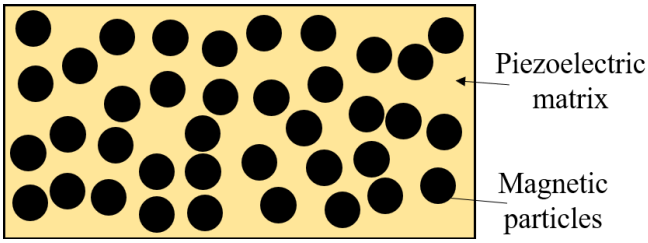

Figure 1.3. Schematic of 0-3 composite, where black sphere represents the magnetic particles that are embedded in the yellow color PE matrix.

1.4.2 2-2 Connectivity

The 2-2 composites are also termed as laminate composites as shown in **Figure 1.4**. The term "2-2 connectivity" indicates that there are two continuous phases in the composite, one represents the PE material and the other represents the magnetostrictive material. In this technique, one phase is stacked or laminated over another. These phases are arranged in a continuous manner throughout the composite, ensuring a direct and continuous path for both electrical and magnetic signals to propagate.

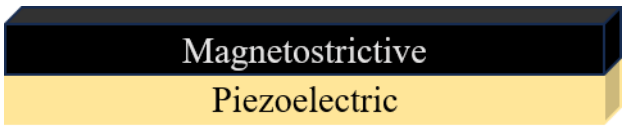

Figure 1.4. Schematic of 2-2 composite, where black color magnetostrictive layer is stacked over yellow colored PE layer.

The 2-2 composites exhibit relatively higher *ME* coupling than 0-3 composites, which is explained based on following factors:

a. **Improved interfacial bonding:** The alternating layers of PE and magnetostrictive materials in a laminate composite typically have better interfacial bonding compared to

particulate composites. This ensures efficient stress transfer between the layers, leading to enhanced magnetostrictive response when subjected to a magnetic field and improved PE response under mechanical stress.

b. **Alignment of domains:** In laminate composites, the alignment of domains in the PE and magnetostrictive layers can be optimized to ensure a more effective interaction between the two materials. This alignment facilitates the efficient transfer of stress or strain between the layers, further enhancing the overall *ME* coupling.
c. **Reduced stress concentrations:** Particulate composites may suffer from stress concentrations around the particles, which can limit the magnetostrictive response. In laminate composites, stress concentrations can be minimized due to the continuous and uniform distribution of the PE and magnetostrictive materials, resulting in more consistent and significant *ME* coupling.

By selecting appropriate PE and magnetostrictive materials with suitable properties, one can tailor the *ME* coupling in laminates for a particular application. This is hard to achieve in particulate composites, where the material properties are more challenging to control.

1.5 Applications

a. **Magnetic field sensors:** *ME* composites can be utilized to create highly sensitive magnetic field sensors. Changes in the magnetic field induces an electric field in the material, which can be detected and used for sensing applications. These sensors find applications in navigation, non-destructive testing, and geophysical exploration.
b. **Energy harvesting:** *ME* composites have the potential to be used in energy harvesting devices, where they can convert ambient magnetic and electric fields into usable electrical energy. This technology could be integrated into wearable electronics or sensors that operate in remote areas.
c. **Magnetic memory devices:** *ME* materials can be used to create non-volatile magnetic memory devices, where the state of magnetic polarization can be controlled by an electric field. This could lead to more efficient and power-saving memory technologies.
d. **Microwave devices and antennas:** *ME* composites can be employed to design tunable microwave devices and antennas. By applying an external electric or magnetic field, the resonant frequency (f_r) of the devices can be adjusted, enabling frequency (f) agility and adaptability in communication systems.

e. **Spintronics:** In spintronics, the spin of electrons is exploited to create novel electronic devices. *ME* composites can be utilized to manipulate spins electrically, enabling the development of spintronic devices like spin filters and spin transistors.
f. **Actuators and motors:** The *ME* effect can be utilized to create actuators and motors with improved efficiency and better control. By applying an electric field, the magnetic properties of the composite can be altered, leading to precise and responsive motion.
g. **Biomedical applications:** *ME* composites hold promise in biomedical applications, such as drug delivery systems, where magnetic fields can be used to guide drug-carrying nanoparticles to specific targets in the body.
h. **Magnetic shielding:** *ME* materials can be employed in the design of efficient magnetic shielding materials to protect sensitive electronic components from external magnetic interference.
i. **Robotics and automation:** The ability of *ME* composites to convert magnetic fields into electrical signals can be harnessed in robotics and automation, enabling smarter and more responsive machines.

Chapter 2

Literature review

Overview

This chapter is mainly focused on the factors that have influence on the *ME* coupling of composites. Initially, the impact of substitution and doping on the BNT-based solid solutions is reviewed followed by the effect of substitution on magnetostrictive phase. The *ME* coupling in particulate and laminates has been discussed. The effect of phase fraction and applied *f* of *H* on *ME* coupling among particulates and laminates is also presented. Based on these studies, the literature gap is discussed followed by the objectives for the research work.

The *ME* coupling depends upon the type of PE phase, magnetostrictive phase, connectivity among them, phase fraction and applied *f* of *H*. These factors are discussed one by one in the forthcoming sections of this chapter.

2.1 PE phase

The FE materials of ABO_3-type perovskite such as lead zirconium titanate (PZT) and its derivatives have dominated the field over the past five decades [29]. The reported d_{33} (225 – 590 pC/N) of such materials is far high as compared to earlier discovered materials like quartz tourmaline and Rochelle salt [30]. However, the adverse effects of lead (Pb) on human health pose the researchers to develop lead-free perovskite materials [31]. Therefore, these days FE materials are categorized as lead-based and lead-free. Amongst lead-free FE material, single phase $Bi_{0.5}Na_{0.5}TiO_3$ (BNT), $Bi_{0.5}K_{0.5}TiO_3$ (BKT), $K_{0.5}Na_{0.5}NbO_3$ (KNN) and $BaTiO_3$ (BT) are well known for exhibiting good FE and PE properties [32]. Among them, BNT exhibits high P_s ~ 40 μC/cm^2, good P_r ~ 38 μC/cm^2, moderate d_{33} ~ 58-95 pC/N and high temperature sustainability upto 320 °C [33].

BNT belongs to the perovskite family and has rhombohedral (*R*) crystal structure, where Bi and Na atoms are at A-site and Ti atoms at B-site as shown in **Figure 2.1**. According to Pauling's model, the ionic radii of Bi^{3+}, Na^+ and Ti^{4+} are 102 pm, 116 pm and 68 pm. The distortion at their lattice sites can be seen when a cation of similar size is substituted or doped at their respective site in the crystal structure, which impedes the centrosymmetry and improve the d_{33} of the resultant material. The BNT retains its *R* crystal structure upto 180 °C, which accounts for its ferroelectricity [34]. Above 180 °C, the growth of tetragonal (*T*) phase causes the anti-ferroelectric characteristics and the paraelectric cubic phase has been observed at 320 °C [34,35]. The PE property of BNT can be improved by introducing morphotropic boundary (MPB) region in the crystal system. MPB refers to a specific compositional region where two different PE phases coexist [36]. This occurs due to the non-linear coupling between two or more structural phases with different crystal symmetries. At MPB, one of the phases typically has a higher d_{33} and the other has high electromechanical coupling factor (k_{33}). Due to the MPB formation, the material can possess optimum properties, resulting in an enhanced overall PE response.

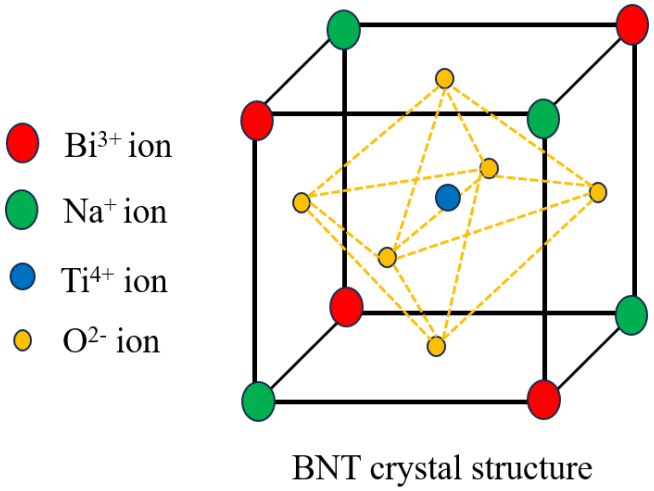

Figure 2.1. Unit cell of perovskite-BNT, where Bi and Na ions occupy corner, Ti occupy body centered and O ions at the face centered position of the cube.

The BNT-based solid solutions exhibit excellent d_{33} in the vicinity of MPB regime. Their MPB has been studied for several phases that have either one of *T*, orthorhombic (*O*) and pseudo-cubic (*Pc*) crystal structure. The PE performance of BNT-based ceramics are significantly influenced by factors like lattice distortion, ion displacement, defect structure, grain size, and density. The d_{33} values for BNT based binary systems lies in the range 93-165 pC/N, where BNT-BT and BNT-BKT solid solution exhibits maximum d_{33} of 155 pC/N and 165 pC/N respectively [37,38,47–56,39,57,40–46]. This suggests the MPB solid solution of *RT* BNT-BKT ceramics exhibits relatively high d_{33} than the other binary systems. This is due to the relatively larger ionic radii of K^+ ion (133 pm) that causes more lattice distortion than the other substituted ions. It has been observed that the d_{33} of binary solid-solutions can be further improved by ion doping either at A or B-site of its perovskite crystal structure. The dopant slightly differs in size of the respective A or B-site cation causes the lattice distortion, ion displacement and domain configuration in the crystal structure that directly influence the PE properties of the ceramics. The d_{33} for several ion doped BNT-based binary solid solution ranges in 132-180 pC/N [58,59,68–73,60–67]**.** It can be concluded that the ion doping enhances the d_{33} of several BNT-based solid solutions and suggest Ag^+ (ionic radii: 114 pm) doping is superior for achieving high d_{33} in the binary BNT-BKT solid solutions. Further, the d_{33} can be improved in the BNT-based ternary solid solutions in the vicinity of MPB regime. The d_{33} corresponds to different BNT-based ternary solid solutions is shown in **Table 2.1**.

Table 2.1. d_{33} of different BNT-based ternary solid solutions.

Material	Phase	d_{33} (pC/N)	Year	Ref.
79BNT-18BKT-3$BiFeO_3$	*R-T*	170	2008	[74]
88BNT-6BT-6$Bi_{0.5}Ag_{0.5}TiO_3$	*R-T*	172	2011	[75]
72BNT-8$Bi_{0.5}Li_{0.5}TiO_3$-20BKT	*R-T*	190	2009	[76]
$(Bi_{0.95}Na_{0.75}K_{0.15}Li_{0.05})0.5Ba_{0.05}TiO_3$	*R-T*	194	2007	[77]
81BNT-18BKT-1$LiNbO_3$	*R-T*	195	2009	[78]
86.5BNT-6BT-7.5$Bi_{0.5}Li_{0.5}TiO_3$	*R-T*	208	2008	[79]
82BNT-16BKT-2$KNbO_3$	*R-T*	215	2007	[80]
72.5BNT-22.5BKT-5$Bi(Mg_{0.5}Ti_{0.5})O_3$	*R-T*	180-220	2014	[33,81,82]

Thus, from the table 2.1, it can be concluded that 72.5(BNT)-22.5(BKT)-5$Bi(Mg_{0.5}Ti_{0.5})O_3$ (BNKMT) is a potential candidate as a choice of PE phase for synthesizing *ME* composite. In addition, BNKMT exhibits low E_c ~ 20 kV/cm, good P_r ~ 26.2 μC/cm^2, and high d_{33}^* ~ 500 pm/V. In BNKMT K^+ (133 pm) ion is substituted at A-site, whereas Mg^{2+} (86 pm) at B-site. The substitution of Mg^{2+} at Ti^{4+} site distorts the neutrality of the perovskite structure. To preserve charge neutrality some of Bi^{3+} (102 pm) cations get converted to Bi^{5+} (90 pm) and cause the high disorder in the crystal structure.

Figure 2.2 depicts the *P-E* loops of the BNKMT specimens under different processing conditions, which reveals the pure FE character when synthesized at 900 °C via sol-gel method [33](**Figure 2.2**(a)) whereas slight anti-ferroelectric (AFE) character is get introduced for the specimen prepared via solid state reaction route and processed 1100 °C [82] (**Figure 2.2**(b)). The phase diagram of BNT-BKT-BMT solid solutions has been shown **Figure 2.2**(c) [82], which indicates the MPB lies in the concentration regime of BNT (70-80%), BKT (20-30%) and BMT (0-5%). However, no thorough investigation is available on the exact MPB concentration. Thus, it can be concluded that the BNKMT specimen requires comprehensive study towards its optimization, which is completely ignored in the literature.

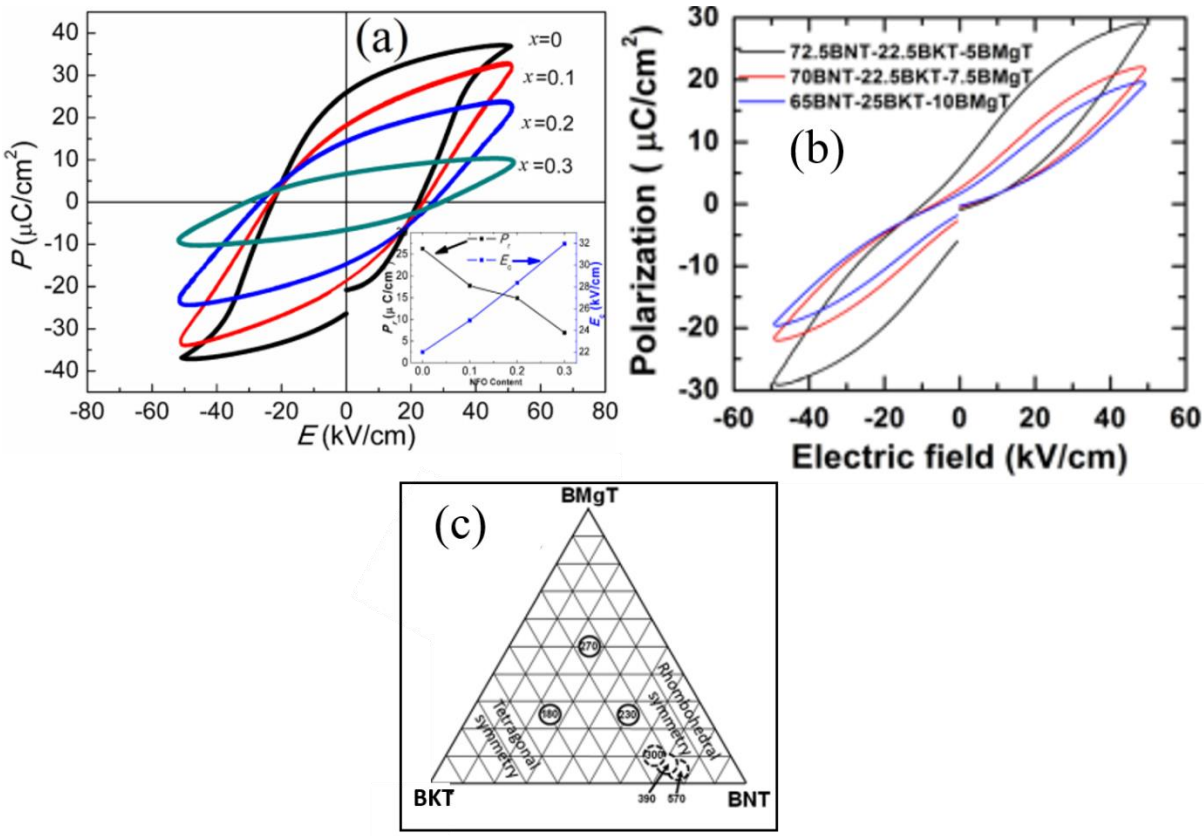

Figure 2.2. *P-E* loop of (a) (1-x)BNKMT-xNFO and (b) BNKMT, 70BNT-22.5BKT-7.5BMgT and 65BNT-25BKT-10BMgT specimens. (c) Phase diagram of BNT-BKT-BMT solid solutions [33,82].

2.2 Magnetostrictive phase

In order to choose good magnetostrictive phase, the magnetostrictive coefficient (λ_s) material should be high at low H. The λ_s of the different spinel ferrites are tabulated in **Table 2.2**.

Table 2.2. λ_s for different spinel ferrite materials [83].

Material	λ_s (ppm)
$MnFe_2O_4$	-5
Fe_3O_4	40
$CoFe_2O_4$	-110
$MgFe_2O_4$	-6
$Li_{0.5}Fe_2O_4$	-8
$NiFe_2O_4$	-26
$CuFe_2O_4$	-9

YFe_5O_{12}	-2
$SmFe_5O_{12}$	3.3
$DyFe_5O_{12}$	1.46
$EuFe_5O_{12}$	9.48

Among them, $CoFe_2O_4$ (CFO), Fe_3O_4 (FO) and $NiFe_2O_4$ (NFO) has shown relatively higher λ_s. However, CFO and FO attain these values at very high, i.e., ~ 5 kOe [84]. On the other hand, NFO exhibit λ_s ~ -26 ppm around 1 kOe [85], which suggest the suitability of material for making low *H ME* devices. NFO has an inverse spinel crystal structure, where Ni has divalent, and Fe has trivalent cationic states. In NFO, O^{2-} ions occupy corners and faces, Ni^{2+} occupy octahedral void site, Fe^{3+} are equally distributed at both octahedral and tetrahedral sites of the unit cell as shown in **Figure 2.3**.

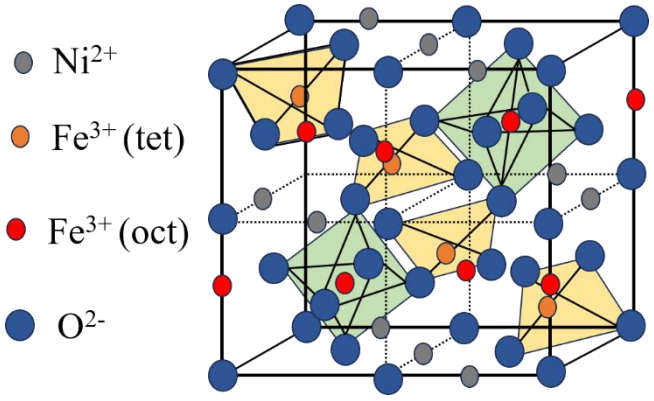

Figure 2.3. Schematic of NFO crystal structure, where Ni^{2+} occupies octahedral void site, Fe^{3+} are equally distributed at both octahedral and tetrahedral sites and O^{2-} ions occupy corner and face center of the FCC unit cell.

The Fe^{3+} ions at octahedral and tetrahedral sites have equal and opposite magnetic moments and their resultant magnetic moment is zero. In NFO, the net magnetic moment is $2\mu_B$, which is only due to Ni^{2+} ion spins. Therefore, NFO possess good saturation magnetization (M_s ~ 52 emu/g) and low coercivity (H_c ~ 70 Oe) [85,86]. NFO based magnetic materials are suitable for inducing high strain at low *H*. However, the piezomagnetic (PM) coefficient (q_s) for NFO derivative is not available in the literature. So, the indirect relevance between magnetization (*M*) and q_s has been considered as follows,

$$q_s = \frac{d\lambda}{dH} \propto \frac{dM^2}{dH} \tag{2.1}$$

Therefore, dM^2/dH indicates the qualitative q_s. The NFO is inverse spinel ferrite, where Ni^{2+} ion occupies B-site and Fe^{3+} ions are equally distributed at both A and B-sites. So, in NFO, the cations can be substituted either at Ni-site or at Fe-site. When substituting at the Fe-site ($NiS_xFe_{2-x}O_4$, where S is the substituted cation), specifically with cations like Ce, Cr, Er, Gd, Tb, and Al, the M_s decreased as they are non-magnetic in nature [87–93]. However, the substitution of metals like V, Nd, Dy and In enhances the M_s, which is tabulated in **Table 2.3**.

Table 2.3. Magnetic properties of $NiS_xFe_{2-x}O_4$ ceramics.

S	*x*	M_s (emu/g)	Ref.
V	0.2	43.2	[94]
Nd	0.03	59.8	[95]
Dy	0.07	60.02	[96]
In	0.3	68	[97]

On the other hand, the cation substitution at Ni-site (i.e., $Ni_{1-x}S_xFe_2O_4$) increases the magnetic properties of NFO as tabulated in **Table 2.4**. It has been observed M_s increases with the substitution of both alkaline earth metals (like Ca and Mg) and transition metal (like Cu, Mn and Zn).

Table 2.4. Saturation magnetization of $Ni_{1-x}S_xFe_2O_4$ ceramics with different substitutions.

S	*x*	M_s (emu/g)	Ref.
Cu	0.2	33	[98]
Ca	0.5	40.12	[99]
Cd	0.3	46	[100]
Ca, Mg	0.05	54.12	[101]
Mn	0.4	61.2	[102]
Mg	0.1	64.54	[103]
Zn	0.4	73	[104]

Thus, it can be concluded that the $Ni_{1-x}Zn_xFe_2O_4$ (NZ_xFO) exhibit highest M_s among all the substituted NFO composition because the diamagnetic Zn^{2+} occupies tetrahedral A-site of inverse spinel structure and to preserve the number of cations at B-site Fe^{3+} ions at A-site migrates to B-site and violates the compensation mechanism governed by equal number of Fe^{3+} ions distributed at both A and B-sites. Moreover, NZ_xFO ceramics exhibit good q_s of order

0.02-0.07 ppm/Oe [105], which make it suitable magnetostrictive candidate for synthesizing the *ME* composite.

2.3 Role of connectivity

As discussed earlier, the 0-3 connectivity between PE and magnetostrictive phase have relatively higher leakage current density than 2-2 composites. Therefore, it is hard to achieve good polarization in 0-3 matrix composition. There are several reports available on BNT-based 0-3 *ME* composites and are represented in **Table 2.5**.

Table 2.5. α_E (at 1 kHz) for the several 0-3 composites comprising BNT-based materials coupled with different ferrites.

PE Phase	Magnetostrictive Phase	PE:Magnetic Phase fraction	α_E (mV/cm.Oe)	Ref.
BNT	CFO	65:35	0.5	[106]
BNT	$BaFe_{12}O_{19}$	80:20	2.29	[107]
BNT	$NZ_{0.5}FO$	80:20	4.33 at 10 Hz	[108]
BNT	$MgFe_2O_4$	80:20	4.79	[109]
0.93BNT-0.07BCTS	$MgFe_2O_4$	75:25	4.95	[110]
BNT	CZFMO	80:20	5.8	[111]
BNT	$CoMn_{0.2}Fe_{1.8}O_4$	90:10	6.76	[112]
BNT	$Ni_{0.2}Co_{0.8}Fe_2O_4$	60:40	7.54	[113]
BNT	$BiFeO_3$	40:60	9	[114]
0.8BNT-0.2BKT	$NZ_{0.2}FO$	65:35	42.41	[115]
BNKMT	NFO	80:20	73	[116]
BNKMT	CFO	80:20	112	[81]

Where, BCTS and CZFMO are $Ba_{0.945}Ca_{0.055}Ti_{0.91}Sn_{0.09}O_3$ and $Co_{0.6}Zn_{0.4}Fe_{1.7}Mn_{0.3}O_4$ respectively. The *ME* composite comprising BNKMT, and spinel ferrites are the promising for *ME* device applications. However, its *ME* coupling with Zn modulation is not reported in the literature. Further, relatively higher *ME* coupling in 2-2 composites is tabulated in the **Table 2.6**.

Table 2.6. α_E (at 1 kHz) for numerous 2-2 type *ME* composites comprising BNT-based ceramics coupled with magnetic ferrites.

PE Phase	Magnetostrictive Phase	α_E (mV/cm.Oe)	Ref.
0.8BNT-0.2BKT	NFO	86	[117]
0.8BNT-0.2BKT	$NZ_{0.2}FO$	115.1	[118]
0.35BNT-0.65BT	$NZ_{0.2}FO$	140	[119]
0.97(BNT)–0.03(KNLNST)	CZFMO	142	[120]

where, KNLNST is $K_{0.47}Na_{0.47}Li_{0.06}Nb_{0.74}Sb_{0.06}Ta_{0.2}O_3$.

There are few reports available on the BNT-based *ME* laminate composites that clearly demonstrates the giant *ME* coupling. Its reported α_E is relatively higher than the particulate composites. For instance, the maximum α_E reported in 0.8BNT-0.2BKT-$NZ_{0.2}FO$ laminate composites is 2.7 times higher than its particulate composites [115,118]. These findings encourage the researchers to develop *ME* laminate composites to achieve giant *ME* coupling.

2.3.1 Processing methods for laminate composites

The laminate composites in bulk are mostly synthesized by stacking distinct phases together with conductive epoxy as shown in **Figure 2.4(a)** [121–123]. However, the conductive epoxy is relatively softer than both PE and magnetostrictive phases which causes damping of magnetostrictive strain on PE phase. To eradicate its damping effect, co-firing technique is used as represented in **Figure 2.4(b)** [124–126]. In the co-fired method, one phase is stacked over other phase and sintered at a particular temperature. However, these distinct phases have different sintering temperature, therefore may not depict their maximal *ME* properties. To overcome this problem, a direct diffusion bonding technique has been developed as depicted in **Figure 2.4(c)**, which is one of the main contributions to achieve optimal *ME* properties. In this technique, one phase is sintered independently that has higher sintering temperature. Further, second phase is stacked on the sintered pellet by applying slight pressure during compaction. Furthermore, the composite pellet is sintered at the optimum sintering temperature of the second phase.

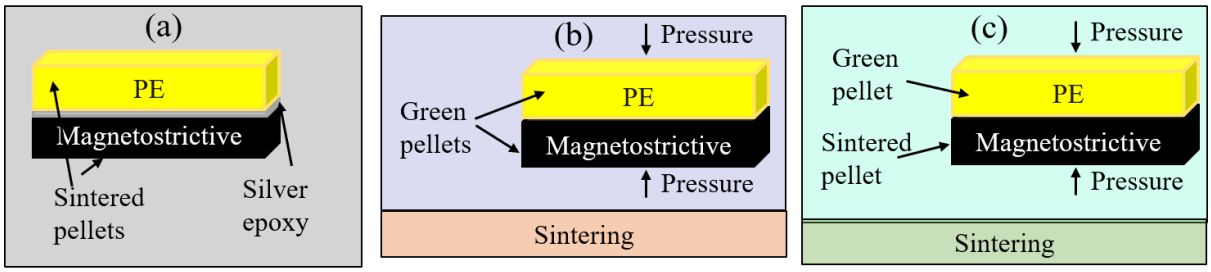

Figure 2.4. Fabrication of laminate composite using (a) silver epoxy, (b) co-firing technique and (c) direct diffusion bonding.

2.3.2 ME effect in multilayer laminate composites

In laminate composites, the *ME* effect is a function of interfacial strain transfer between the layers. Therefore, *ME* properties have been studied in bilayer and trilayer configurations. It has been observed that the trilayer laminates exhibit higher α_E compared to bilayer laminates due to an increase of interfacial area.

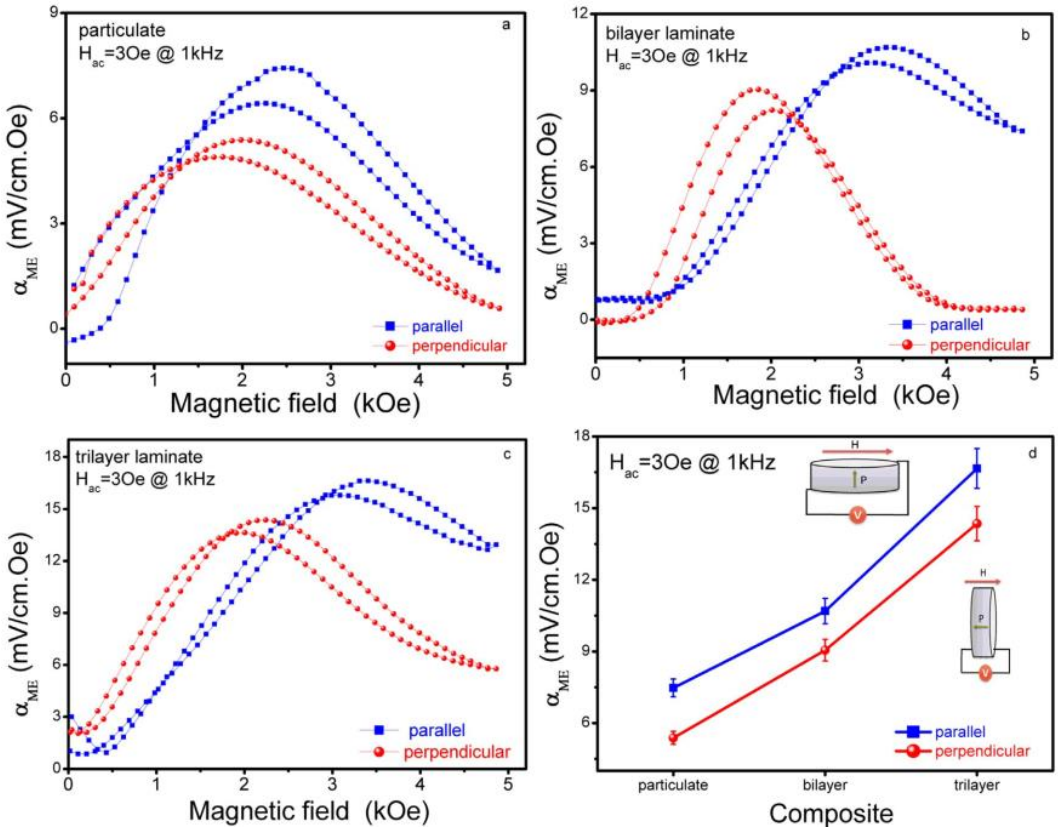

Figure 2.5. Variation in α_E with H for $(Ba_{0.85}Ca_{0.15})(Zr_{0.1}Ti_{0.9})O_3$-CFO (a) particulate, (b) bilayer laminate and (c) trilayer laminate composites. (d) Change in maximal α_E in particulate, bilayer and trilayer laminate composites [127].

For example, enhanced α_E has been reported in trilayer laminate composite of $(Ba_{0.85}Ca_{0.15})(Zr_{0.1}Ti_{0.9})O_3$-CFO than its bilayer and particulate composite [127] as displayed in **Figure 2.5**. Also, it is interesting to note that the sample placed in parallel configuration to applied *H* has shown relatively higher α_E than perpendicular configuration because magnetic phase exhibit high magnetostriction in longitudinal mode [120].

2.4 Effect of phase fraction

ME effect is a product tensor and require biphasic surrounding to achieve maximum coupling. For a particular 0-3 composite, α_E first increases with the magnetic phase fraction and decreases after a specific composition. For instance, the variation in α_E with volume fraction of NFO coupled with PZT has been shown in **Figure 2.6**.

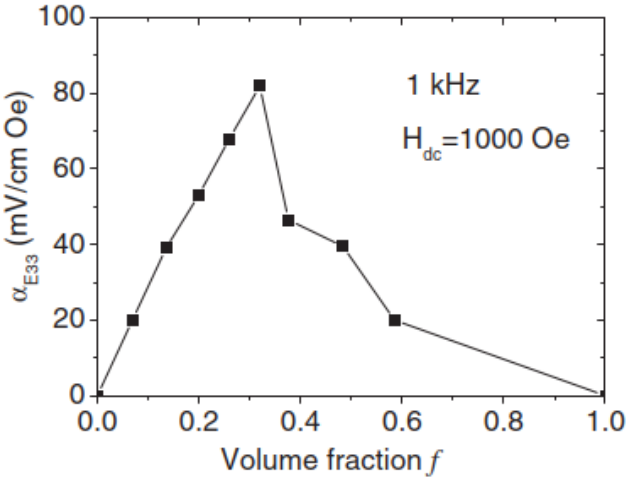

Figure 2.6. Variation in α_E with volume fraction of NFO coupled with PZT in their particulate composite [128].

In particulate composites, maximal α_E achieved for different composites at varying phase fraction as shown in **Table 2.5**. Ideally, maximal α_E should be achieved for 50:50 composition of PE and magnetostrictive phase. Practically, it is not possible due to the following reasons:

- The particles of one phase are not uniformly distributed throughout the other phase due to the limitation of mechanical mixing.
- The optimum growth of each phase particles is crucial in order to achieve their maximal properties. However, in composites the grain growth of one phase hinders the another one.
- The different sintering conditions for both phases to achieve their maximal respective properties.

Therefore, the particulate composites exhibit maximal α_E for different at phase fraction.

Similar to particulate composite, the α_E of laminates increase with the inclusion of magnetic phase upto maximal α_E and decreases thereafter. However, it has been observed that in laminates maximal α_E achieved at relatively higher volume fraction [129,130]. For example, highest α_E has been observed for volume fraction of around 0.7 for Terfenol-D in trilayer Terfenol-D/PMN-PT/ Terfenol-D laminate composite [130] as represented in **Figure 2.7**.

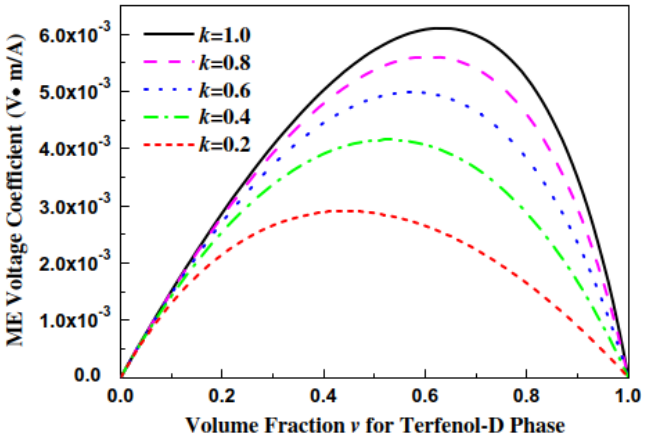

Figure 2.7. Effect of variation in Terfenol-D volume fraction on α_E in Terfenol-D/PMN-PT/ Terfenol-D laminate composite [130].

2.5 Effect of *f*

The impact of *f* on the α_E of composites involves complex interactions amongst material characteristics, domain behaviors, and phase connectivity. The *ME* specimen shows drastic change in the α_E at a certain frequency, termed as resonance frequency f_r. This is due to the high electromechanical coupling that directly affects the mutual interaction between the PE and magnetostrictive phase. At off-resonant *f* regime, the α_E do not show any substantial change. For instance, effect of *f* on α_E for PZT-NFO particulate composite has been shown in **Figure 2.8**.

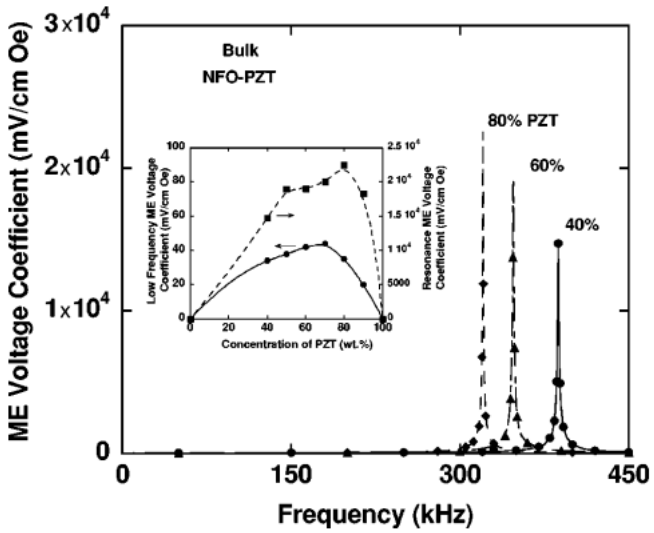

Figure 2.8. Effect of f on (1-x)PZT-xNFO particulate composite. The f_r increases with NFO content [131].

Based on these findings, it can be concluded that the f_r is strictly depends upon the phase fraction and α_E at f_r is quite high than that at off-resonant f. In addition, there is no significant change in α_E at off-resonant conditions.

2.6 Research Gaps

ME composites have gained huge attention due to their unique ability to couple magnetic and electric properties together, which facilitates their use for the multifunctional applications in sensors, energy harvesters, data storage, and biomedical devices. However, two major challenges are persisting for their use in such applications, i.e., i) environmental concern and ii) significant *ME* coupling (α_{ME} > 100 mV/cm.Oe) at low f (< 50 Hz) and low magnetic field (H < 1 kOe). To deal with these issues, lead-free *ME* composites consist of good PE phase (d_{33} > 100 pC/N) and excellent magnetostrictive material ($q_s = d\lambda_s/dH$ > 0.02 ppm/Oe for H < 1 kOe) is prerequisite. Among the several lead-free PE materials, BNKMT is promising one. On the other hand, Zn substitution in NFO is found to enhance piezomagnetism even at low H. The observation of giant *ME* response in BNKMT-spinel ferrite particulate composites has already shown its potential. However, the modulation of *ME* coupling with Zn substitution in NFO coupled with BNKMT composite is not yet studied and warrant attention from the research community. This is crucial for achieving maximal α_E for the particular concentration of Zn substitution. Further, such particular concentration of Zn substituted NFO in varying phase fraction with BNKMT is not yet explored. Moreover, there are no investigation available

on their laminate composites, which is important in order to achieve giant *ME* coupling. Therefore, in this thesis, a comprehensive *ME* study of optimized BNKMT and NZ_xFO has been undertaken in their particulate as well laminate composites.

2.7 Objectives

Based on the motivation and research gaps in literature, the following are the research objectives:

- Preparation of modified BNT- spinel (AFe_2O_4, A= Ni, Zn) magnetoelectric (*ME*) 0-3 and 2-2 composite structures.
- Investigate the effect of structural, compositional and morphological parameters on *ME* properties.

Chapter 3

Experimental and characterization techniques

Overview

This chapter includes the synthesis method for developing PE phases (BNT and BNKMT), magnetostrictive phases (NZ_xFO) and their 0-3 and 2-2 composites. A brief detail of novel direct diffusion bonding technique is given for synthesizing 2-2 composite. Further, several material characterization techniques have been explained in the final section of this chapter.

3.1 Synthesis of pure PE and magnetostrictive phase

3.1.1 Sol-gel method

High purity chemical reagents (purity > 99.5%, Sigma Aldrich) i.e., sodium acetate trihydrate ($CH_3COONa.3H_2O$), bismuth nitrate pentahydrate [$Bi(NO_3)_3.5H_2O$], titanium isopropoxide ($TiC_{12}H_{28}O_4$), 2-methoxy ethanol ($C_3H_8O_2$) and acetic acid (CH_3COOH) were used for the synthesis of BNT. First, bismuth nitrate and titanium isopropoxide chemicals were stoichiometry dissolved in 2-methoxy ethanol and sodium acetate was dissolved separately in acetic acid. These mixtures were continuously stirred at room temperature (*RT*) till homogenous solution was obtained. Then these solutions were mixed and stirred at 100 °C until solution turns into viscous gel. The gel was further heated at 180 °C till the white powder was obtained. Further, the calcination of as-prepared powders was carried at 600 °C for 3h. The calcined powder was uniaxially pressed at 100 MPa into cylindrical shape pellets of 10 mm diameter and 0.8 mm thickness and thereafter sintered at 1000 ˚C - 1075 ˚C for 1h. For BNKMT synthesis, magnesium nitrate hexahydrate [$Mg(NO_3)_2.6H_2O$], potassium nitrate [KNO_3] were used in addition to NBT reagents.

For NFO synthesis, iron nitrate nonahydrate [$Fe(NO_3)_3.9H_2O$], nickel nitrate pentahydrate [$Ni(NO_3)_2.5H_2O$], deionized (DI) water and citric acid ($C_6H_8O_7$) were used. The chemical reagents were stoichiometrically weighed and dissolved in DI-water. The mixture underwent continuous stirring at *RT* until a uniform reddish-brown translucent solution was obtained. Further NH_3 solution (25 %) was added to maintain pH ~ 7 and then the resultant solution was persistently stirred and subjected at 90 °C till the gel was formed. The gel was further heated at 150 °C till its combustion. The combust powder was black in color. Further, these powders were calcined at 900 °C for 3h. The calcined powder was uniaxially pressed at 100 MPa into cylindrical shape pellets of 10 mm diameter and 0.8 mm thickness and thereafter sintered at 1050 ˚C - 1200 ˚C for 1h. Also, in addition to NFO reagents, zinc nitrate hexahydrate [$Zn(NO_3)_2.6H_2O$] was used to prepare NZ_xFO ceramics. The flow chart for the synthesis of BNT and NFO has been displayed in **Figure 3.1**(a) & (b) respectively.

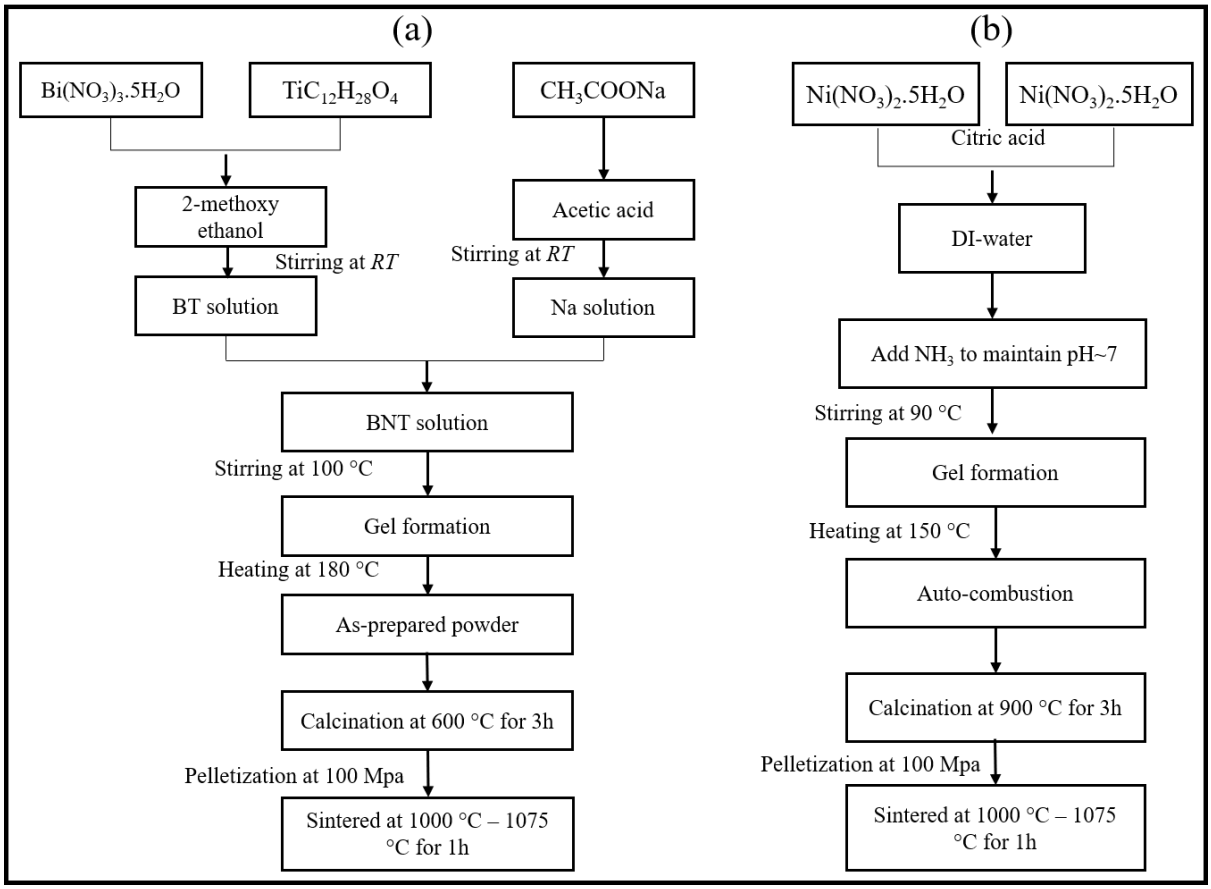

Figure 3.1. Flow chart for the synthesis of (a) BNT and (b) NFO by the sol-gel method.

3.1.2 Solid-state reaction route

Analytic grade metal precursors (purity > 99.5%), i.e., bismuth oxide (Bi_2O_3), sodium carbonate (Na_2CO_3) and titanium dioxide (TiO_2) were used to synthesize BNT, whereas nickel oxide (NiO) and iron oxide (Fe_2O_3) were used for the synthesis of NFO. Chemicals potassium acetate (KCH_3COOH) and magnesium oxide (MgO) were used in addition to BNT reagents and zinc oxide (ZnO) in addition to NFO reagents for synthesizing BNKMT and NZ_xFO ceramics respectively. The respective phase precursors were stoichiometry weighed and wet mixed in a zirconium jar at 250 rpm for 3h with a charge to ball ratio 1:5. Further, the as-mixed powders were dried and calcined separately at 900 ˚C for 3h in resistance furnace. The calcined powders of PE and magnetostrictive phases were uniaxially pressed into pellets of 10 mm diameter and 0.8 mm thickness at 100 MPa. Thereafter, PE phase pellets were sintered at 1000 ˚C - 1075 ˚C for 1h, whereas magnetostrictive phase pellets were sintered at 1050 ˚C - 1200 ˚C for 1h. The detailed processing method of solid-state reaction for the synthesis of BNT and NFO has been presented in **Figure 3.2**(a) & (b) respectively.

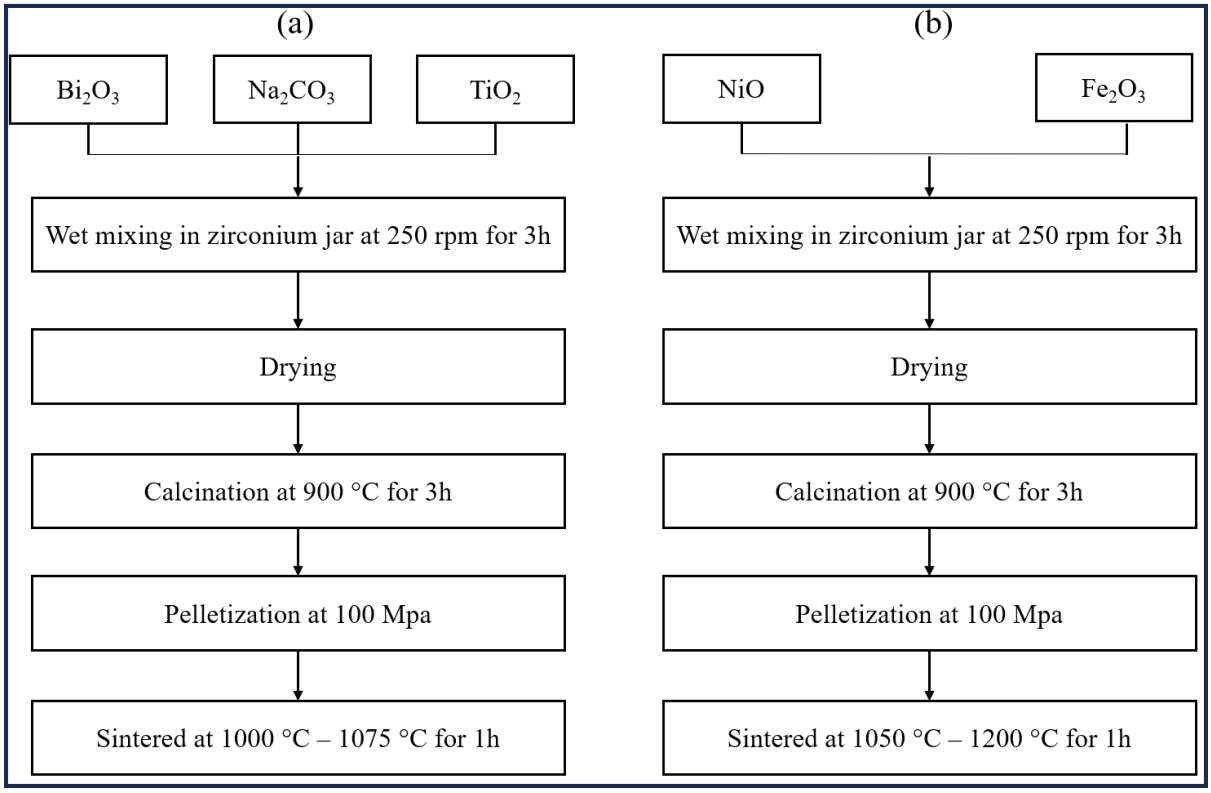

Figure 3.2. Flow chart for the synthesis of (a) BNT and (b) NFO by solid state reaction route.

3.2 Fabrication of 0-3 and 2-2 composites

3.2.1 0-3 composite

For synthesizing 0-3 composite, the appropriate weight ratio of calcined powders of PE and magnetostrictive phases were wet mixed in a zirconium jar at 250 rpm for 3h with a charge to ball ratio of 1:5 to obtain desired volume fraction composite. These mixed powders were dried and uniaxially pressed into cylindrical shape pellets at 100 Mpa followed by sintering at 1050 ˚C for 1h. Its processing flow chart has been shown in **Figure 3.3**(a).

3.2.2 2-2 composite

For developing PE/magnetostrictive laminate composite, initially, calcined magnetostrictive powder was uniaxially pressed at 100 MPa into 10 mm cylindrical pellets and sintered at 1200 °C for 1h. The PE phase calcined powder was then pressed over or in between the magnetostrictive phase pellets at 20 Mpa to prepare bilayer and trilayer laminate composite pellets. The thickness of both ferroelectric and magnetic phase pellets was kept at 0.7 mm. These composite pellets were sintered at 1040 °C for 1h. Its processing flow chart has been depicted in **Figure 3.3**(b).

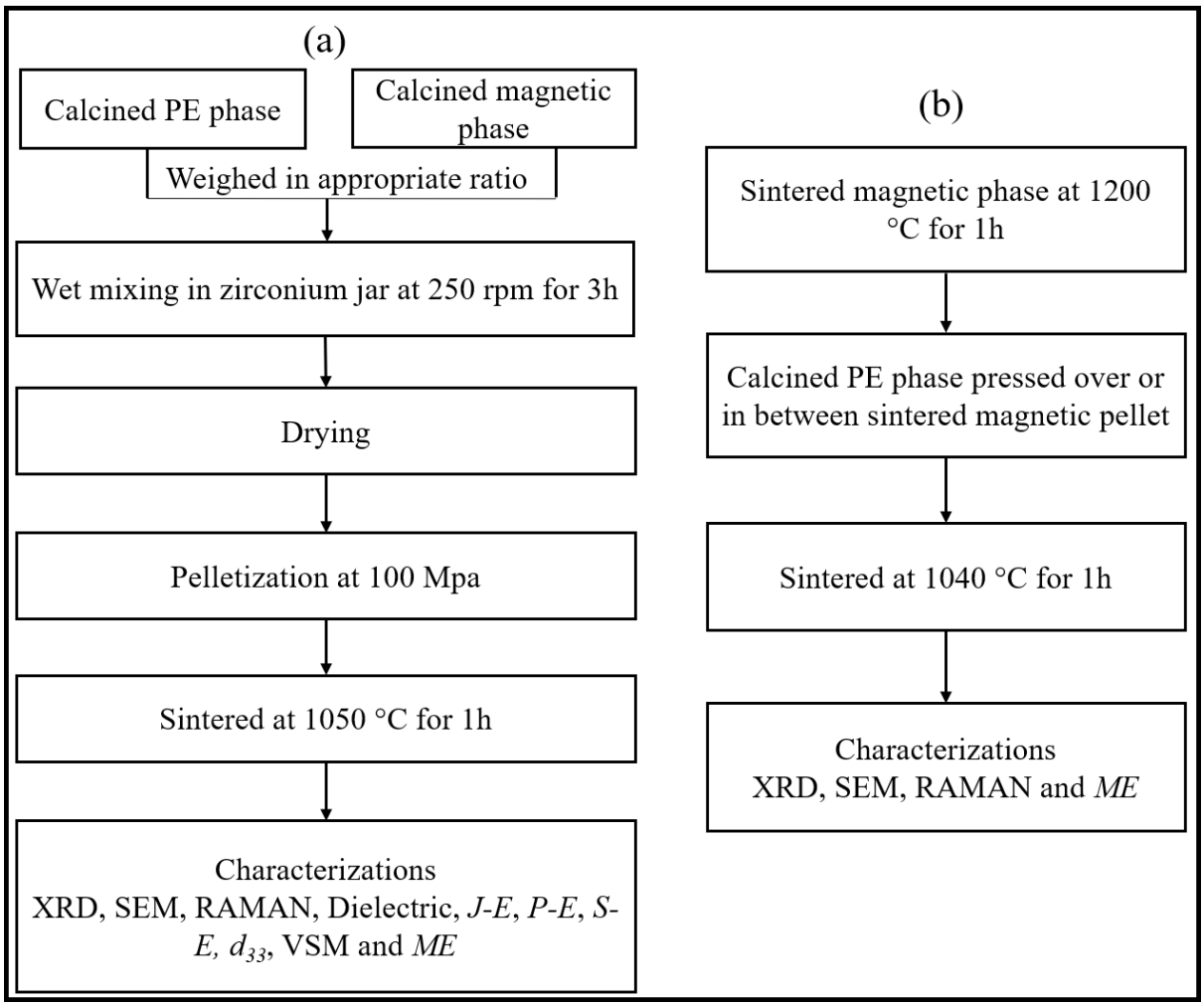

Figure 3.3. Flow chart for fabricating (a) 0-3 and (b) 2-2 *ME* composites.

3.3 Materials Characterization

The structural characterizations of all pure and composite specimens were carried out by X-ray diffractometer (XRD), Raman spectrometer and field emission scanning electron microscopy (FE-SEM). Further, the *RT* dielectric and leakage current density (*J*) measurements for PE phases and 0-3 composites was recorded using LCR-meter and electrometer respectively. Their FE properties were examined by Multiferroic test system and further d_{33} measurements were recorded by using d_{33}-meter. The magnetic properties of the magnetostrictive phases and 0-3 composites were recorded using vibrating sample magnetometer (VSM). For all the composite specimens, *ME* properties were investigated by Multiferroic test system. The concise description for each testing facility along with specifications has been given below.

3.3.1 X-ray Diffraction (XRD)

The phase purity of all the specimens were examined by Rigaku X-ray diffractometer (XRD) (model: Smartlab SE, Japan). The diffraction data was recorded in 2θ range from 20°-80° with a step size of 0.013°, where θ is Bragg's or diffraction angle. To evaluate crystallite size (*D*), Scherrer's formula was used [132]:

$$D = \frac{K\lambda}{\beta Cos\theta} \quad (3.1)$$

Where *K* is dimensionless shape factor (0.89 for both cubic and rhombohedral crystal structure), λ is the wavelength of Cu-K_α radiation (0.154 nm) and β is full-width at half maxima.

3.3.2 Raman Spectroscopy

To investigate lattice distortion, disorder and strain in the crystalline ceramics, the Raman spectroscopic analysis was carried out in range 100 – 800 cm^{-1}. The spectrum was recorded using Micro-Raman Spectrometer (Labram HR Confocal, Horiba, France) (instrumental resolution ±1 cm^{-1}) equipped with a 532 nm diode pumped solid state laser at 25 mW power.

3.3.3 Microstructure analysis

The microstructural examination of the sintered specimens was carried out by FE-SEM (Carl-Zeiss, Sigma 500, Germany). Prior to the measurement, a fine layer of gold (Au) with a thickness < 5 nm was coated through sputtering onto the sample's surface to mitigate the charging effects. The back-scattered micrographs were acquired using a dedicated backscattered electron detector attached with the FE-SEM. The energy dispersive spectrometer of Bruker (QUANTAX 200) equipped with the FE-SEM was used to record energy dispersive spectra (EDS) and elemental mapping. The average grain size was calculated using Image-J software.

3.3.4 Dielectric properties

The *f* dependent dielectric constant (ε_r) and dielectric loss (tanδ) ranges from 10^2 Hz -10^6 Hz has been carried out using Fluke LCR meter (model: PM 63 at 100 mV. Prior to all electrical and *ME* measurements, the pellets were silver coated on the both ends and heated at 200 °C for 2h.

3.3.5 Leakage current measurement

The leakage current density (*J*) of the ceramics in reversible dc *E* has been examined using Keithley electrometer (6517B, USA). All the measurements were performed at 10 V step-size.

3.3.6 Piezoelectric charge coefficient measurement

To determine the piezoelectric charge coefficient (d_{33}), the Sinocera d_{33} meter (model: YE2730A, China) was used that setup at a force of 0.25 N. Prior to the d_{33} measurements, the specimens were poled using Corona poling (Millman thin films PVT. LTD. Pune, India). The specimens were placed at 2 cm distance from tungsten needle at a voltage of 10 kV for 5 minutes.

3.3.7 Magnetic measurements

The magnetization *vs* magnetic field (*M-H*) curves were recorded using Lakeshore (model: 7404, USA) vibrating sample magnetometer (VSM). The measurements were carried out in range -10 kOe to +10 kOe with a step size of 200 Oe. The virgin *M* curves has also been plotted in the 1st quadrant to evaluate magnetic permeability using formula,

$$M = \mu H \tag{3.2}$$

To determine qualitative PM coefficient, dM^2/dH *vs* H plot has been investigated.

3.3.8 Magnetoelectric measurements

The polarization *vs* electric field (*P-E*), strain *vs* electric field (*S-E*) and α_E *vs* H has been investigated using Precision multiferroic-II system (Radiant Technology, USA). For the pure PE phase, the FE measurements were carried out at 1 Hz, whereas *FE* and *ME* measurements for the composites were recorded at 10 Hz.

The *ME* measurements were carried out in an applied ac magnetic field of 3 Oe at 10 Hz using Helmholtz coil (Lakeshore MH-6, USA), which is operable maximum up to 20 Hz. The sample holder for the *ME* measurements has been shown in Figure 3.4. The *dc* magnetic field was varied using electromagnets (GMW 5480, USA) (Figure 3.5). In this method, charge (*q*) and capacitance (*C*) were measured with H_{dc} at fixed H_{ac}. The notation H_{dc} and H_{ac} represents the applied dc magnetic field and ac magnetic field respectively.

For the α_{ME} measurement, the virtual ground charge-measurement input of a Radiant Precision Multiferroic tester was linked to the composite specimen. The Helmholtz coil (Lakeshore MH-6) which can produce a maximum *H* of ±45 Oe that was used along with DC magnet (GMW

5480, USA) which can goes upto a limit of 2000 Oe. The sample has been solely exposed to a 3 Oe triangular wave at 10 Hz during the measurement. The multiferroic-II measures the charged developed by the sample using electrometer. Further the capacitance of the samples was measured under same condition. Thus, α_{ME} is calculated using the formula given in equation (3.3)

$$\alpha_{ME} = \frac{q}{C.t.H_{ac}} = \frac{V_{out}}{t.H_{ac}} \tag{3.3}$$

It should be noted that if leakage current contributes, then the measured q signal in applied H_{ac} wanders. The amplitude of wander determines the order of leakage current. In such case, the q-H loop is fitted with the 2nd order polynomial equation to eliminate the contribution of leakage current, i.e.,

$$q = A_1H^2 + A_2H + A_3 \tag{3.4}$$

where, A_1, A_2 and A_3 are the coefficients of polynomial equation. The slope of equation (3.4) is

$$\frac{dq}{dH} = 2A_1H + A_2 \tag{3.5}$$

To calculate α_{ME}, equation (3.5) is divided with C and t as

$$\alpha_{ME} = \frac{2A_1H + A_2}{C.t} \tag{3.6}$$

Figure 3.4. Sample holder for the *ME* measurements.

Figure 3.5. DC electromagnets connected with the master-slave power supply.

Chapter 4

Results and discussion: Pure Phases

Overview

In this chapter, the synthesis and optimization of both PE and magnetostrictive are discussed. This chapter is categorized into four sections. In first two sections, the effect of sintering temperature on the structural and electrical properties of PE BNT and BNKMT phases has been investigated. In the third section, the influence of sintering temperature on the structural and magnetic properties of NFO is presented. In the last section, effect of Zn substitution on the magnetic properties of the optimized NFO has been discussed.

4.1 Synthesis and optimization of BNT

The BNT has been synthesized by sol-gel and state reaction route at 600 °C and 900 °C respectively for 3h. Thereafter, phase analysis of sol-gel and solid state driven BNT is studied using XRD pattern as shown in **Figure 4.1**. All the diffraction peaks have been matched with JCPDS card: 36-0340 reveals the formation of pure BNT. The lack of any additional peak confirms that there is no secondary phase formation.

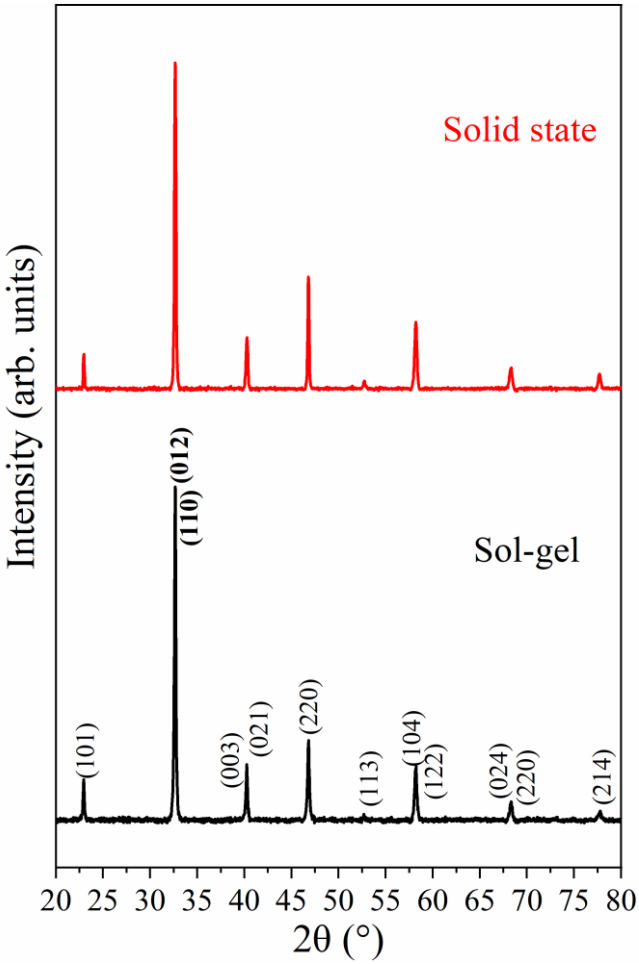

Figure 4.1. XRD pattern of sol-gel and solid-state driven BNT ceramics calcined at 600 °C and 900 °C for 3h.

Further, the calcined BNT was sintered at 1000 °C - 1075 °C for 1h. The effect of sintering temperature (T_s) on its phase, structural, dielectric and FE properties has been investigated.

4.1.1 Phase analysis

Figure 4.2 depicts the XRD pattern of pure BNT ceramics sintered at 1000 °C – 1075 °C. The diffraction peaks are matched with the JCPDS card number 36-0340 (**Figure 4.2**(a)) that

reveals the formation of perovskite crystal structure without any secondary phase. Further, it can be seen that the diffraction peaks slightly shift towards higher angle (**Figure 4.2**(b)), which reveals the strain induced with higher T_s. Moreover, crystallite size (D) increases with T_s (see **Table 4.1**) and calculated by the Scherrer's formula (equation 3.1).

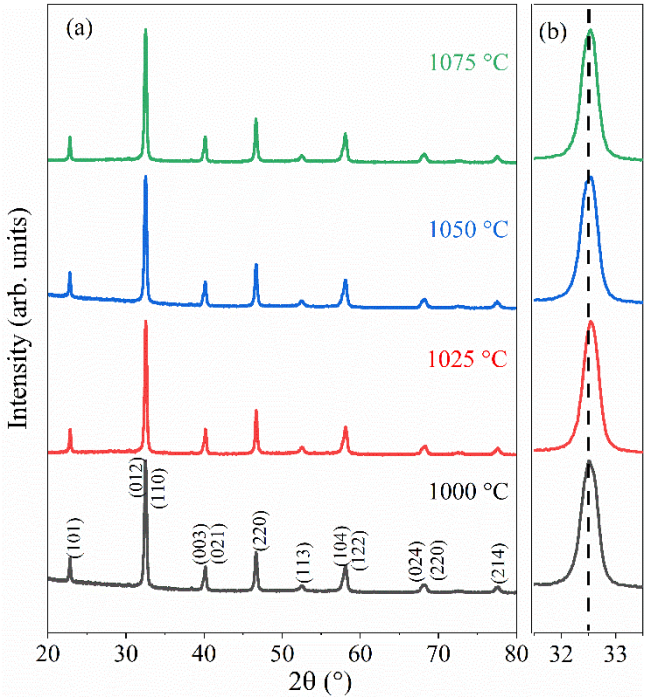

Figure 4.2. XRD pattern of sintered BNT ceramics at 1000 °C – 1075 °C in 2θ range (a) 20°-80° and (b) Zoom portion of BNT from 31.8°-33° to clearly identify the peak.

Table 4.1. Crystallite size of BNT based ceramics processed at 1000 °C – 1075 °C for 1h.

T_s (°C)	D (nm)
1000	36.01
1025	39.87
1050	43.17
1075	45.21

4.1.2 Raman study

The Raman spectroscopy has been used to investigate the effect of T_s on the optical vibration modes of BNT. All specimens exhibit conventional 3 Raman bands of the ABO_3 perovskite structure [133], which are designated as X, Y and Z and represented in **Figure 4.3**(a).

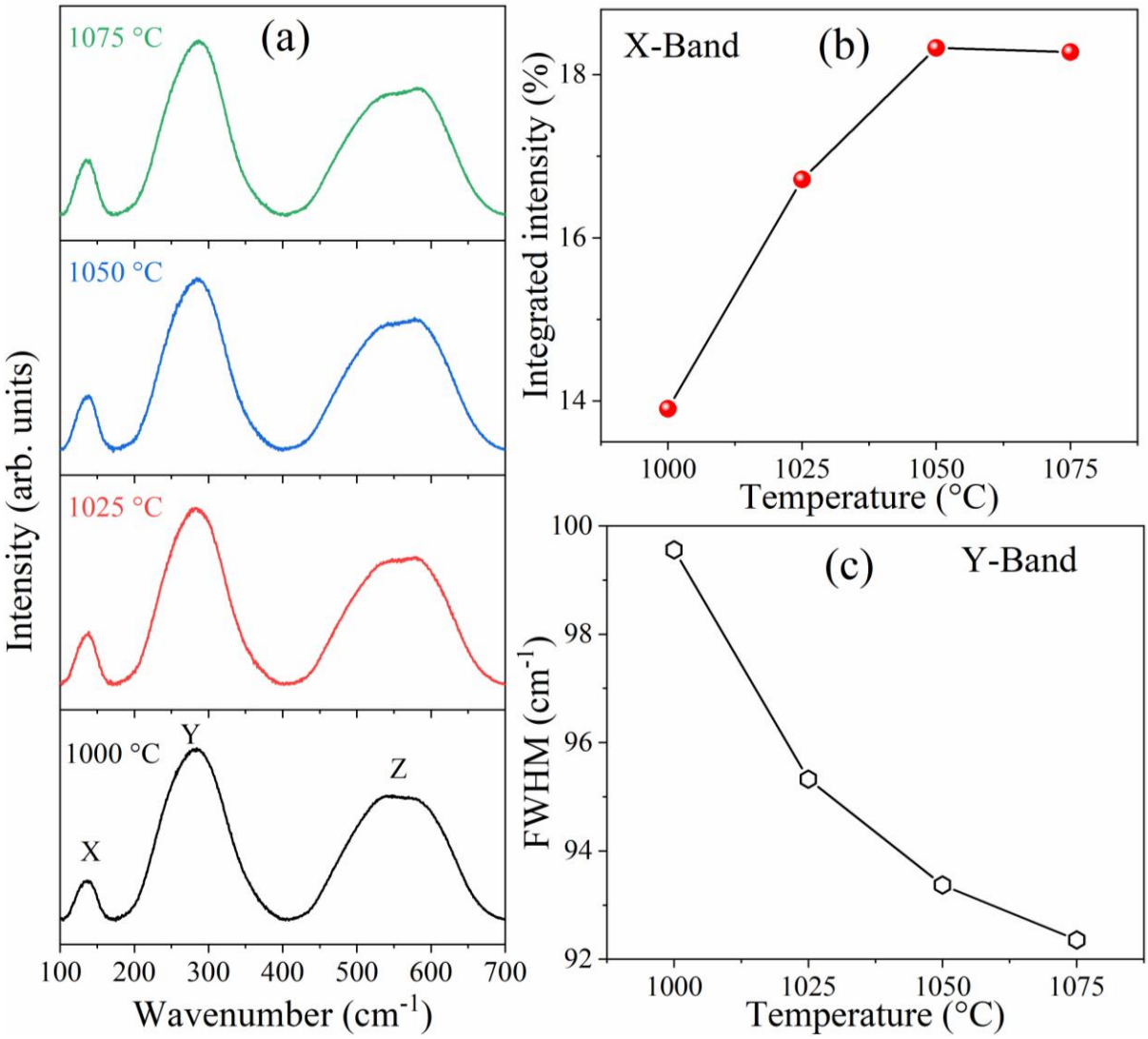

Figure 4.3. (a) Raman spectra of BNT ceramics sintered at 1000 °C – 1075 °C for 1h. Variation in (b) integrated intensity of X-band and (c) FWHM of Y-band with T_s.

The X band determine the A-O vibrations, whereas Y and Z represent the B-O and B-O_6 octahedra vibrations of the perovskite ABO_3-structure respectively. The integrated intensity of X-band increases with T_s (**Figure 4.3**(b)) upto 1050 °C and decrease thereafter. This suggests the structure is stable up to 1050 °C and there is formation of defects at A-site above 1050 °C. Further, the band width of the bands decreases with T_s, which indicates the progressive

reduction of phonon scattering from the grain boundaries [134]. A representative of variation in full-width at half maxima (FWHM) with T_s for Y-band is demonstrated in **Figure 4.3**(c).

4.1.3 Microstructural analysis

Further, the effect of variation in T_s on the microstructure of BNKMT has been investigated and shown in **Figure 4.4**. All the grains have cube like structure without any visible defects and pinholes or pores. The average grain size of BNT ceramics sintered at 1000 °C is 0.44 μm that increases with sintering temperature. The average grain size is 0.61 μm, 0.78 μm and 1.23 μm for the BNT ceramics sintered at 1025 °C, 1050 °C and 1075 °C respectively. A dense microstructure is crucial in order to achieve good FE and PE properties.

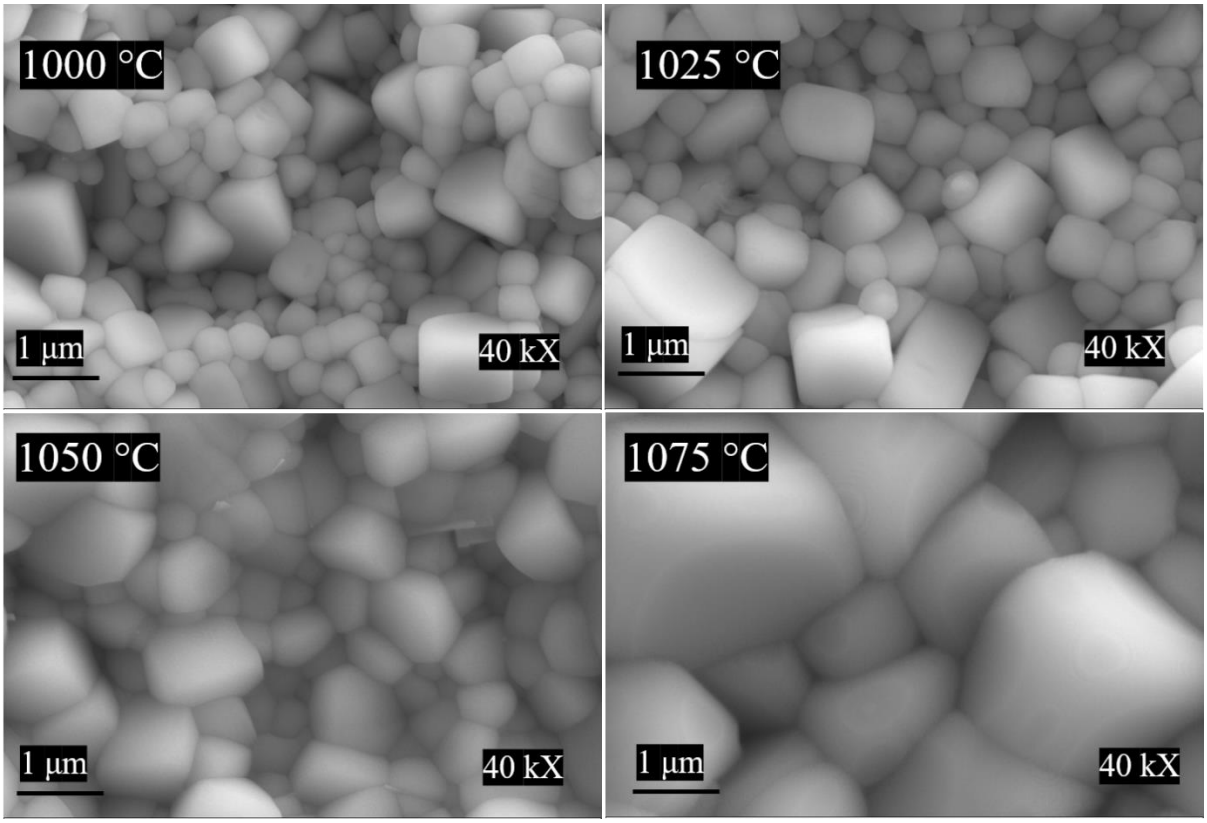

Figure 4.4. SEM micrograph of BNT ceramics sintered at 1000 °C – 1075 °C for 1h.

4.1.4 Dielectric study

The *RT* dielectric measurements in *f* range 10^2 Hz - 10^6 Hz for BNT ceramics sintered at 1000 °C – 1075 °C is represented in **Figure 4.5**. The ε_r and tan δ decreases abruptly with *f* up to 10^4 Hz that indicates the restricted movements of space charges with *f* in accordance to Maxwell–Wagner polarization model [135]. The ε_r increases and tan δ decreases with T_s (at 1 kHz) (**Table**

4.2) depicts the rise in polarizability and dip in losses with the larger grains. However, at 1075 °C the rise in tan δ indicates the origin of defects at high T_s.

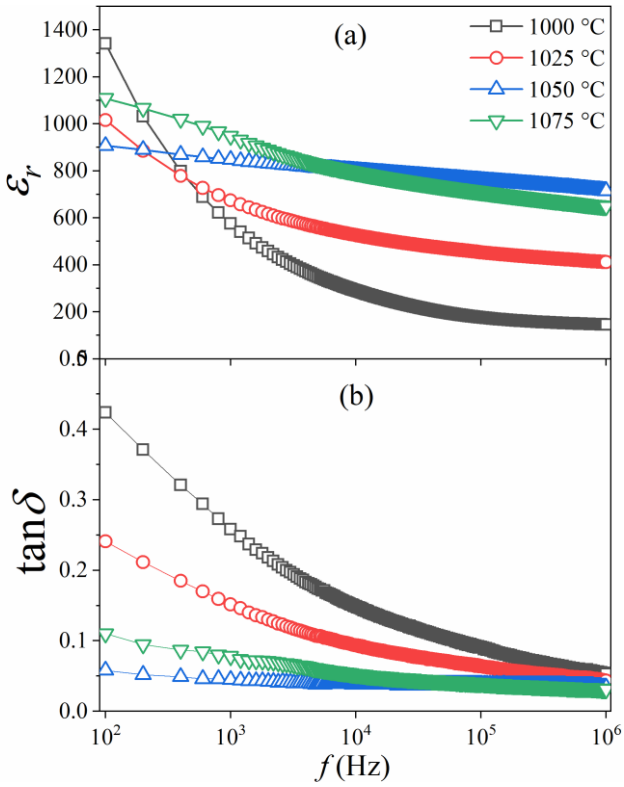

Figure 4.5. Variation in f dependent (a) ε_r and (b) tan δ for BNT ceramics sintered at 1000 °C – 1075 °C.

Table 4.2. ε_r and tan δ at 1 kHz for BNT specimen sintered at different temperatures.

T_s (°C)	ε_r	tan δ
1000	576	0.25
1025	675	0.15
1050	848	0.045
1075	944	0.078

4.1.5 Leakage current study

Further, the *RT* variation in *J* with *E* for BNT ceramics has been displayed in **Figure 4.6**. The sharp increase in *J* till 1 kV/cm is attributed to the space charge conduction. Above 1 kV/cm, gradual increase of *J* indicates the contribution of grain boundaries, and Poole-Frenkel emission [136,137].

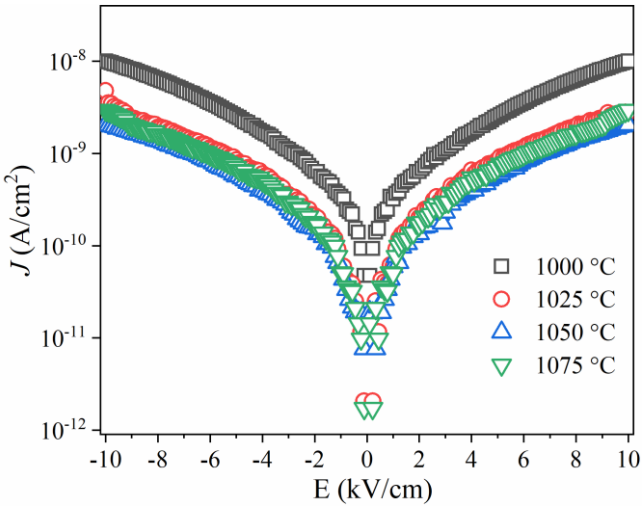

Figure 4.6. Variation in J with E for BNT specimens sintered at 1000 °C – 1075 °C.

At high E (~ 10 kV/cm), the J decreases with T_s up to 1050 °C due to decrease in size of grain boundaries that act as defect sites or trapping center for the charge carriers. Above 1050 °C, the increase in J indicates the growth of defects as already suggested by dielectric measurements.

4.1.6 Ferroelectric study

The ferroelectric behavior of BNT specimens sintered at 1000 °C – 1075 °C is confirmed by their *RT P-E* loops at 1 Hz as shown in **Figure 4.7**(a). A well saturated hysteresis has been observed for all the specimens. It is observed that the BNT specimen sintered at 1000 °C exhibits lossy FE hysteresis behavior due to its poor densification. With increase in T_s, the E_c decreases till the BNT specimen sintered at 1050 °C. However, E_c rises for BNT sintered at 1075 °C hints the growth of defects. The variation in P_s with T_s also follows the same trend as that of E_c. However, there is no significant change in P_r for the samples sintered at 1025 °C – 1075 °C. The variation in P_s, P_r and E_c with T_s has been tabulated in **Table 4.3**.

Table 4.3. P_s, P_r, E_c, d_{33}^* and d_{33} for BNT ceramics sintered at 1000 °C – 1075 °C.

T_s (°C)	P_s (μC/cm^2)	P_r (μC/cm^2)	E_c (kV/cm)	d_{33}^* (pm/V)	d_{33} (pC/N)
1000	35.64	32.93	46.6	71.4	47±5
1025	39.61	29.51	38.19	89.1	69±4
1050	39.98	28.67	35.73	105.2	78±2
1075	39.36	28.76	37.09	99	72±4

The variation in S, d_{33}^* and d_{33} with T_s are represented in **Figure 4.7**(b-d). The values of S, d_{33}^* and d_{33} first increase to 1050 °C also supported the rise in polarizability. Above 1050 °C, the decrease in S, d_{33}^* and d_{33} response suggest the growth of defects is not suitable for piezoelectric response. Therefore, it can be concluded from these findings that the BNT sintered at 1050 °C is suitable candidate for synthesizing *ME* composite. Thus, for 0-3 *ME* composite the T_s = 1050 °C is crucial for achieving good d_{33}.

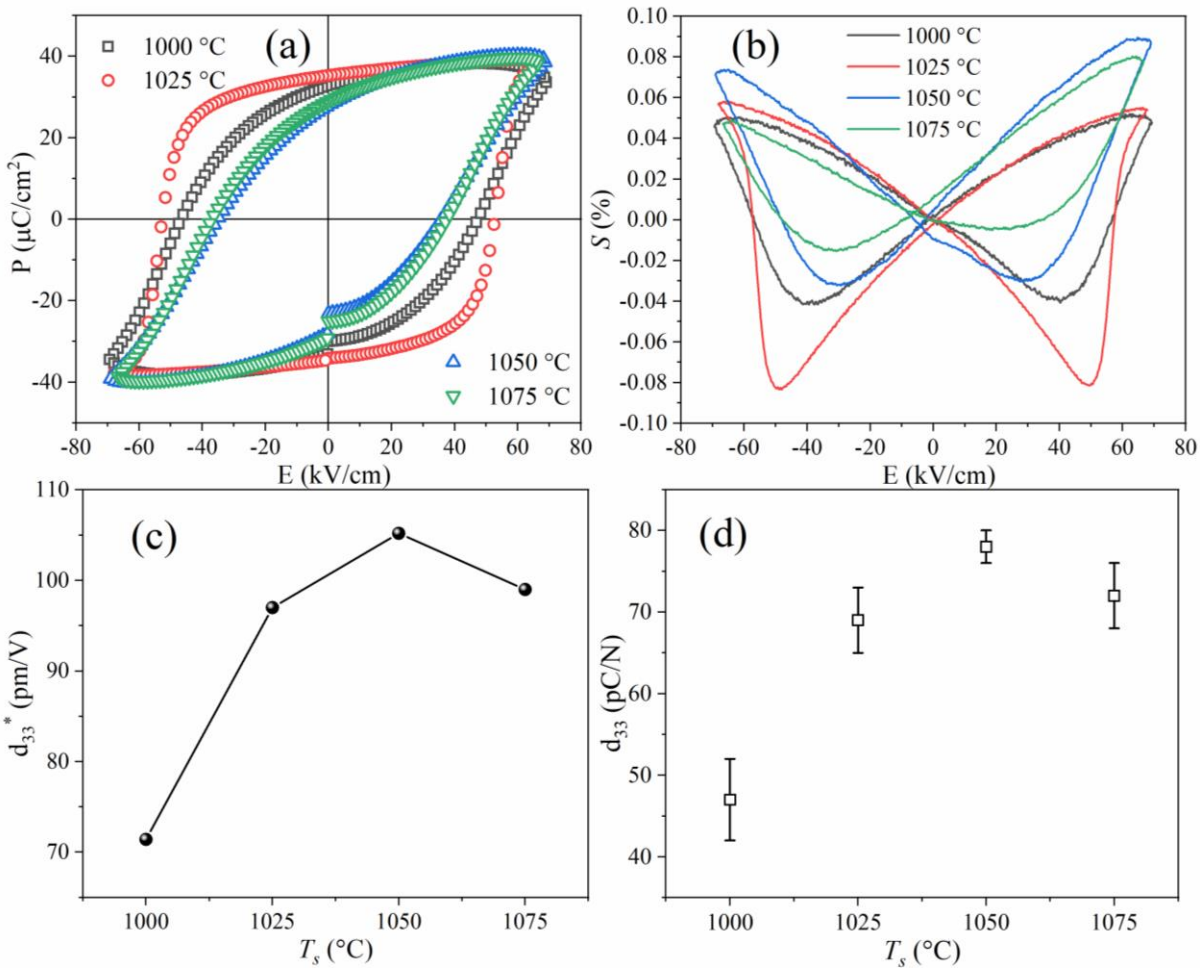

Figure 4.7. Variation in (a) *P-E* and (b) *S-E* loops, (c) d_{33}*, and (d) d_{33} of BNT specimens with the variation in sintering temperature.

4.2 Synthesis and optimization of BNKMT

The BNKMT has been synthesized via sol-gel and solid-state reaction method and calcined at 600 °C and 900 °C for 3h respectively. A PE material with optimized composition shows high saturation polarization (P_s), low coercivity (E_c) and high electro-strain (S). BNKMT is a ternary compound, which shows maximum properties at the morphotropic phase boundary. The

composition depicted in **Table 4.4** are investigated in the vicinity if MPB. It has been observed that $72.5Bi_{0.5}Na_{0.5}TiO_3$-$22.5Bi_{0.5}K_{0.5}TiO_3$-$5BiMg_{0.5}Ti_{0.5}O_3$ (BNKMT) possess relatively better FE and piezoelectric properties. Henceforth, BNKMT has been chosen for synthesizing *ME* composites.

Table 4.4. Variation in the P_s, E_c and S for the ternary BNT-BKT-BMT solid solutions.

Composition	$\boldsymbol{P_s}$ **(μC/cm²)**	$\boldsymbol{E_c}$ **(kV/cm)**	$\boldsymbol{S}$ **(%)**
$72.5Bi_{0.5}Na_{0.5}TiO_3$-$22.5Bi_{0.5}K_{0.5}TiO_3$-$5BiMg_{0.5}Ti_{0.5}O_3$ (BNKMT)	37.21	13.32	0.23
$72Bi_{0.5}Na_{0.5}TiO_3$-$23Bi_{0.5}K_{0.5}TiO_3$-$5BiMg_{0.5}Ti_{0.5}O_3$	36.58	13.87	0.21
$73Bi_{0.5}Na_{0.5}TiO_3$-$22Bi_{0.5}K_{0.5}TiO_3$-$5BiMg_{0.5}Ti_{0.5}O_3$	36.47	13.95	0.21
$73Bi_{0.5}Na_{0.5}TiO_3$-$23Bi_{0.5}K_{0.5}TiO_3$-$4BiMg_{0.5}Ti_{0.5}O_3$	35.83	14.57	0.19
$72Bi_{0.5}Na_{0.5}TiO_3$-$24Bi_{0.5}K_{0.5}TiO_3$-$4BiMg_{0.5}Ti_{0.5}O_3$	36.02	14.12	0.20
$72Bi_{0.5}Na_{0.5}TiO_3$-$22Bi_{0.5}K_{0.5}TiO_3$-$6BiMg_{0.5}Ti_{0.5}O_3$	35.59	14.83	0.18

The phase analysis of BNKMT samples has been depicted in **Figure 4.8**, that revealed the formation of a pristine perovskite crystal structure for both the sol-gel and solid-state derived BNKMT specimens. The distinct diffraction peaks have been indexed with the JCPDS database card no. 36-0340.

Further, the pure BNKMT phase has been subjected to sintering at 1000 °C - 1075 °C for 1 h and the effect of sintering temperature on its phase, structural, dielectric and FE properties have been investigated.

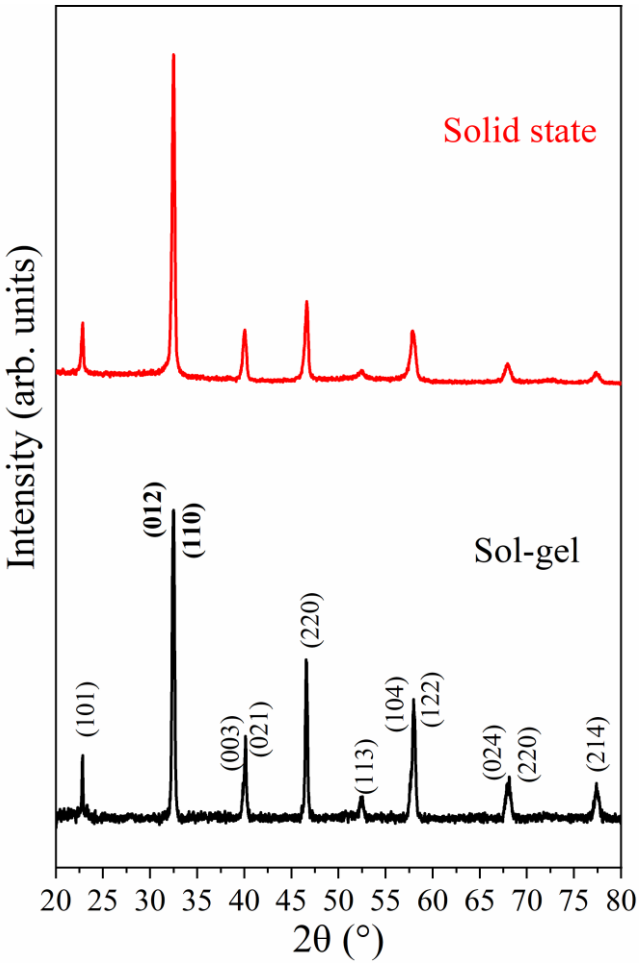

Figure 4.8. XRD pattern of sol-gel and solid-state driven BNKMT calcined at 600 °C and 900 °C for 3h respectively.

4.2.1 Phase analysis

Figure 4.9 shows the XRD pattern of BNKMT ceramics sintered at 1000 °C – 1075 °C. The diffraction peaks are matched with the JCPDS card number 36-0340 (**Figure 4.9**(a)) that reveals the formation of perovskite crystal structure. The diffraction peaks slightly shift towards higher angle with the T_s (**Figure 4.9**(b)) that reveals the strain induction. Moreover, the increase in crystallite size (D) with T_s has been observed (**Table 4.5**), which is calculated using Scherrer's formula (see equation 3.1). There are no traces of impurity peak up to 1040 °C. However, above 1040 °C, there is a formation of secondary phase (denoted by * in XRD pattern). The phase is found to be orthorhombic $K_4Ti_3O_8$ (JCPDS: 041-0167), which forms due to the volatility of Bi and Na elements. Further, the intensity of the impurity peak increases with temperature suggests the growth of secondary phase at high sintering temperature.

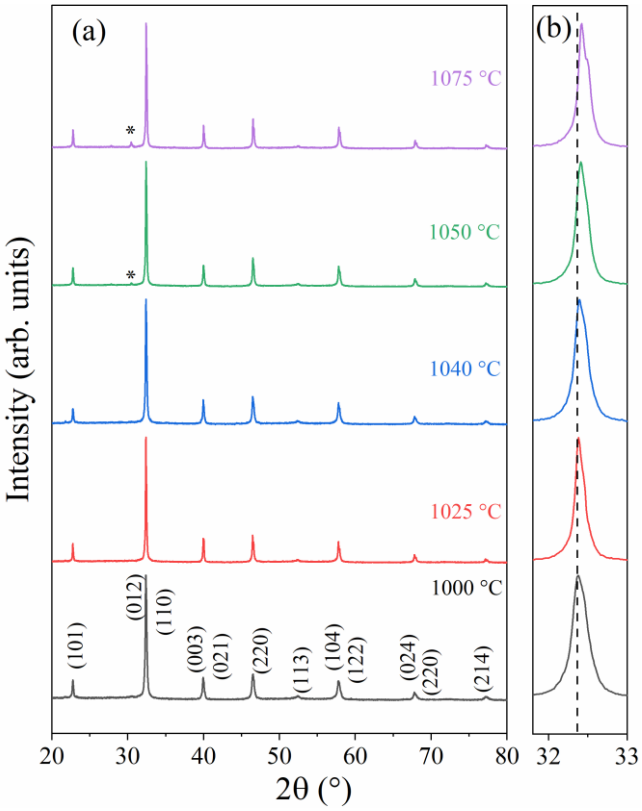

Figure 4.9. XRD pattern of sintered BNKMT ceramics at 1000 °C – 1075 °C in 2θ range (a) 20°-80° and (b) 31.8°-33°.

Table 4.5. Crystallite size of BNKMT ceramics sintered at 1000 °C – 1075 °C.

T_s (°C)	D (nm)
1000	25.67
1025	30.05
1040	33.82
1050	35.69
1075	39.12

To confirm the occurrence of the MPB, Rietveld analysis of BNKMT has been carried out and depicted in **Figure 4.10**.

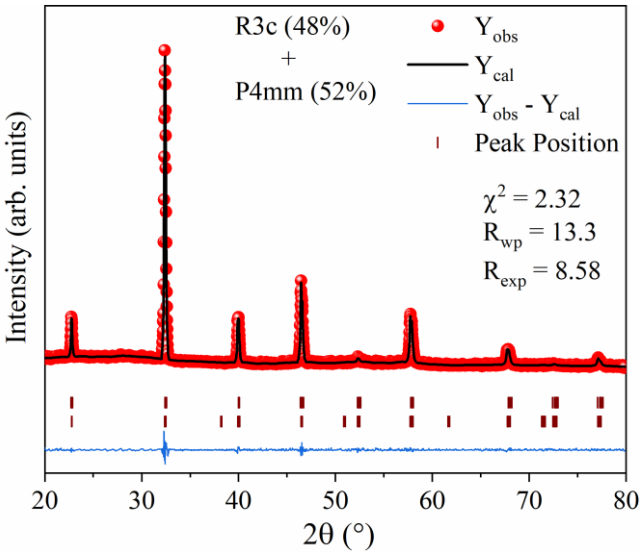

Figure 4.10. Refined XRD patter if BNKMT ceramics sintered at 1040 °C for 1h. The red solid circles, continuous black line and blue line represent the observed pattern, calculated pattern, and difference curve between the observed and calculated profiles. The wine color vertical bars denote the position of reflections.

The Rietveld refinement is employed with pseudo-Voigt function and has been executed with *R3c* + *P4mm* space groups, which represents the occurrence of MPB.The parameters such as observed intensity ($Y_{obs.}$), theoretical intensity ($Y_{cal.}$), their difference ($Y_{obs.}$-$Y_{cal.}$), and Bragg's positions have also been represented. The Rietveld refined factors (*R*-factors), i.e., R_{wp} and R_{exp}, and goodness of fitting (χ^2) determines the precision of fitting. The experimental data is in close agreement with the theoretical one.

4.2.2 Raman study

Further, Raman spectroscopy has been used to investigate the effect of T_s on the optical vibration modes of BNKMT. All specimens exhibit conventional 3 Raman bands of the ABO_3 perovskite structure [133], which are designated as X, Y and Z and represented in **Figure 4.11**(a). The X band determines the A-O vibrations, whereas Y and Z represent the B-O and B-O_6 octahedra vibrations respectively. These bands become narrower with the T_s upto 1040 °C, which indicates the progressive reduction of phonon scattering from the grain boundaries [134]. A representative of variation in full-width at half maxima (FWHM) with T_s for Y-band is demonstrated in **Figure 4.11**(b).

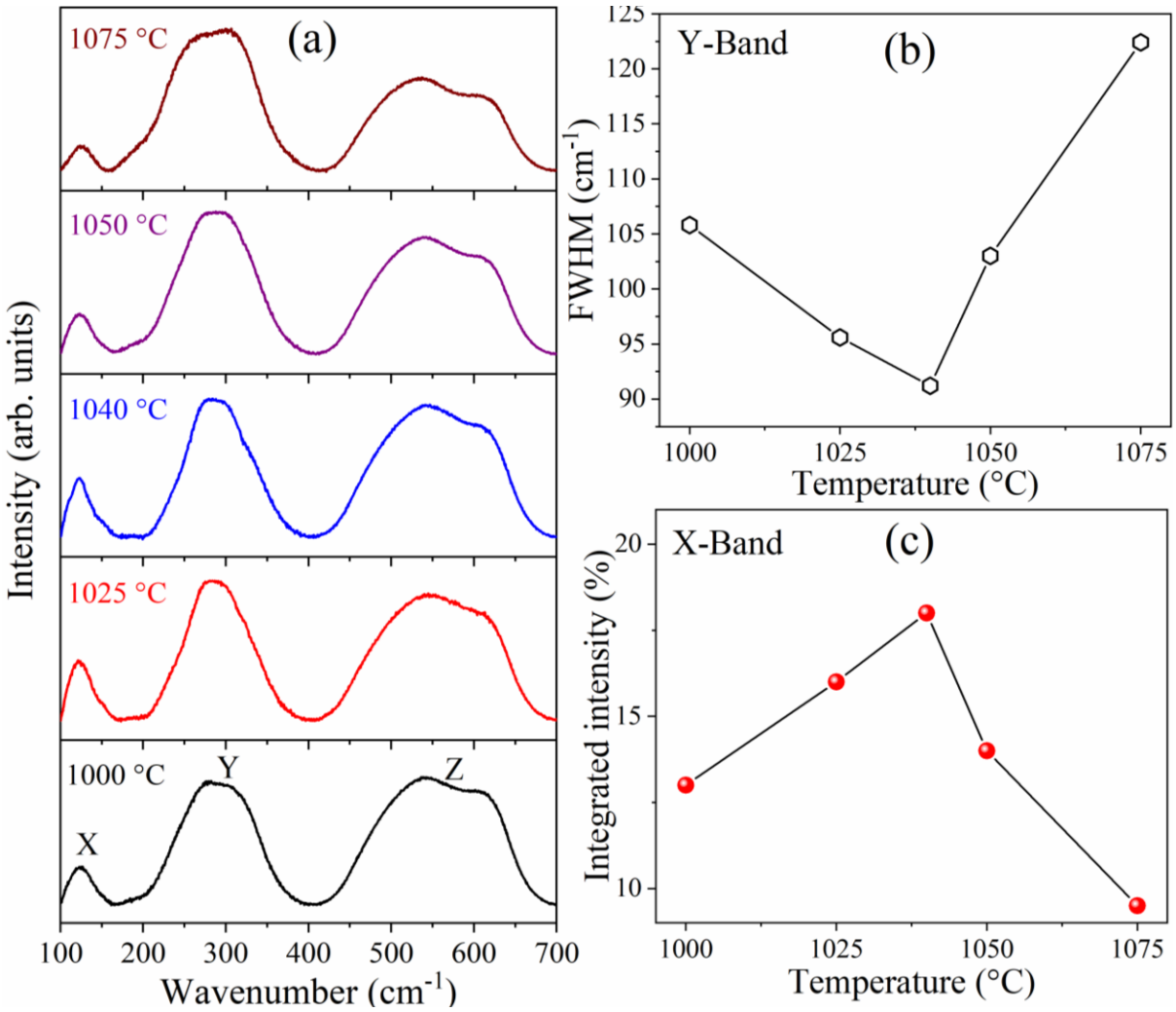

Figure 4.11. (a) Raman spectrum of BNKMT specimens sintered at 1000 °C – 1075 °C. Variation in (b) FWHM of Y-band and (c) integrated intensity of X-band with T_s.

The decrease in FWHM with the T_s attributes to the increase in crystallinity and reduction in the grain boundaries (consisting disordered atoms that causes phonon scattering). Above 1040 °C, secondary phase formation instigate the softening of phonon frequency [138] (as already indicated by XRD pattern), which is also supported by the decrease in Z-band intensity. The decrease in X band intensity above 1040°C (**Figure 4.11**(c)) suggest the defects at A-site in the perovskite structure produces secondary phase.

4.2.3 Microstructural analysis

Further, the effect of variation in T_s on the microstructure of BNKMT has been examined and represented in **Figure 4.12**. It can be seen that the increase in T_s leads to coarsening of grains. Below 1050 °C, the grains have nearly cube like shape. However, at 1050 °C and 1075 °C,

some of the grains shows abnormal rod-like shape, which suggests the formation of secondary phase, i.e., $K_4Ti_3O_8$ [139], which corroborates to the XRD and Raman analysis.

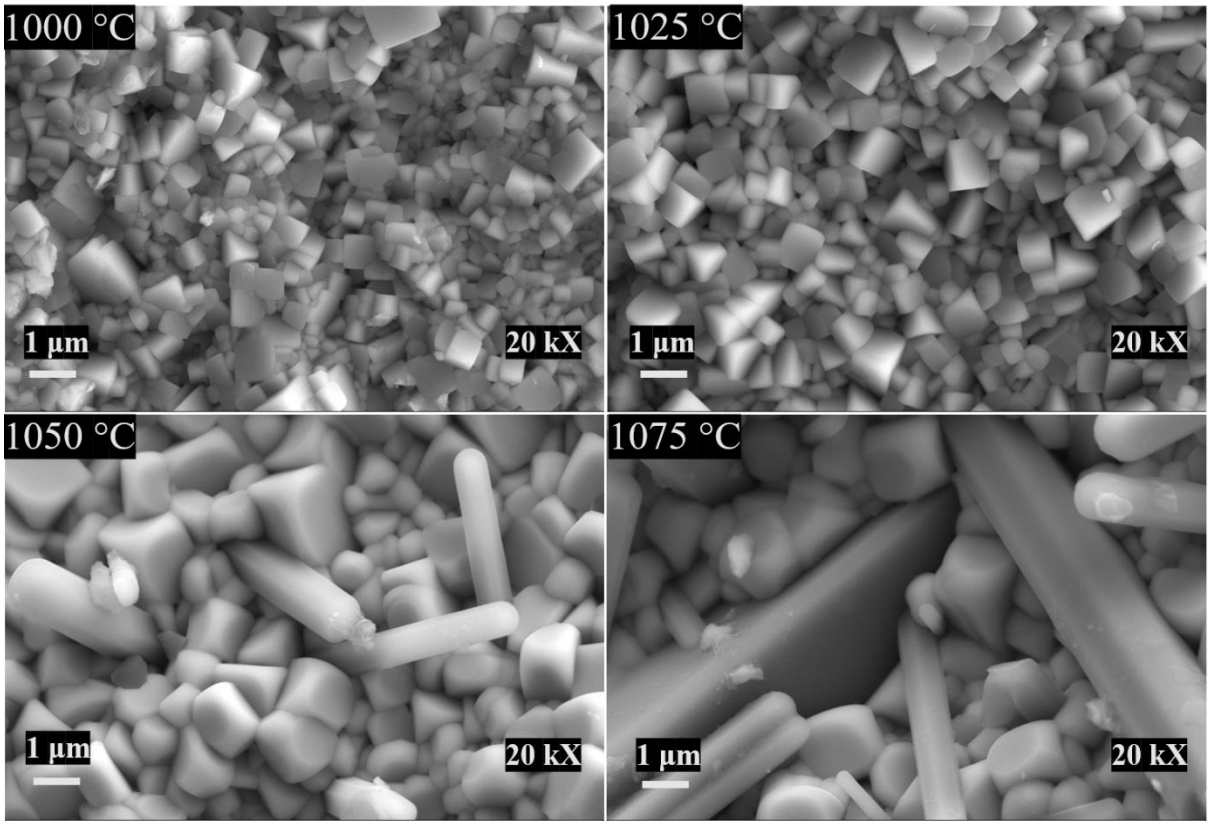

Figure 4.12. SEM micrograph of BNKMT ceramics sintered at 1000 °C – 1075 °C for 1h.

To confirm distinct phases, the elemental mapping of BNKMT ceramics (sintered at 1075 °C) is shown in **Figure 4.13**. A representative secondary electron micrograph of BNKMT specimen at 10 kX has been shown in **Figure 4.13** (a), and the corresponding elemental mapping is depicted in **Figure 4.13**(b). The mapping reveals two distinct phases, where cube like grains corresponds to phase pure BNKMT and the abnormal rod-like grains are found to be Bi and Na deficient. The observed secondary phase probably has its own domain structure, which is different from the regular domain structure of BNKMT grains. The occurrence of such morphology significantly influences the electrical properties of a ceramics [140,141].

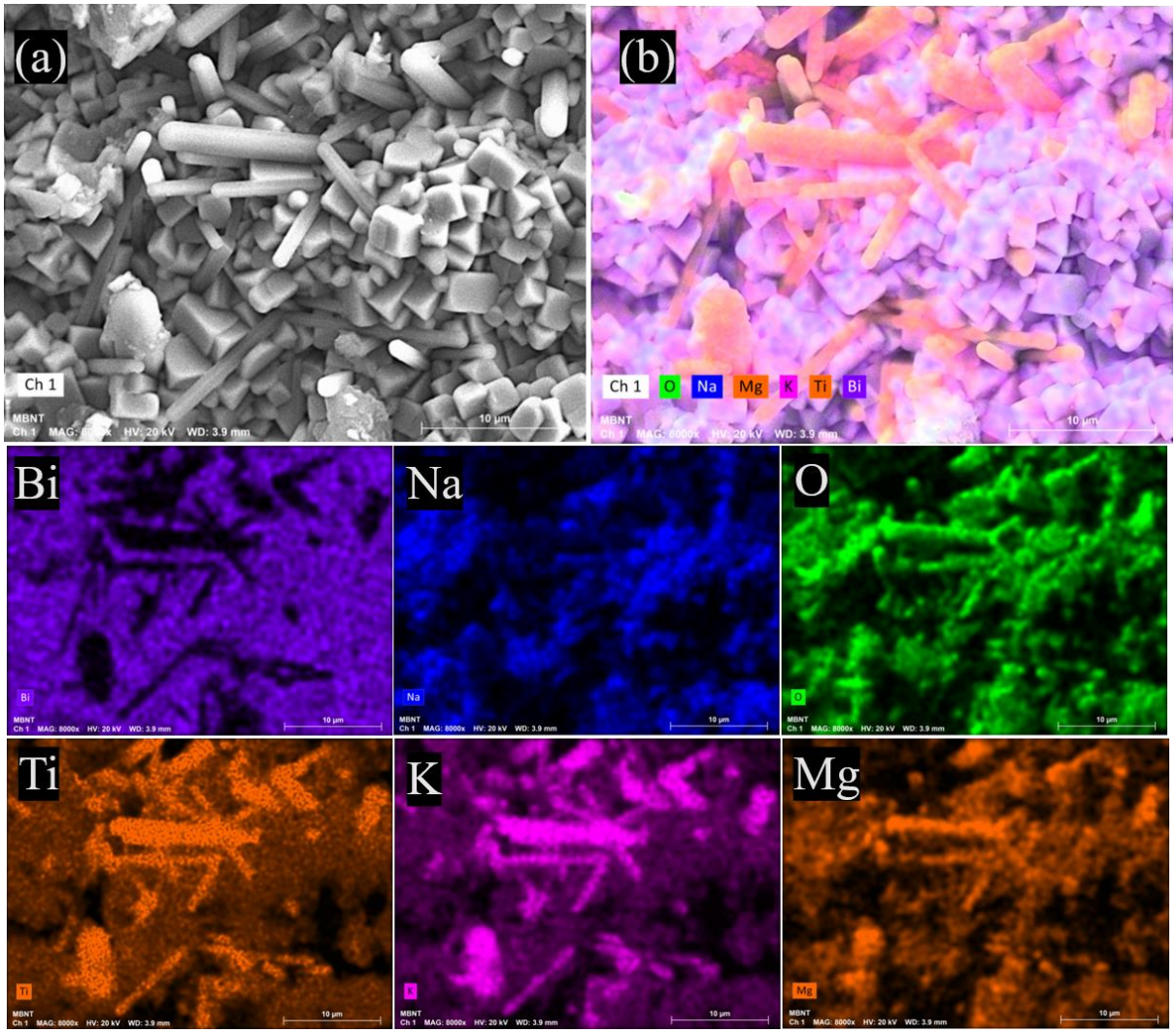

Figure 4.13. (a) SEM micrograph and (b) elemental mapping of BNKMT ceramics sintered at 1075 °C for 1h.

4.2.4 Dielectric study

The *RT* dielectric measurements in *f* range 10^2 Hz - 10^6 Hz for BNKMT ceramics sintered at 1000 °C – 1075 °C is represented in **Figure 4.14**. The ε_r and tan δ decreases abruptly with *f* upto 10^4 Hz that support the reduction of space charge carriers. The ε_r increases and tan δ decreases with T_s (at 1kHz) upto 1040 °C depicts the increase in polarizability and decline in the losses with the larger grains. However, above 1040 °C decrease in ε_r and increase in tan δ (**Table 4.6**) support the growth of secondary phase.

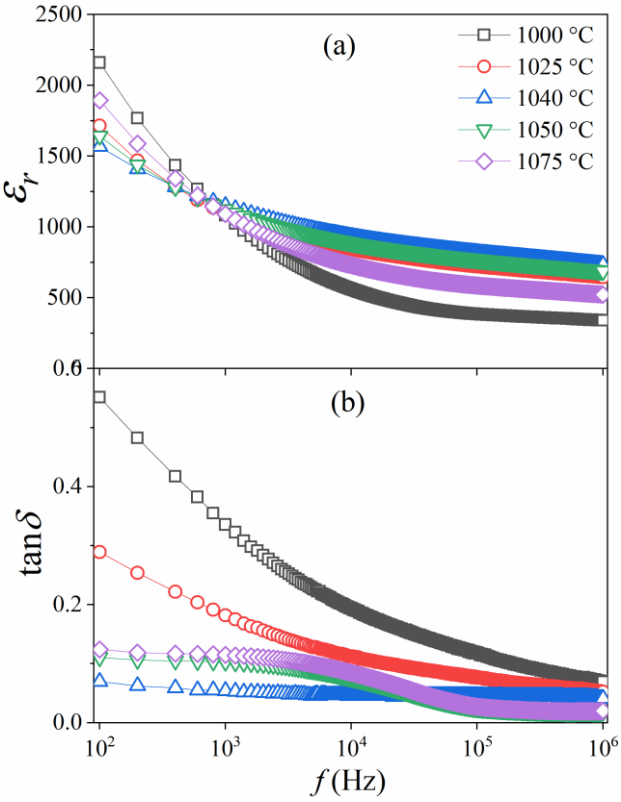

Figure 4.14. Variation in f with (a) ε_r and (b) tan δ for BNKMT ceramics sintered at 1000 °C – 1075 °C for 1h.

Table 4.6. ε_r and tan δ at 1 kHz for sintered BNKMT ceramics.

T_s (°C)	ε_r	tan δ
1000	1081	0.33
1025	1098	0.18
1040	1150	0.05
1050	1123	0.103
1075	1091	0.119

4.2.5 Leakage current measurement

The *RT J-E* curves for BNKMT ceramics has been recorded and depicted in **Figure 4.15.** Variation in J with E for BNKMT ceramics sintered at 1000 °C – 1075 °C. The sharp increase in J till 1 kV/cm attributes to the space charge conduction. Above 1 kV/cm, gradual increase of J indicates the contribution of grain boundaries, and Poole-Frenkel emission [136,137]. At high E (~ 10 kV/cm), the J decreases with T_s upto 1040 °C due to decrease in size of grain

boundaries that act as defect sites or trapping center for the charge carriers. Above 1040 °C, the increase in *J* indicates the contribution of defects.

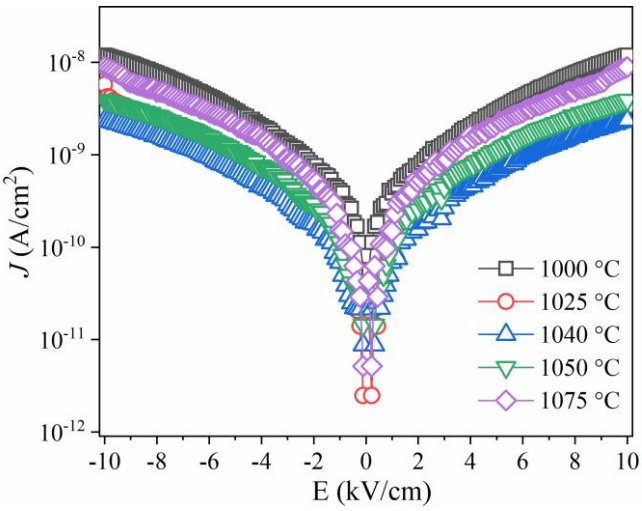

Figure 4.15. Variation in *J* with *E* for BNKMT ceramics sintered at 1000 °C – 1075 °C.

4.2.6 Ferroelectric study

The FE and piezoelectric properties of BNKMT ceramics has been investigated and shown in **Figure 4.16** and **Figure 4.17** respectively. The BNKMT ceramics with T_s < 1040 °C exhibits typical relaxor FE loops (no sharp switching of *I* with *E* also corroborates to relaxor behavior) as shown in **Figure 4.16**(a-c). The gradual increase in maximum polarization (P_{max}) and P_r without any significant change in threshold field (E_f) (indicated by peak of polarization current (*I*)) with T_s has been observed. This attribute to the increase in grain size, which results in the growth of stable domains with relatively lesser domain walls. For T_s > 1040 °C, the pinching of *P-E* loop has been observed as represented in **Figure 4.16**(d) & (e). Such characteristic behavior is also supported by its polarization current (*I*) *vs* E curves, where the observation of two *I* hump in positive *E* region reflects the forward switching *E* (E_f, field required for the anti-ferroelectric (AFE) to FE transition) and backward switching *E* (E_b, field required for the FE to AFE transition) [142]. The E_f of the ceramics shift towards lower *E*, whereas E_b at higher *E* as the size of both cubic (FE phase) and abnormal-rod like grains (AFE phase) increases with T_s that advances the domains switching. The existence of both FE and AFE characteristics in a ceramic could be favorable for the observation of high electro-strain (*S*) [143,144].

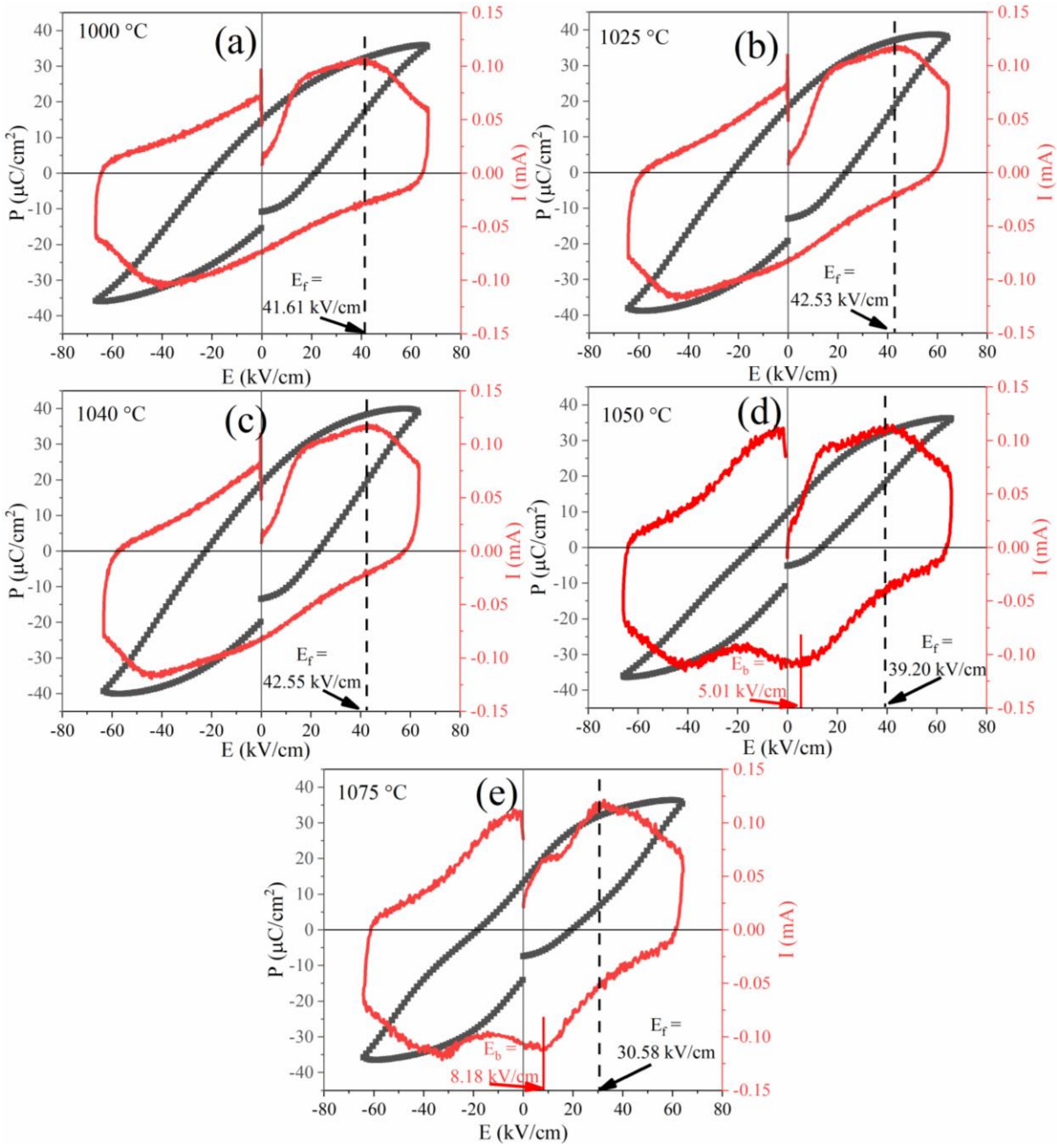

Figure 4.16. Variation in *P* and *I* with *E* for BNKMT ceramics sintered at (a) 1000 °C, (b) 1025 °C, (c) 1040 °C, (d) 1050 °C and (e) 1075 °C.

Therefore, the piezoelectric behavior of the BNKMT ceramics has been studied as shown in **Figure 4.17**. The bipolar *S*-*E* curve of the BNKMT ceramics sintered at various temperature in range 1000 °C to 1075 °C has been shown in **Figure 4.17**(a). All the specimens exhibit typical butterfly *S*-*E* loop, where maximum *S* increases gradually with the T_s upto 1040 °C as shown in **Figure 4.17**(b). This supports the increase in P_{max} with T_s (as shown in **Figure 4.16**(a-c)). Interestingly, an abrupt increase in *S* has been observed for the ceramics have T_s > 1040 °C.

This may be due to the contribution of the local strain caused by the defect domains. These domains act as pinning center for the domain walls. When an *E* is introduced, the domain walls undergo a necessary realignment to conform to *E* direction. However, the presence of defect domains introduces obstacles that impede the mobility of domain walls and causes the high *S* within the material. Therefore, giant *S* of 0.31 % (S_{max}/E_{max} ~ 502 pm/V) has been observed for BNKMT specimen sintered at 1075 °C. Further, the d_{33} do not follow the same trend as exhibited by *S* with T_s (**Figure 4.17**(b)). The d_{33} increases with T_s upto 1040 °C and decreases thereafter. Such behavior supports the pure FE behavior of BNKMT. An observation of high d_{33} (~ 189 pC/N) for BNKMT specimen with T_s = 1040 °C suggest the potential of material that can be used as a magnetostrictive phase for the synthesis of *ME* composite.

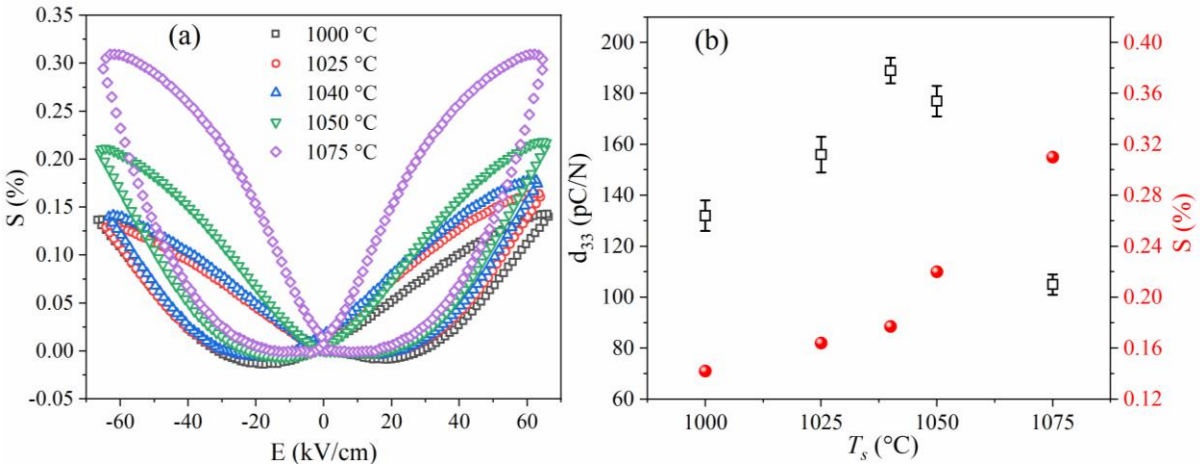

Figure 4.17. (a) *S-E* curve and (b) Variation in maximum *S* and d_{33} with the T_s for BNKMT ceramics sintered at various temperatures.

4.3 Synthesis and optimization of NFO

Similar to PE phases, the magnetic NFO has also been synthesized via sol-gel and solid-state reaction route. Both the sol-gel and solid-state derived NFO has been calcined at 900 °C for 3 h. Their XRD pattern reveals the formation of inverse spinel NFO without any formation of secondary phase as represented in **Figure 4.18**. Their diffraction peaks are indexed with the JCPDS card: 10-0325. Thereafter, the calcined samples were sintered at 1050 °C – 1200 °C for 1 h. Further, the effect on its phase, structural and magnetic properties has been investigated.

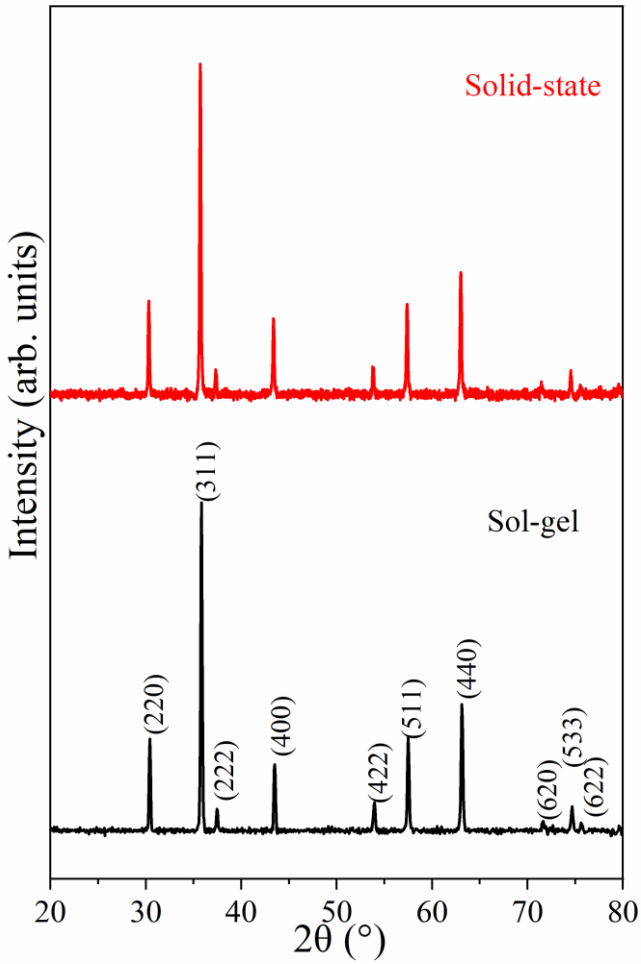

Figure 4.18. XRD pattern of sol-gel and solid state derived NFO calcined at 900 °C for 3 h.

4.3.1 Phase analysis

Figure 4.19 displays the XRD pattern of NFO ceramics sintered at 1050 °C – 1200 °C for 1h. The diffraction peaks are matched with the JCPDS card: 10-0325 that reveals the formation of inverse spinel NFO. It can be seen that there are no traces of impurity peak has been observed throughout the T_s range. Further, the Scherrer's formula (equation 3.1) is used to evaluate the *D* and displayed in **Table 4.7**. It can be seen that the increase in *Ts* leads to increase *D*.

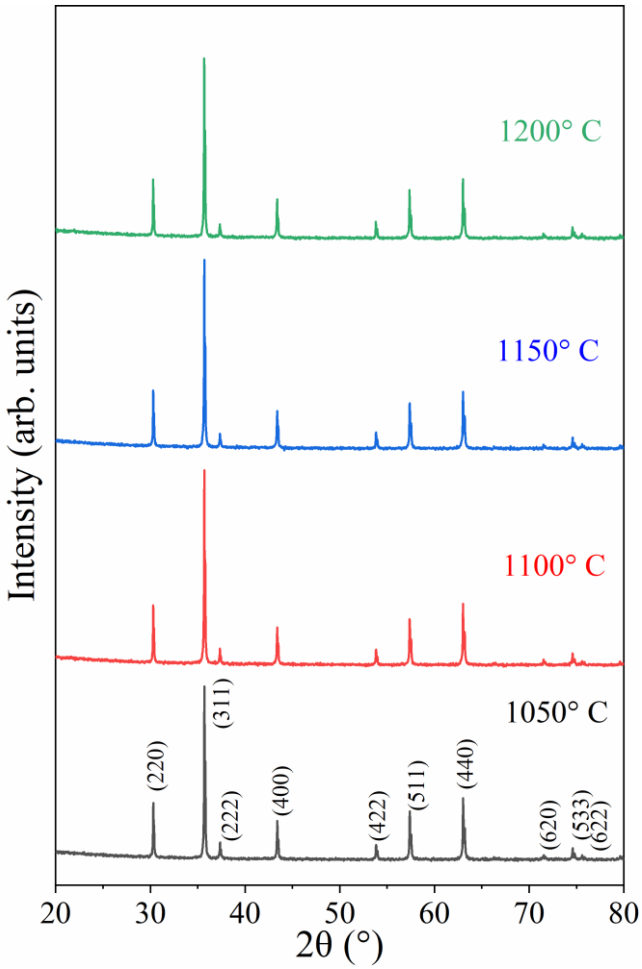

Figure 4.19. XRD pattern of NFO specimens sintered at 1050 °C – 1200 °C for 1 h.

Table 4.7. Crystallite size of BNKMT ceramics sintered at 1000 °C – 1075 °C.

T_s (°C)	D (nm)
1050	35.73
1100	38.42
1150	41.18
1200	44.37

4.3.2 Raman study

In order to investigate the vibrational modes in NFO, its Raman spectrum has been investigated in range 300 cm^{-1} to 800 cm^{-1}, where three octahedral E_g, F_{2g} (2) and F_{2g} (3), and one tetrahedral

A_{1g} band of NFO ceramics is clearly observed and represented in **Figure 4.20**. The A_{1g} and E_g bands represent the symmetric stretching and bending of metal-oxygen bonds respectively. On the other hand, F_{2g} bands related to as-symmetric stretching [145]. It can be seen that there has no significant impact of T_s on the vibrational modes of NFO.

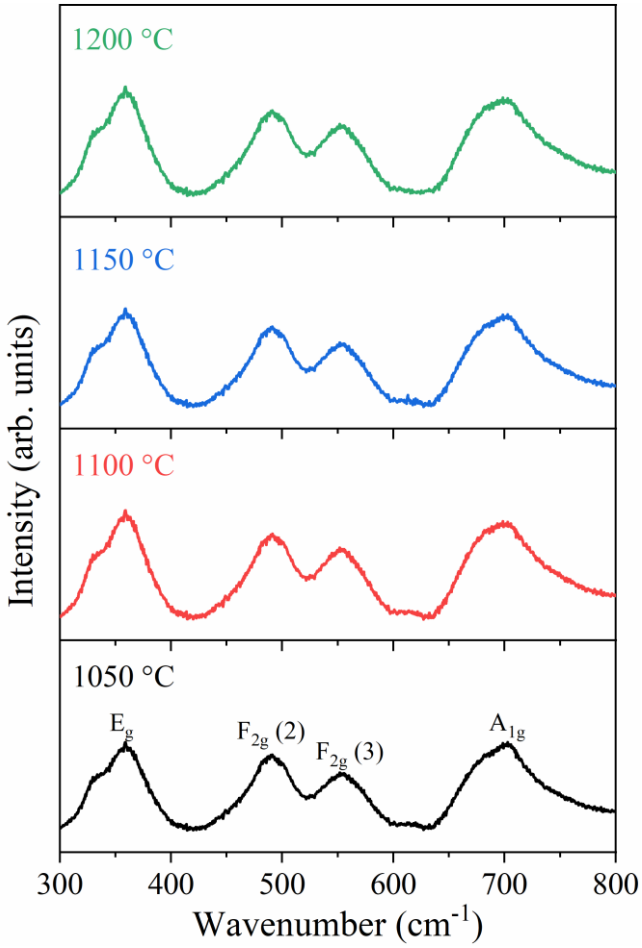

Figure 4.20. Raman spectrum of sintered NFO specimens in range 300 cm^{-1} -800 cm^{-1}.

4.3.3 Microstructural analysis

Further, the effect of variation in T_s on the microstructure of NFO has been investigated and depicted in **Figure 4.21**. It can be seen that increase in T_s leads to the growth of grains. The grain growth is very crucial in order to achieve good magnetic properties. The average grain size is 1.06 µm, 1.53 µm, 1.89 µm and 2.43 µm for the NFO ceramics sintered at 1050 °C, 1100 °C, 1150 °C and 1200 °C respectively.

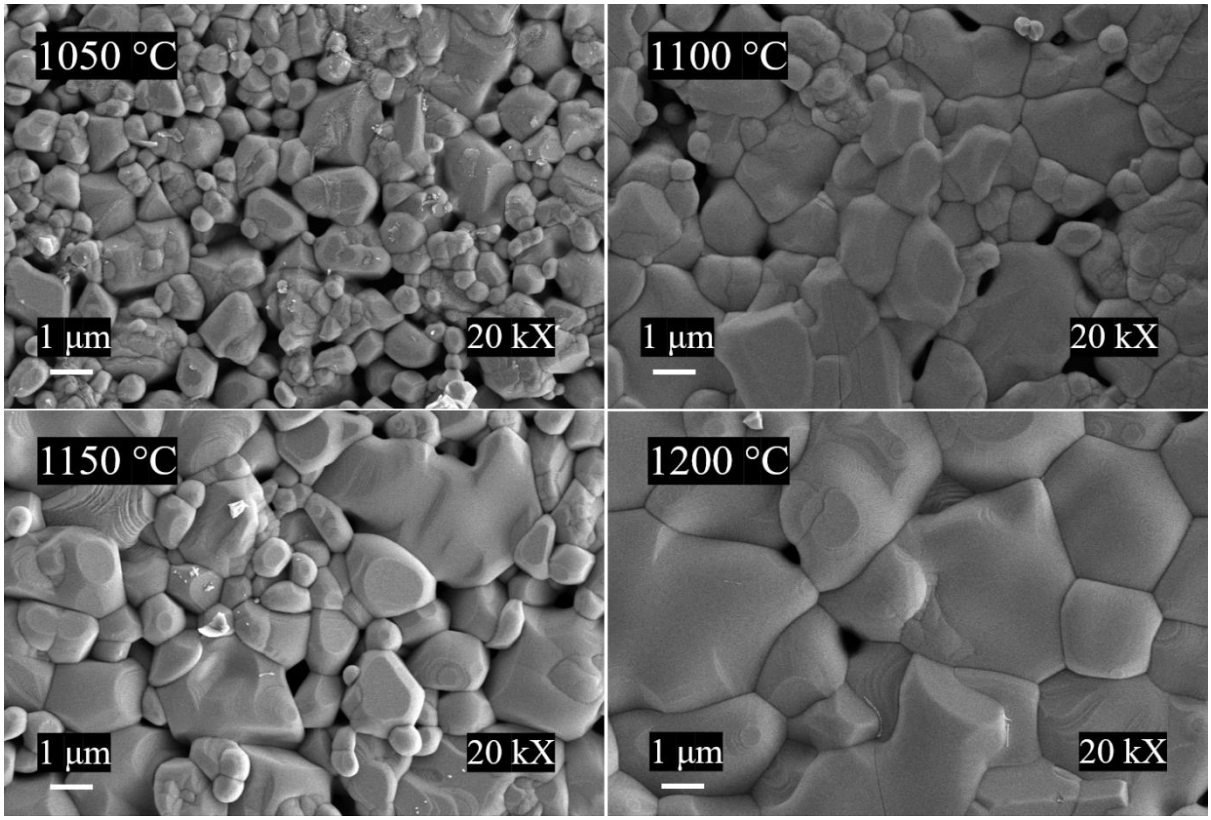

Figure 4.21. SEM micrograph of NFO ceramics sintered at 1050 °C – 1200 °C for 1 h.

4.3.4 Magnetic behavior analysis

The magnetic properties of NFO ceramics sintered at 1050 °C – 1200 °C for 1h has been investigated as shown in **Figure 4.22**. **Figure 4.22**(a) depicts the magnetic hysteresis loops, where all sintered specimens exhibit soft FM behavior. The increase in T_s enhances the M_s as displayed in **Figure 4.22**(b). Further, to analyze the qualitative PM coefficient, their dM^2/dH *vs* H plot has been investigated as shown in **Figure 4.22**(c). The dM^2/dH initially increases with H upto its peak value and then decreases. The maximum value of dM^2/dH increases with T_s and observed maximum for 1200 °C sintered NFO as displayed in **Figure 4.22**(d). This indicates that the T_s of 1200 °C is suitable for achieving maximal PM properties.

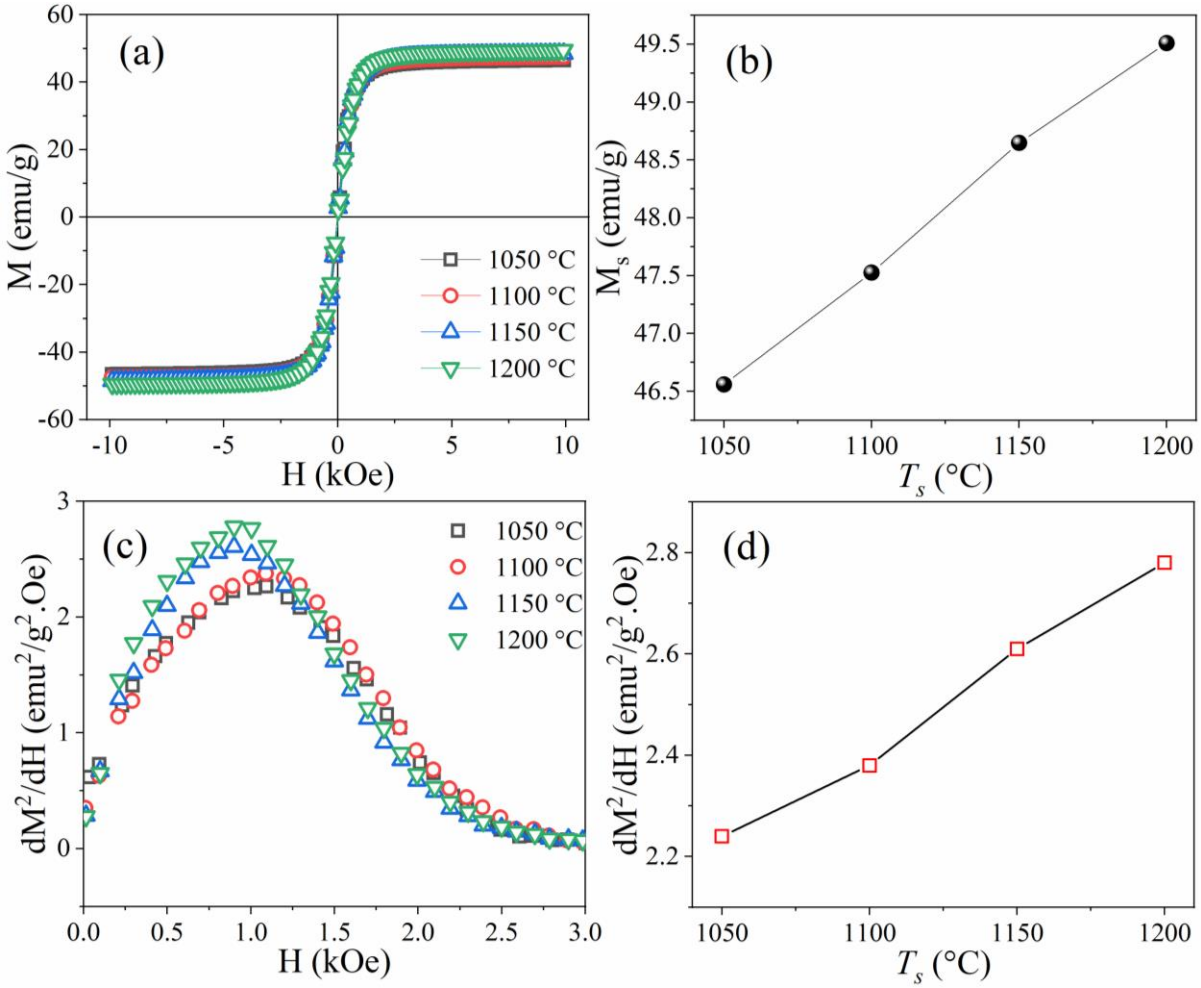

Figure 4.22. Variation in (a) *M-H* loop, (b) M_s, (c) dM^2/dH *vs H* curves and (d) maxima of dM^2/dH with T_s for NFO ceramics.

4.4 Effect of Zn substitution on piezomagnetism

It has been observed that the NFO specimen sintered at 1200 °C exhibit excellent magnetostrictive properties. To enhance piezomagnetism Zn has been substituted at Ni-site and its phase, structural and magnetic properties has been investigated.

4.4.1 Phase analysis

Figure 4.23 displays the XRD pattern of NZ_xFO (x = 0.0 - 0.5; Δx = 0.1) ceramics sintered at 1200 °C for 1 h. All peaks of NZ_xFO ceramics are matched with JCPDS card: 10-0325 that reveals the formation of cubic spinel ferrite. An absence of an additional peak confirms the lack of chemical reaction within the used sintering condition.

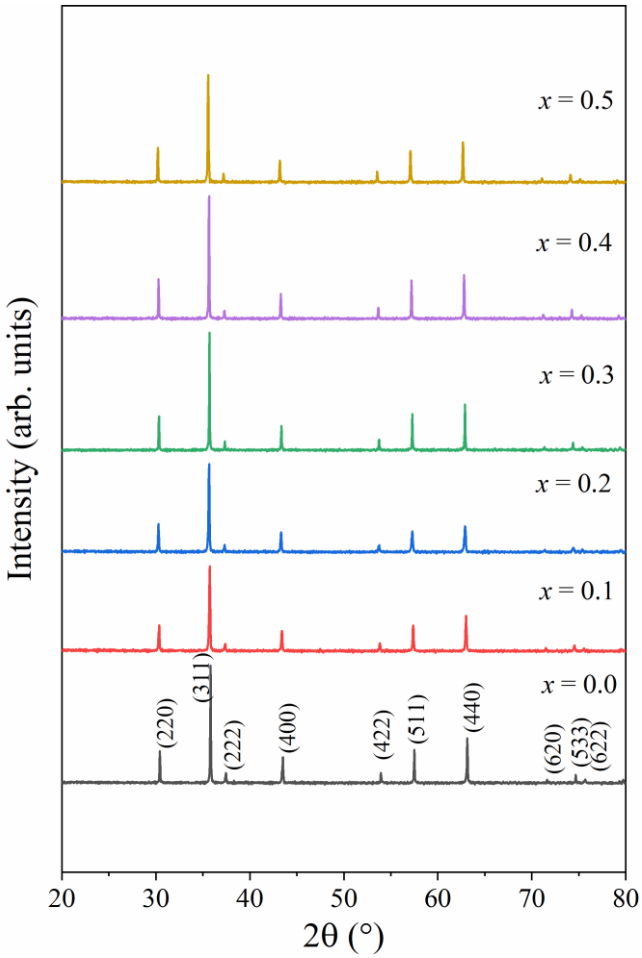

Figure 4.23. XRD pattern of NZ_xFO ceramics sintered at 1200 °C for 1h.

4.4.2 Raman spectroscopy

To confirm the site occupation by Zn-cation, Raman spectroscopy of NZ_xFO ceramics has been carried out from 400 cm^{-1} to 800 cm^{-1}, where two octahedral F_{2g} (2) and F_{2g} (3), and one tetrahedral A_{1g} band of NFO ceramics is clearly observed in **Figure 4.24**. It can be seen that Zn^{2+} substitution causes the splitting of both octahedral and tetrahedral bands (confirmed by extra deconvoluted green color peak for a particular band) that confirms the occupation of Zn^{2+} ions at their respective bands site. Moreover, area of the deconvoluted peak (green color) under A_{1g} is higher than each F_{2g} band, which suggests the preferential occupation of Zn^{2+} ions at A-site. Above $x > 0.3$, the splitting of F_{2g} decreases, that also support the inclination towards the $ZnFe_2O_4$ normal spinel structure.

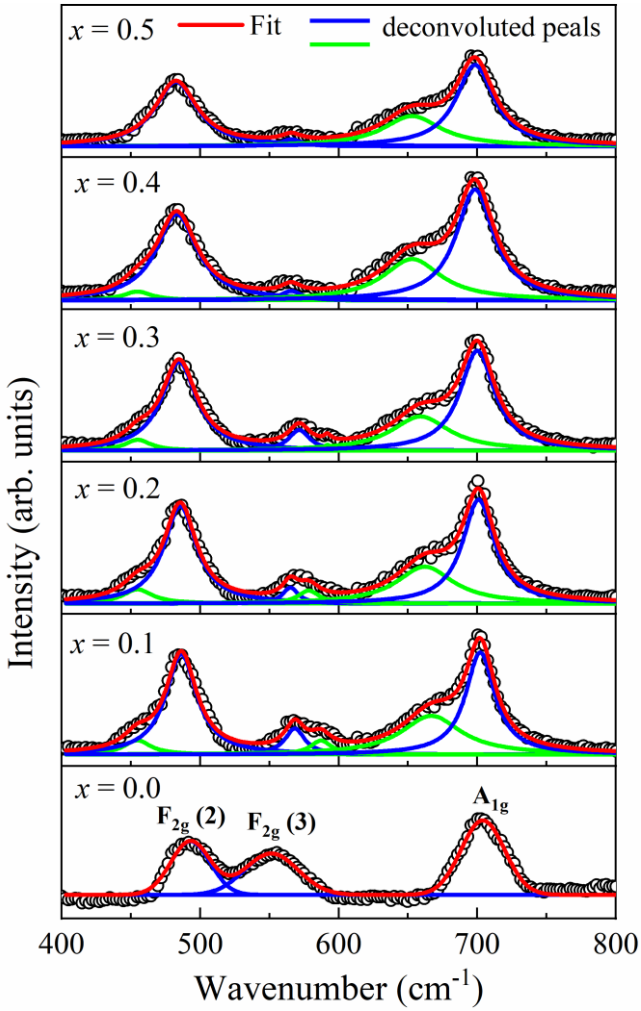

Figure 4.24. Raman spectrum of sintered NZ_xFO ceramics. Deconvoluted peaks in green and blue color depicts the occupation of Zn cations at their respective sites.

4.4.3 Microstructural analysis

Further, the microstructure of sintered NZ_xFO has been examined and displayed in **Figure 4.25**. It can be seen that a dense microstructure has been observed for all the ceramics which is crucial for sustaining charge during *ME* coupling.

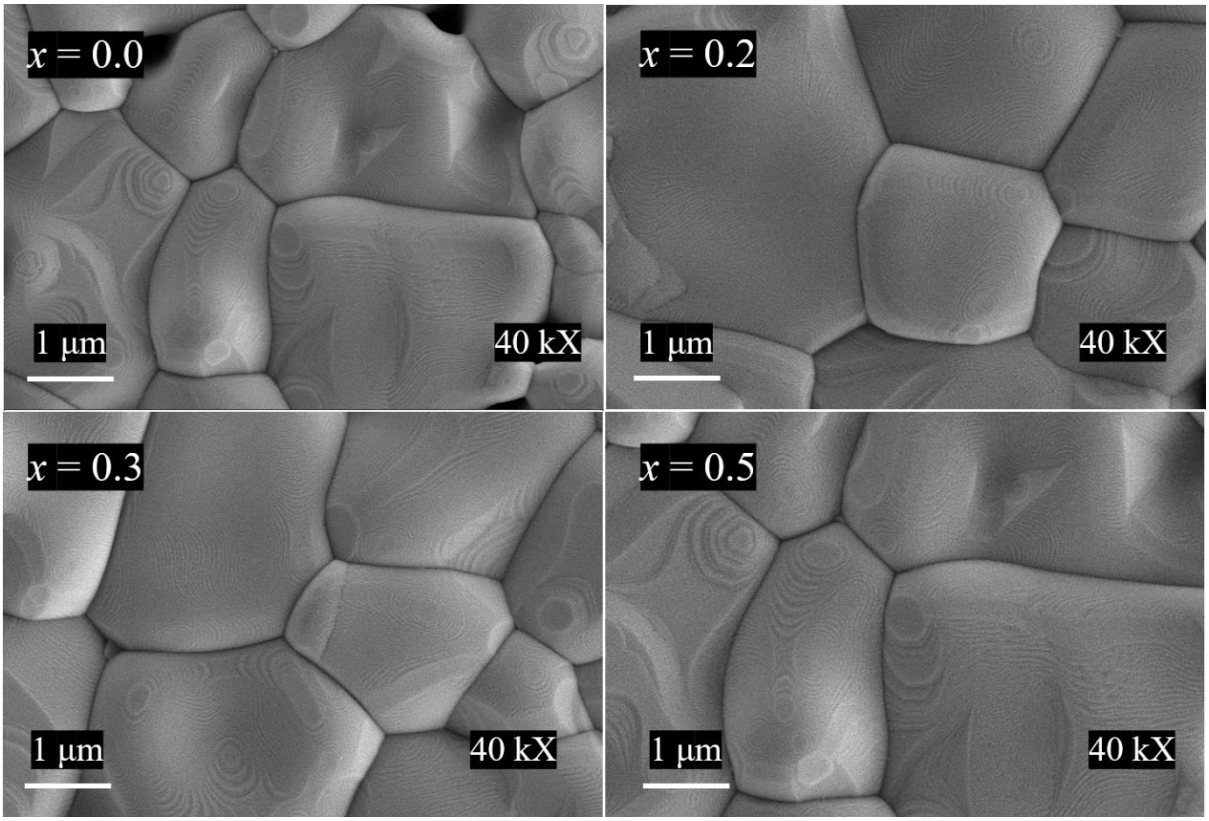

Figure 4.25. SEM micrographs of NZ_xFO ceramics at 40 kX magnification for the pellets sintered at 1200 °C for 1 h.

4.4.4 Magnetic behavior analysis

The magnetic properties of NZ_xFO ceramics have been investigated as shown in **Figure 4.26**. All the specimens exhibit slim magnetic hysteresis behavior as illustrated in Figure 4.25(a). The inclusion of Zn enhances the M_s as displayed in **Figure 4.26**(b). Further, to analyze the qualitative PM coefficient, their dM^2/dH *vs* H plot has been investigated as shown in **Figure 4.26**(c). The dM^2/dH is found to increase with Zn substitution till x = 0.3 and decreases afterwards (**Figure 4.26**(d)). However, M_s increases with Zn content till x = 0.5 as shown in **Figure 4.26**(b). This implies that there is no direct correlation between q_s and M_s. In conclusion, q_s is only correlated to the rate of change of M instead of M_s.

For better understanding of q_s, virgin M-H plot of NZ_xFO ceramics is investigated and shown in **Figure 4.27**(a). The initial slope of virgin M curves (straight line fitted) indicates the initial permeability (μ_i) of the ceramics, which is calculated by using formula, $M = \mu H$ [146]. The μ_i is found to increase with Zn substitution upto x = 0.3, which suggests the collinear magnetic ordering at B-site (see **Figure 4.27**(b)) [147,148].

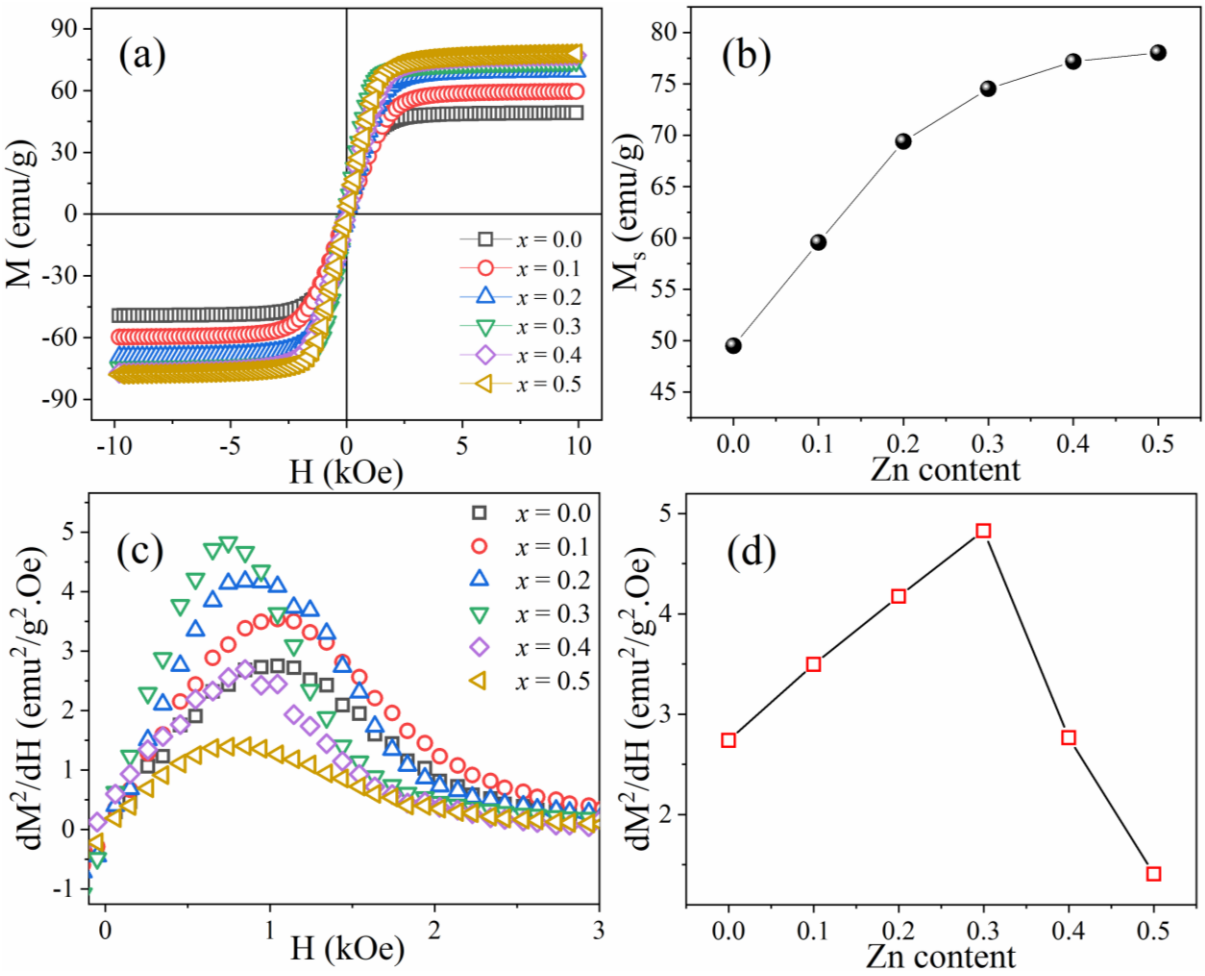

Figure 4.26. Variation in (a) *M-H* loop and (c) dM^2/dH *vs H*. (b) variation in M_s and d) maxima of dM^2/dH with the Zn substitution.

This is in accordance to Neel's two sublattice model that states the diamagnetic Zn^{2+} ions preferably occupy anti-parallel tetrahedral site (A-site) instead of occupying Ni^{2+} octahedral site (B-site), which causes the migration of Fe^{3+} ions from A-site to B-site that deteriorate the compensation mechanism exhibited by equal number of Fe^{3+} magnetic moments at both sites in NFO structure [145]. Above $x > 0.3$, the decrease in μ_i suggest the non-collinear Yafet-Kittel (Y-K) type of magnetic ordering (**Figure 4.27**(c)) due to the strong preference of $ZnFe_2O_4$ normal spinel structure [147,148]. Previously, Mossbauer and neutron diffraction study of NZ_xFO reveals the occupation of Zn ions at both A and B-sites [147,149,150]. The Raman study of NZ_xFO ceramics also confirmed the same. These findings indicate that $NZ_{0.3}FO$ should be used as magnetostrictive phase for the synthesis of *ME* composites.

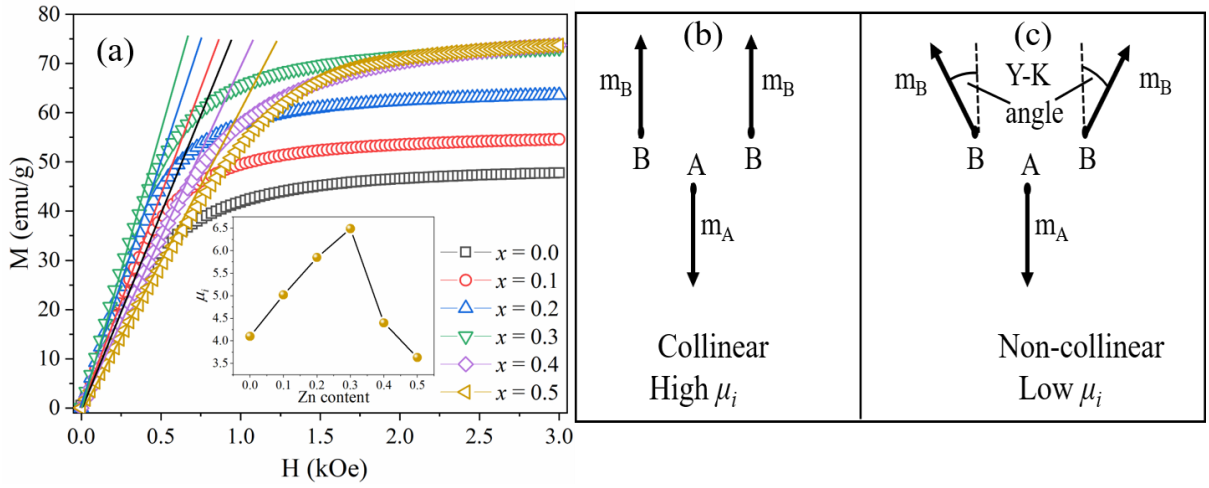

Figure 4.27. (a) Virgin *M-H* curves of NZ_xFO ceramics, where inset represents the variation of μ_i with Zn inclusion. Pictorial representation of (b) collinear and (c) non collinear magnetic ordering on permeability.

Chapter 5

Results and discussion: Magnetoelectric 0-3 composites

Overview

In this chapter, the phase, structural, electrical, magnetic and *ME* properties of 0-3 composites has been investigated. The chapter is divided into four sections. In the first section, the *ME* coupling in (1-*x*)BNT-*x*NFO composites are examined. Second section is focused on the *ME* coupling of (1-*x*)BNKMT-*x*NFO composite. These two sections demonstrate the effect of PE phase on *ME* coupling. In third section, the effect of magnetostrictive phase on the *ME* coupling has been studied by varying Zn substitution in NFO coupled with BNKMT in a fixed weight proportion, i.e., explore the *ME* coupling in 0.8BNKMT-0.2NZ$_x$FO composite. The last section emphasizes on the *ME* coupling based on the suitable PE (BNKMT) and magnetostrictive (NZ$_{0.3}$FO) in variation of relative weight fraction.

5.1 (1-*x*)BNT-*x*NFO composite

The *ME* particulate composite comprising BNT and NFO in varying weight fraction have been successfully synthesized at 1050 °C for 1h, i.e., (1-*x*)BNT-*x*NFO (x = 0.05 - 0.30; Δx = 0.05). Further, their structural, magnetic, electrical and *ME* properties have been systematically examined.

5.1.1 Phase analysis

The XRD pattern of pure BNT, NFO and composites (1-*x*)BNT-*x*NFO specimens is shown in **Figure 5.1**. The BNT crystallizes in pure rhombohedral crystal structure with *R3c* space group (JCPDS card: 036-0340), while NFO shows spinel structure with *Fd3m* space group (JCPDS card: 10-0325). The XRD pattern shows the existence of individual phases without any traces of impurity. It can be seen that the intensity of NFO peaks increase with its concentration in the composite.

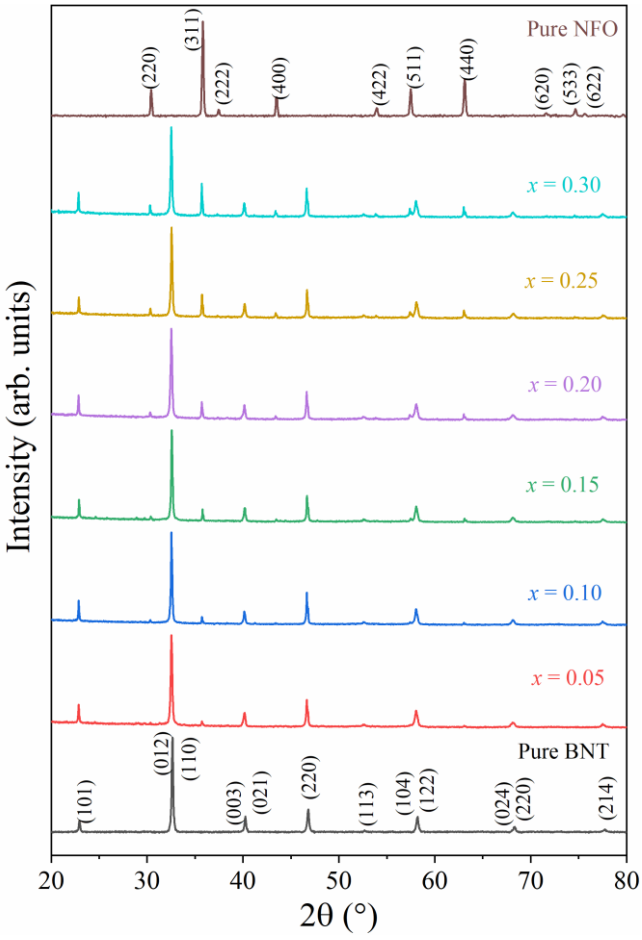

Figure 5.1. XRD pattern of pure BNT, NFO and composites of (1-*x*)BNT-*x*NFO specimens.

5.1.2 Raman study

Figure 5.2 depicts the Raman spectra of BNT, NFO and (1-*x*)BNT-*x*NFO composites specimens ranging from 100-800 cm^{-1}. As suggested by group theory all 3 Raman active modes (X, Y & Z) has been observed for BNT and in close agreement with previous studies [151,152]. The X, Y and Z bands demonstrates vibrations of Bi/Na-O, Ti-O, and Ti-O_6 octahedra respectively. Further, NFO exhibits three Raman bands denoted by P, Q and R. The P and Q are related to symmetric stretching and anti-symmetric bending of metal-oxygen bonds at octahedral site respectively, whereas R corresponds to stretching at tetrahedral site [145]. In composites, the bands of both phases are observed. However, low intensity of NFO peaks ascribed to its low volume fraction. It is to be noted that similar to XRD, no change in peak position is observed, which denied the presence of micro-strain towards bond compression/stretching along interphase boundaries.

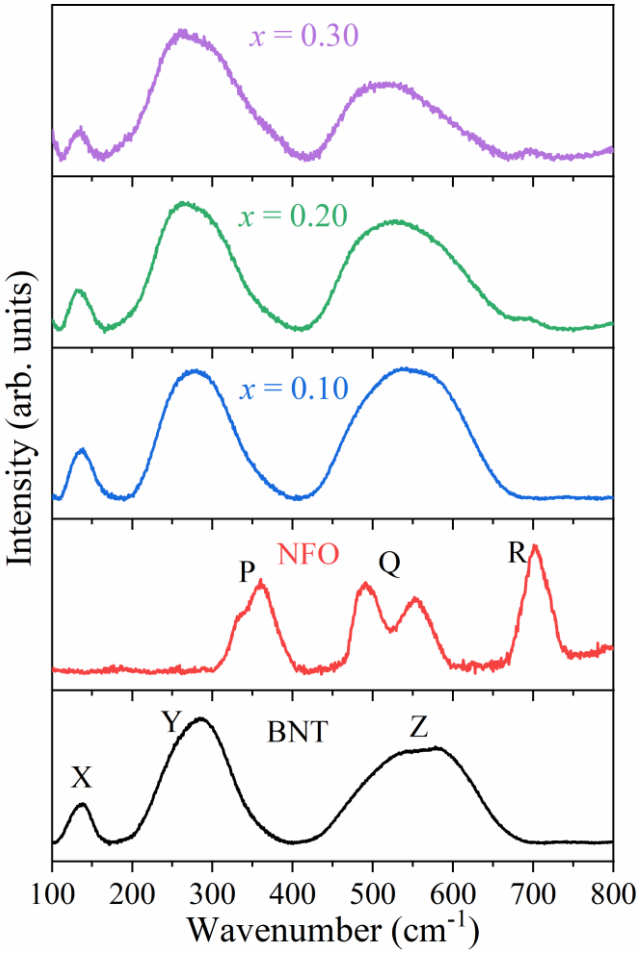

Figure 5.2. Raman spectra of pure BNT, pure NFO and (1-*x*)BNT-*x*NFO composite specimens.

5.1.3 Microstructural analysis

Figure 5.3(a-d) represents the SEM micrographs of pure BNT, NFO and composites 0.9BNT-0.1NFO and 0.7BNT-0.30NFO specimens. Within the used sintering conditions, the BNT grains are found relatively larger than NFO. A well distinguishable larger BNT grains with small NFO grains has been observed in the composite specimens as depicted in **Figure 5.3**(c)&(d).

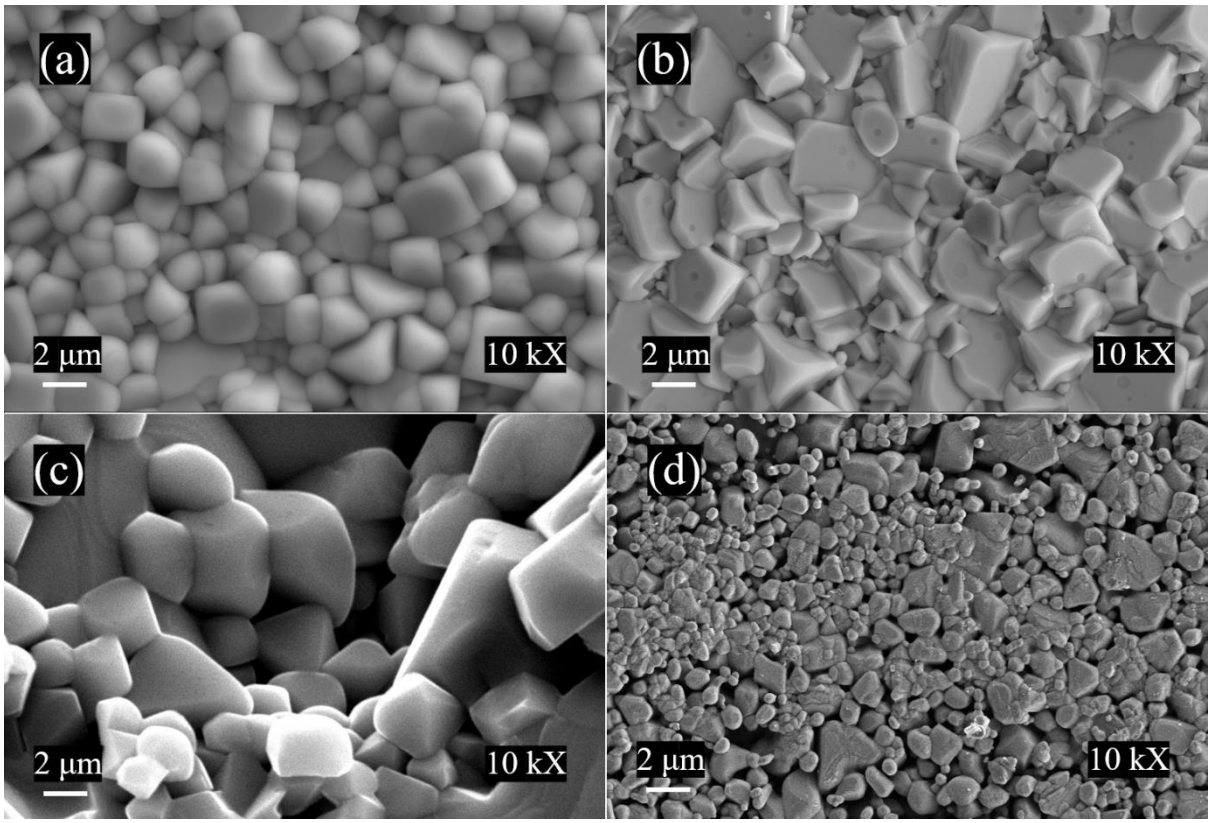

Figure 5.3. SEM micrographs of (1-*x*)BNT-*x*NFO sintered ceramics, where (a) $x = 0$, (b) $x = 0.10$, (c) $x = 0.30$, (d) $x = 1$.

Further, the representative backscattered electron image along with elemental mapping of 0.80BNT-0.20NFO sintered composite has been displayed in **Figure 5.4**. A dense microstructure with well distinguished sharp boundaries of BNT (bright) and NFO (dark) are clearly visible in the composite samples (**Figure 5.4**(a)). The BNT shows larger fraction of coarse grains due to its higher phase fraction, whereas grain growth of NFO may be hindered by the BNT phase. The NFO phase is found to be agglomerated as a consequence of mechanical mixing. The elemental mapping (**Figure 5.4**(b)) along with individual elements present confirms BNT and NFO grains as bright and dark contrast respectively in the samples. Mapping

of Na element is beyond the detection limit of the equipment. In composites, the distribution of FE and FM phases affects the electrical and magnetic properties. This is due to the connectivity of large ferroelectric and small ferrite grains in a composite specimen [153].

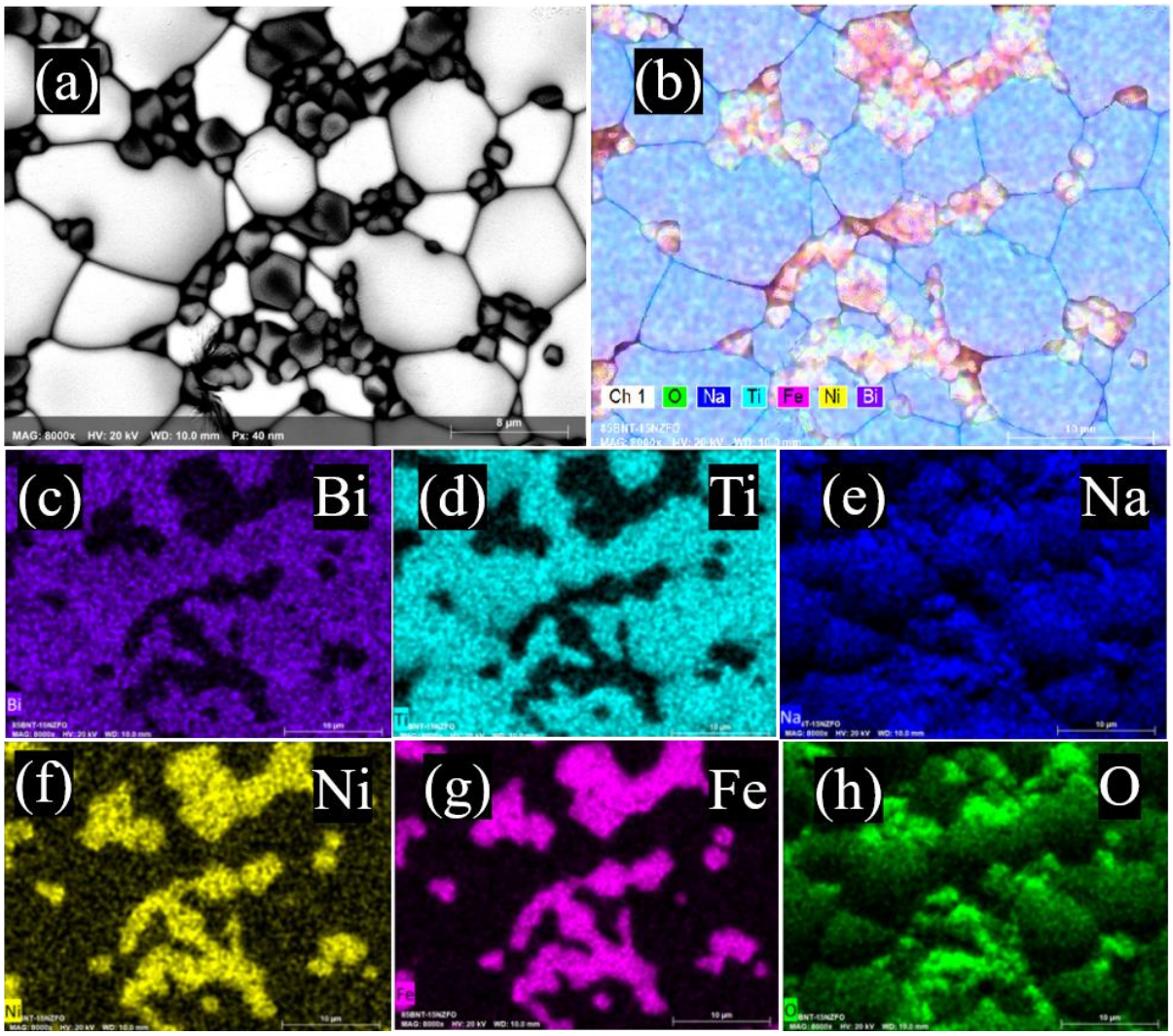

Figure 5.4. Microstructure (a) backscattered image, (b) elemental color mapping of 0.80BNT-0.20NFO composite specimen. (c)-(h) represents the elemental mapping on the same surface for individual element.

5.1.4 Dielectric study

The *RT* dielectric measurements of the pristine BNT, NFO and BNT-NFO composites have been measured in the *f* range from 10^2 Hz to 10^6 Hz and represented in **Figure 5.5**. In the lower frequency range (10^2 – 10^4 Hz), the ε_r decreases and saturate afterwards. According to Maxwell-Wagner polarization and Koop's two layer model, the dielectric behavior is comprised of distinct grains and grain boundaries at low *f*, while at higher *f* only grains

contribution is dominant [154]. It is observed that, as the ferrite concentrations increases, the ε_r decreases and tan δ increases, which pointed to the induction of low resistive phase.

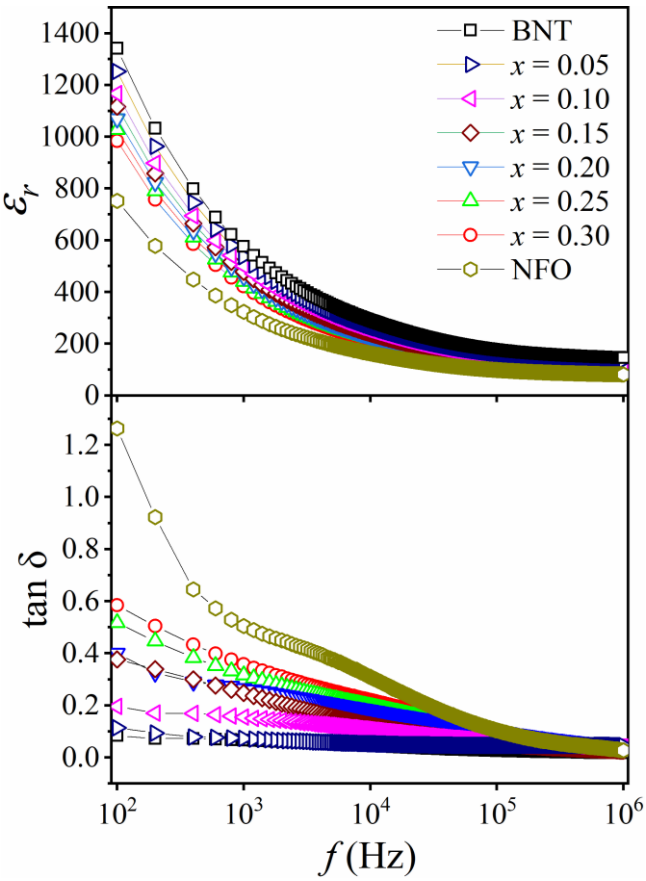

Figure 5.5. Variation in ε_r and tanδ for BNT, NFO and (1-x)BNT-xNFO composite specimens.

5.1.5 Leakage current measurement

In order to check the relative conductivity between the both PE and magnetostrictive phases, the *J-E* plot for BNT, NFO and their composites are recorded and represented in **Figure 5.6**. The graph illustrates the ohmic activity of *J* with *E* upto 1 kV/cm. This is due to the large grains and less dispersion of charge carriers. Above 1 kV/cm, the gradual increase in *J* indicates the contribution of grain boundaries, and Poole-Frenkel emission [136,137]. The *J* increases with NFO content that suggest its relatively low resistivity than BNT. Its induction may hinder the *P* of the composites, therefore, an optimized weight fraction in 0-3 composite is crucial in order to achieve good *ME* coupling.

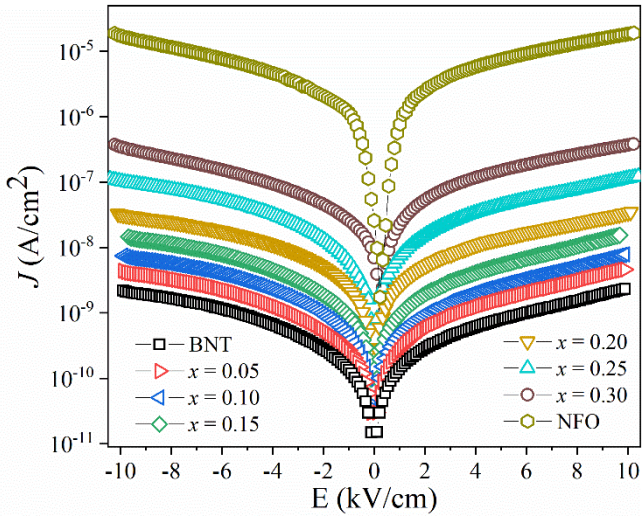

Figure 5.6. *J-E* plot for the BNT, NFO and (1-*x*)BNT-*x*NFO composite ceramics.

5.1.6 Ferroelectric study

The FE behavior of (1-*x*)BNT-*x*NFO specimens is confirmed by their *RT P-E* loops at 10 Hz are shown in **Figure 5.7**(a). A well saturated hysteresis has been observed for $x = 0.00$ and $x = 0.05$. Further, the increase in low resistive NFO phase enhances the conduction losses that make the composite to sustain relatively low *E*, result in the observation of unsaturated loops. The *P-E* loops for $x > 0.20$ exhibits lossy FE hysteresis behavior, which is an indication of the observation of weak *ME* coupling for such particular composition. Further, the obvious decline in P_r has been observed with the non-ferroelectric NFO content as shown in **Figure 5.7**(b). **Figure 5.7**(c) depicts their *S-E* curves, where *S* is found to decreased with NFO content in composite. Further, an obvious declined trend in d_{33} is observed with the induction of low resistive NFO content (**Figure 5.7**(d)), which creates path for the charge carriers to leak and makes electrical poling difficult.

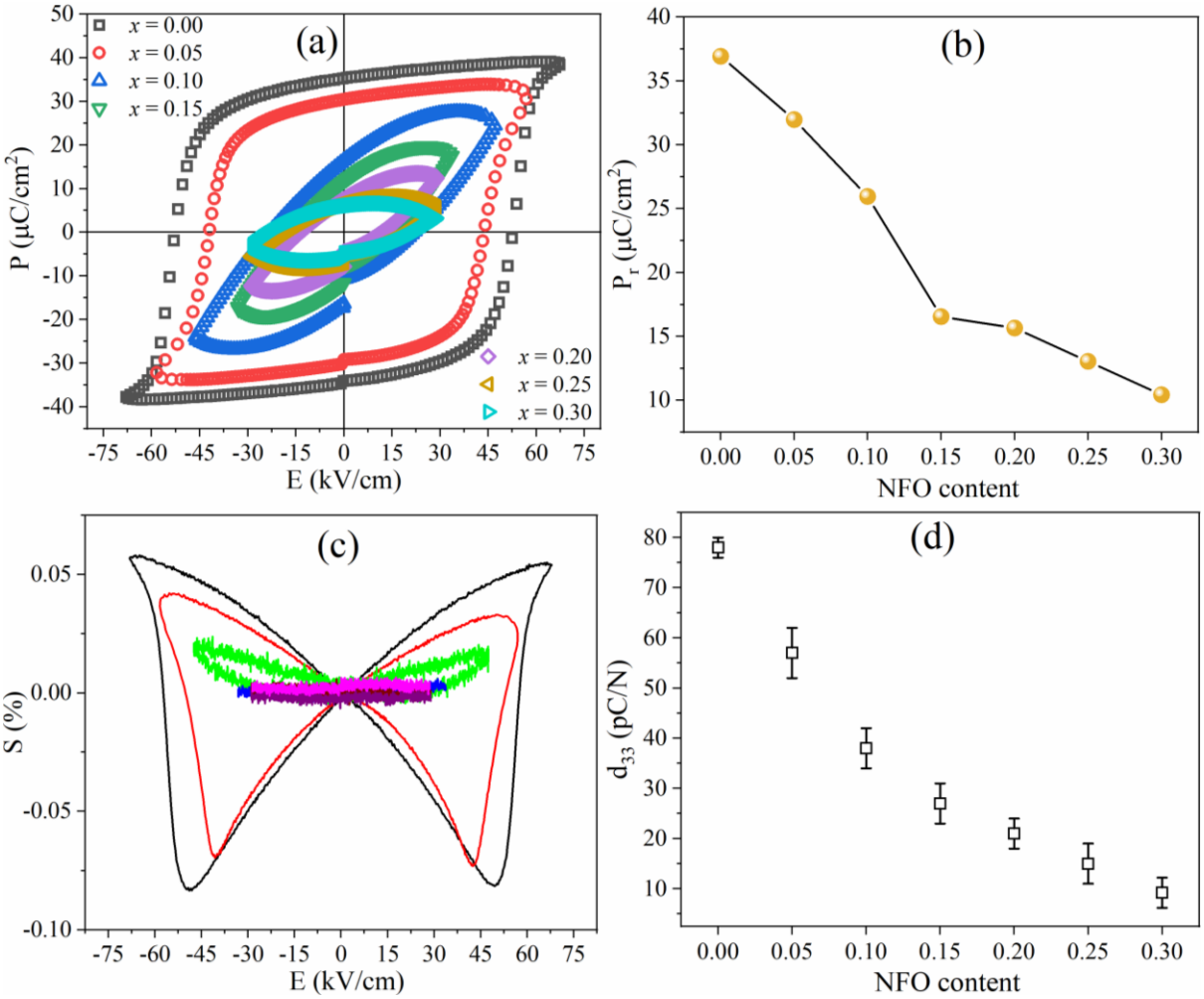

Figure 5.7. (a) *P-E* loops and (c) *S-E* curves measured with respect to NFO concentration in BNT. (b) and (d) represent change in P_r and d_{33} of BNT with NFO concentration.

5.1.7 Magnetic behavior analysis

The *RT M-H* loops of (1-*x*)BNT-*x*NFO composites in reversible dc *H* of 10 kOe is depicted in **Figure 5.8**. All the composites exhibit soft FM behavior due to the presence of magnetic NFO phase. Therefore, the M_s of the composites increase with the NFO content. The NFO exhibit the M_s of 46.53 emu/g as displayed in the inset of **Figure 5.8**.

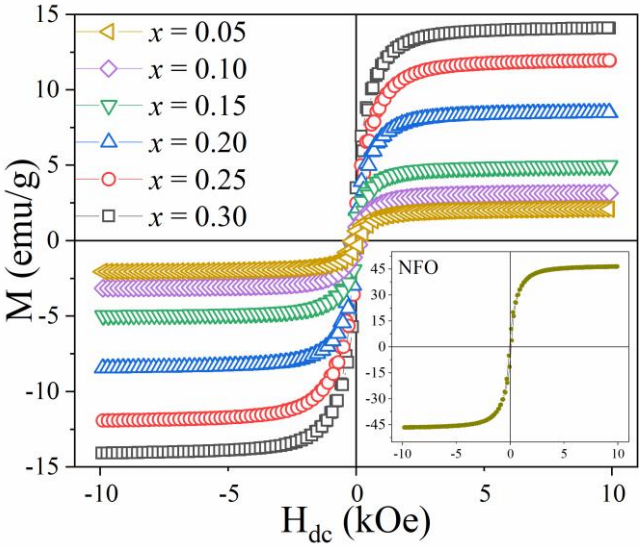

Figure 5.8. *RT* magnetic hysteresis behavior of (1-*x*)BNT-*x*NFO composites, where inset represents the *M-H* curve of pure NFO ceramics.

5.1.8 ME measurements

The *ME* coupling is a product tensor of both FE and FM property. As composite has exhibited both FE and FM characteristics, a large *ME* response in such specimens is expected. The α_{ME} for all composites as a function of H_{dc} at 3 Oe H_{ac} and 10 Hz are represented in **Figure 5.9**.

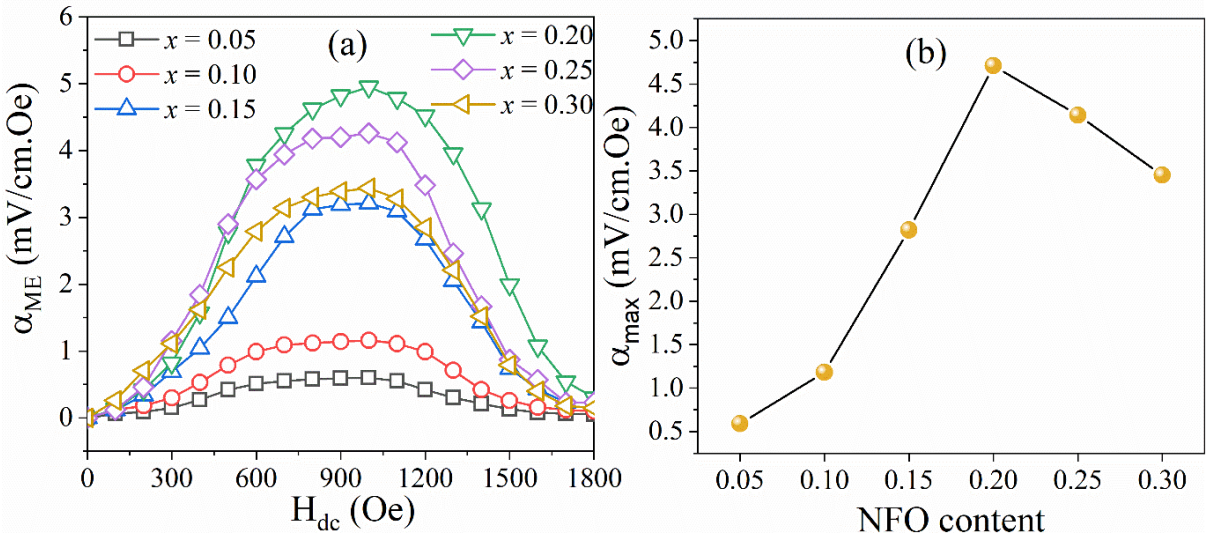

Figure 5.9. Variation in α_{ME} with (a) H_{dc} at 10 Hz and 3 Oe H_{ac} . (b) Variation in the α_{max} with NFO content at 1000 Oe for BNT-NFO composites.

The α_{ME} increases with H_{dc} till 1000 Oe and decreases afterward suggests the maximum strain mediated coupling occurred at 1000 Oe. As NFO content increases, α_{ME} also increases upto *x*

= 0.20 content and decreases thereafter (**Figure 5.9**(b)). The maximum obtained value of α_E (or α_{ME}) is 4.71 mV/cm.Oe for 0.80BNT-0.20NFO composite. For $x < 0.20$, the α_{ME} is low due to the small fraction of magnetostrictive phase. For $x > 0.20$, the excess amount of NFO content hinders the ferroelectric dipole alignments (already suggested by the FE measurements) that cause the lower value of α_{ME}.

5.2 (1-*x*)BNKMT-*x*NFO composite

The *ME* particulate composite comprising BNKMT and NFO in varying weight fraction have been sintered at 1050 °C for 1 h, i.e., (1-*x*)BNKMT-*x*NFO ($x = 0.05$ - 0.30; $\Delta x = 0.05$). Further, their structural, magnetic, electrical and *ME* properties have been systematically examined.

5.2.1 Phase analysis

The XRD pattern of BNKMT, NFO and composites (1-*x*)BNT-*x*NFO specimens is shown in **Figure 5.10**.

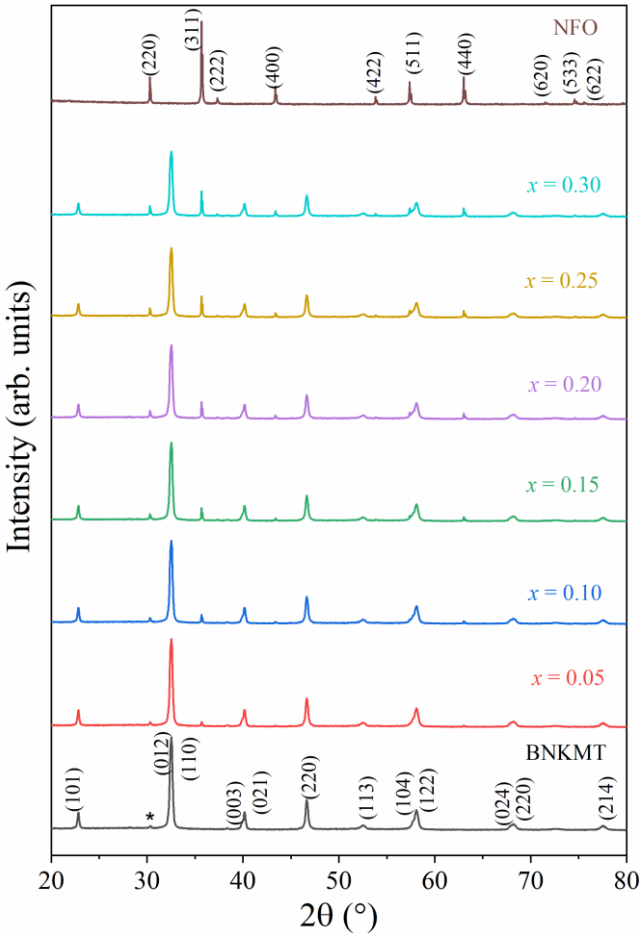

Figure 5.10. XRD pattern of sintered BNKMT, NFO and composites (1-*x*)BNKMT-*x*NFO specimens.

The diffraction peaks of BNKMT are matched with the JCPDS card number 36-0340, whereas NFO with JCPDS card: 10-0325 that reveals the formation of perovskite and inverse spinel structure, respectively. There is an observation of unwanted diffraction peak in BNKMT pattern that reveals the formation of secondary phase, i.e., orthorhombic $K_4Ti_3O_8$ (JCPDS: 041-0167, denoted by * in XRD pattern), which forms due to the Bi and Na volatility. Further, it can be noticed that the intensity of NFO peaks increase with its concentration in the composite.

5.2.2 Raman study

The Raman spectra of BNKMT, NZFO and 0.80BNKMT-0.20NZFO ceramics ranging from 100-800 cm^{-1} is shown in **Figure 5.11**.

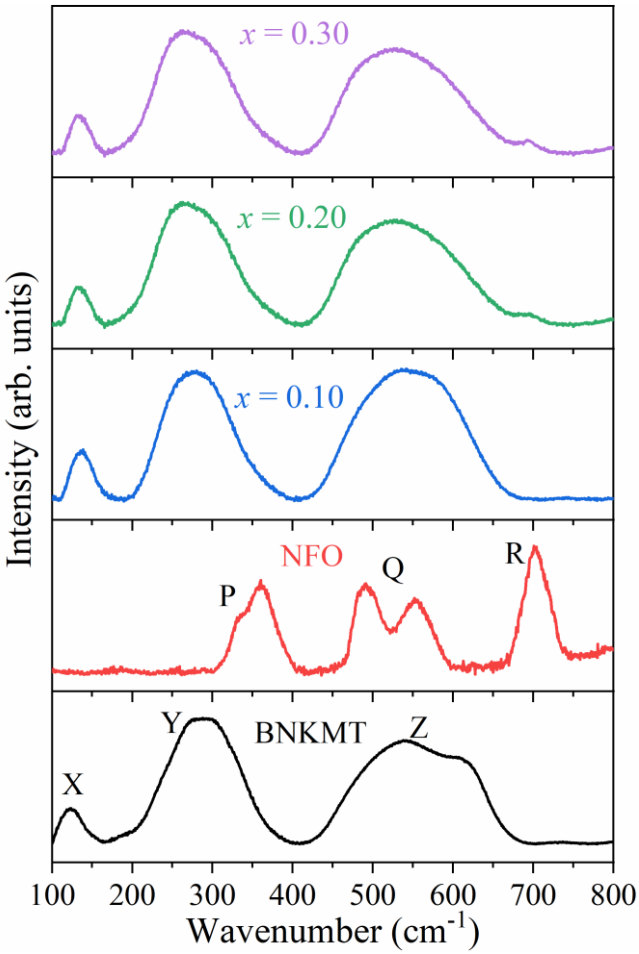

Figure 5.11. Raman spectra of BNKMT, NFO and (1-*x*)BNKMT-*x*NFO composite specimens.

For pure BNKMT, three Raman bands has been observed similar to pristine BNT and designated as X, Y and Z. The X, Y and Z band reflects the A-O, B-O, and B-O_6 octahedra vibrations respectively for ABO_3-perovskite structure of BNKMT. On the other hand, NFO exhibits three Raman bands denoted by P, Q and R. The P and Q are related to symmetric

stretching and anti-symmetric bending of metal-oxygen bonds at octahedral site respectively, whereas R corresponds to stretching at tetrahedral site [145]. In composites, the bands of NFO are obscured in the vicinity of BNKMT bands. Similar to XRD, there is no change in peak position, which negates the presence of micro-strain towards bond compression/stretching along interphase boundaries.

5.2.3 Microstructural analysis

The SEM micrographs of pure BNKMT, NFO and composites 0.9BNKMT-0.1NFO and 0.7BNKMT-0.30NFO specimens are shown in **Figure 5.12**(a-d). The BNKMT exhibits nearly cubic grains along with the abnormal rod like structure of the secondary phase (**Figure 5.12**(a)). The NFO grains are relatively smaller (**Figure 5.12**(d)) than BNKMT. A well distinguishable larger BNKMT grains with small NFO grains has been observed in the composite specimens as depicted in **Figure 5.12**(b) & (c).

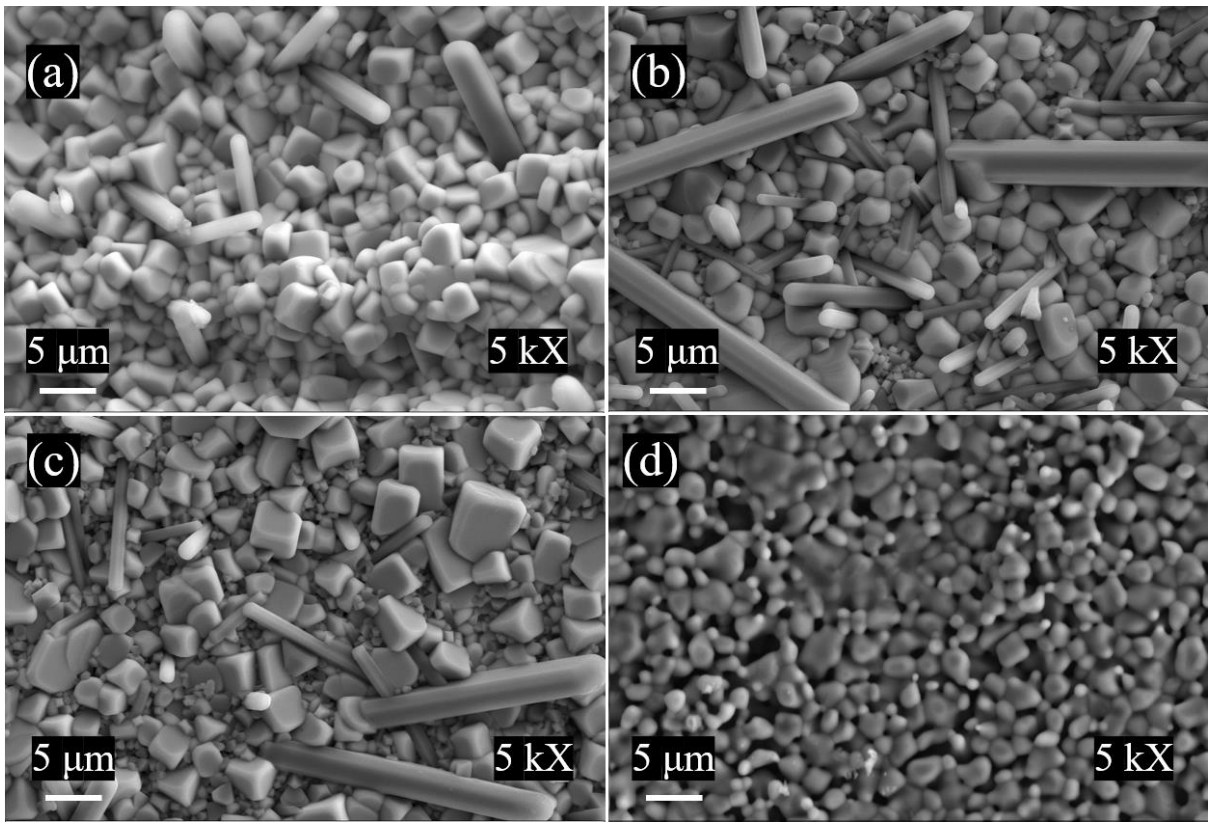

Figure 5.12. SEM micrographs of (1-*x*)BNKMT-*x*NFO sintered ceramics, where (a) $x = 0$, (b) $x = 0.10$, (c) $x = 0.30$, (d) $x = 1$.

A representative backscattered electron micrograph of sintered 0.80BNKMT-0.20NFO composite suggest the dark colored abnormal rod like and smaller grain corresponds to one

phase whereas bright normal grains reflect another phase as displayed in **Figure** 5.13(a). The elemental mapping of 0.8BNKMT-0.2NFO composite (**Figure** 5.13(b)) reveals that the smaller and normal size grains correspond to magnetic NFO and piezoelectric BNKMT phase respectively. Interestingly, an abnormal rod like grains pointed towards secondary phase of BNKMT that arises due to Bi and Na deficiency (already suggested by its XRD pattern). The elemental mapping of Na and Mg is not displayed as it beyond the detection limit of an instrument. The growth of secondary phase directly influences the electrical and *ME* properties of the ceramics.

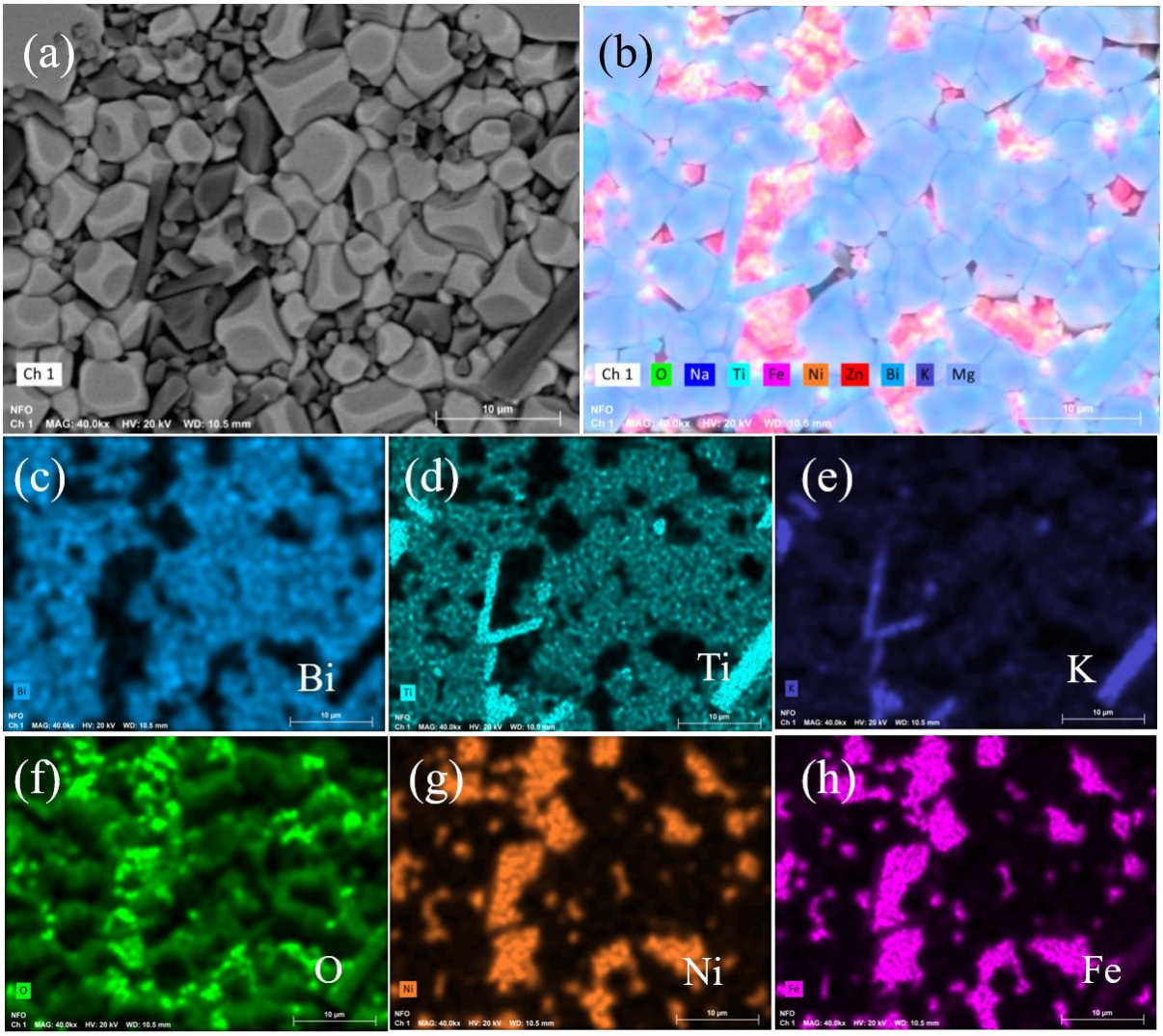

Figure 5.13. Representative (a) backscattered SEM micrograph and (b) elemental mapping of sintered 0.80BNKMT-0.20NFO composite. (c)-(h) represents the elemental mapping on the same surface for individual element.

5.2.4 Dielectric study

Figure 5.14 shows the *RT* dielectric behavior of the BNKMT and BNKMT-NFO composites in the *f* range of 10^2 Hz to 10^6 Hz. The ε_r decreases abruptly in the lower *f* region (10^2 - 10^4 Hz) and gradually in the higher *f* region (10^4 - 10^6 Hz). According to Maxwell-Wagner polarization and Koop's two-layer model, the dielectric behavior at low *f* is composed of distinct grains and grain boundaries, but at higher *f*, only grains contribute towards polarization [154]. As the concentration of ferrite increases, ε_r decreases and tan δ increases that indicates the induction of a phase that have relatively low resistivity.

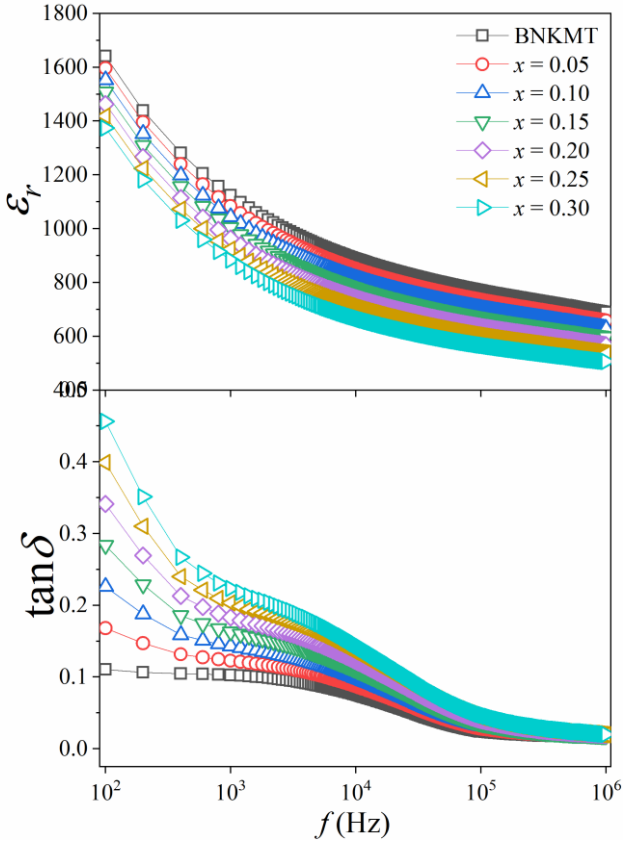

Figure 5.14. Variation in ε_r and tan δ for BNKMT and (1-*x*)BNKMT-*x*NFO composite specimens.

5.2.5 Leakage current measurement

In order to determine the relative conductivity between the PE and magnetostrictive phases, the *J-E* plot for BNKMT and BNKMT-NFO (illustrated in **Figure** 5.15) are examined and analyzed.

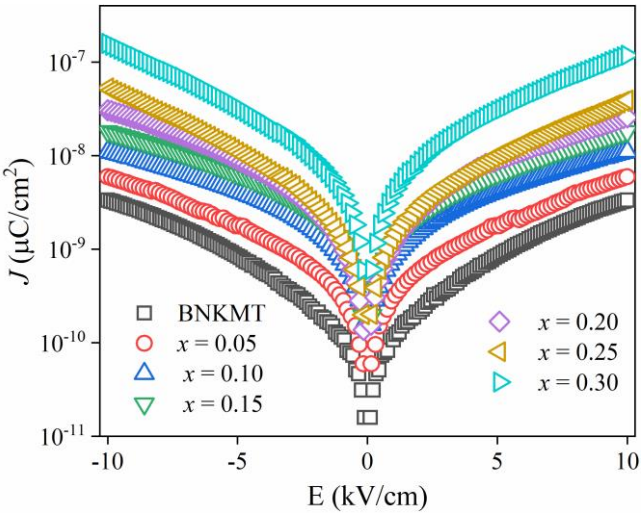

Figure 5.15. *J-E* curves for BNKMT and (1-*x*)BNKMT-*x*NFO composite specimens.

The *J* increases abruptly with *E* upto 1 kV/cm followed by gradual increase. In low *E* (< 1 kV/cm), the large grains contribute towards enhancing *J*, whereas above 1 kV/cm, the contribution of grain boundaries, and Poole-Frenkel emission restricts the *J* [136,137]. The *J* increases with NFO content that suggest its relatively low resistivity than BNKMT. Its induction could negatively impact the *P* of the composites. Thus, an optimized weight fraction in 0-3 composite is crucial for optimal *ME* properties.

5.2.6 Ferroelectric study

Further, *RT P-E* loops for BNKMT and (1-*x*)BNKMT-*x*NFO composites at 10 Hz are displayed in **Figure 5.16**(a). The FE loops are observed for all the specimens. The FE BNKMT phase exhibit good P_r (~ 9.98 μC/cm^2) and low E_c (~13.59 kV/cm). Further, an obvious decrease in P_s has been observed with NFO that is attributed to the relative decrease in FE phase. Moreover, the addition of low resistive NFO phase, enhances the conduction losses in the composites (increase of *P-E* loop area and slope of *P* at high *E* is negative). Therefore, the composites with higher NFO content are unable to sustain high *E*. Further, bipolar *S-E* loops of BNKMT and (1-*x*)BNKMT-*x*NFO composites at 10 Hz are represented in **Figure 5.16**(b). An obvious decrease in *S* has been observed with the induction of non-piezoelectric NFO phase as depicted in **Figure 5.16**(c). Similarly, an obvious decrease in d_{33} with NFO content has been observed (**Figure 5.16**(d)).

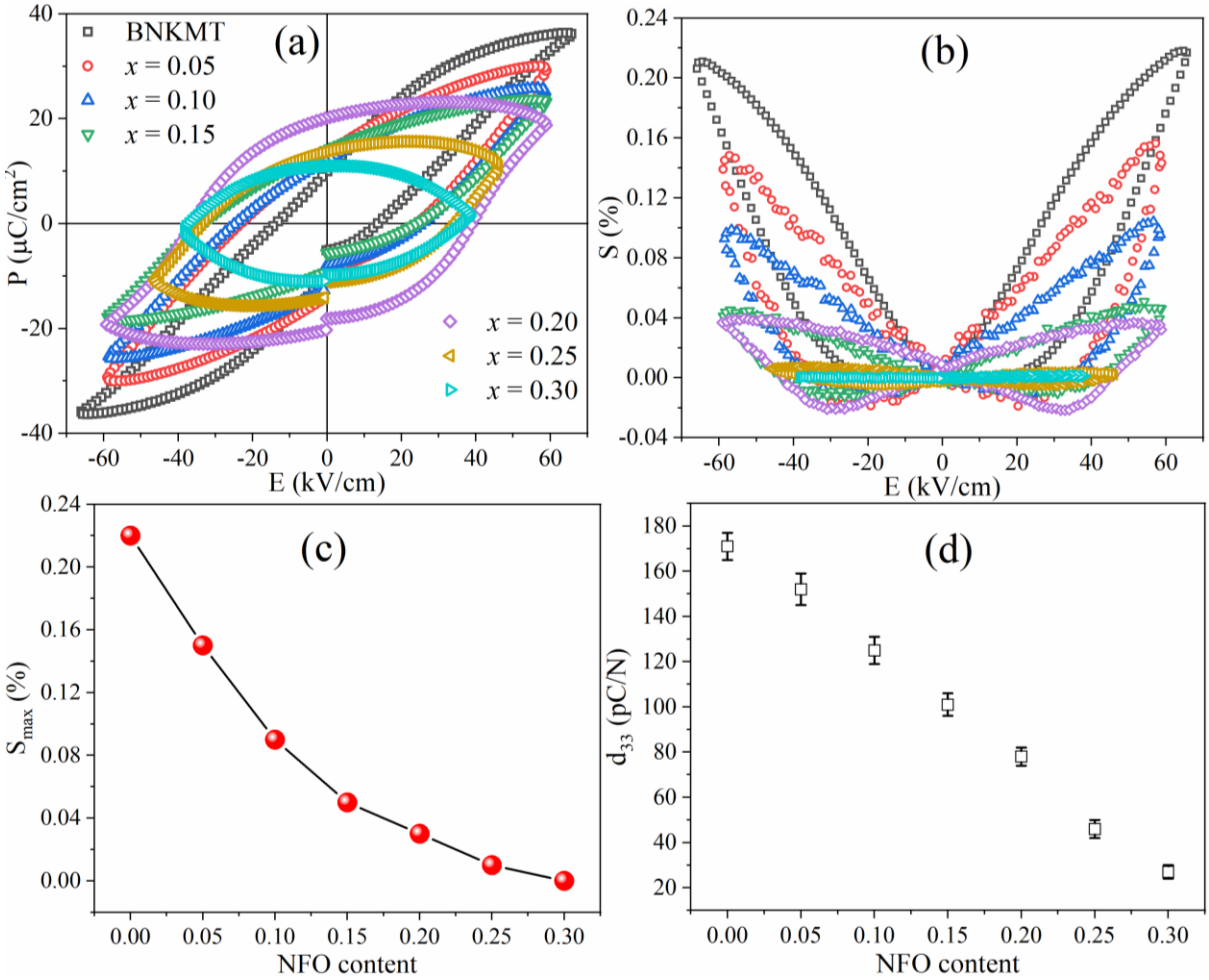

Figure 5.16. Variation in (a) *P-E* loops and (b) *S-E* curves of BNKMT and (1-*x*)BNKMT-*x*NFO specimens measured at 10 Hz. Influence of NFO substitution on (c) S_{max} and (d) d_{33} of the BNKMT-NFO specimens

5.2.7 Magnetic behavior analysis

The *RT M-H* hysteresis curves of (1-*x*)BNKMT-*x*NFO composites in ±10 kOe is shown in **Figure 5.17**. All the composites exhibit soft FM behavior due to the presence of magnetic NFO phase, where, the M_s of the composites increase due to the relative increase of magnetic content. The NFO exhibit the M_s of 46.53 emu/g as depicted in the inset of **Figure 5.17**.

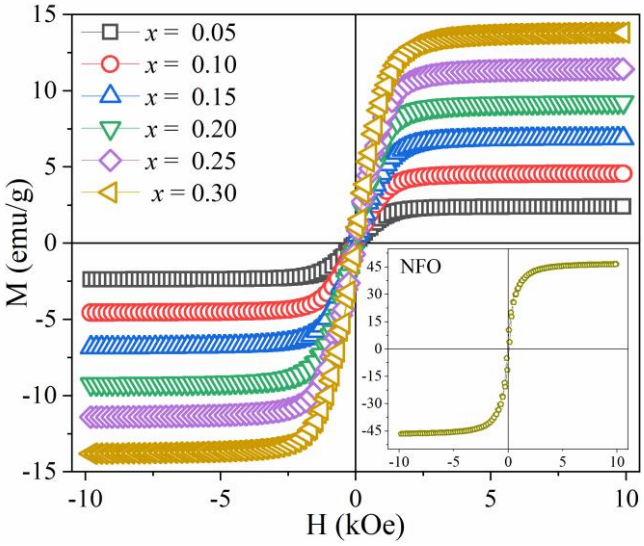

Figure 5.17. *RT* magnetic behavior of (1-*x*)BNKMT-*x*NFO composites, where inset represents the *M* behavior of pure NFO ceramics.

5.2.8 ME measurements

The *ME* coupling is a result of tensor product involving both the FE and FM properties. As composite has exhibited both characteristics, a large *ME* response in such specimens is anticipated. The α_{ME} for all composites as a function of H_{dc} with 3 Oe H_{ac} and 10 Hz has shown in **Figure 5.18**(a).

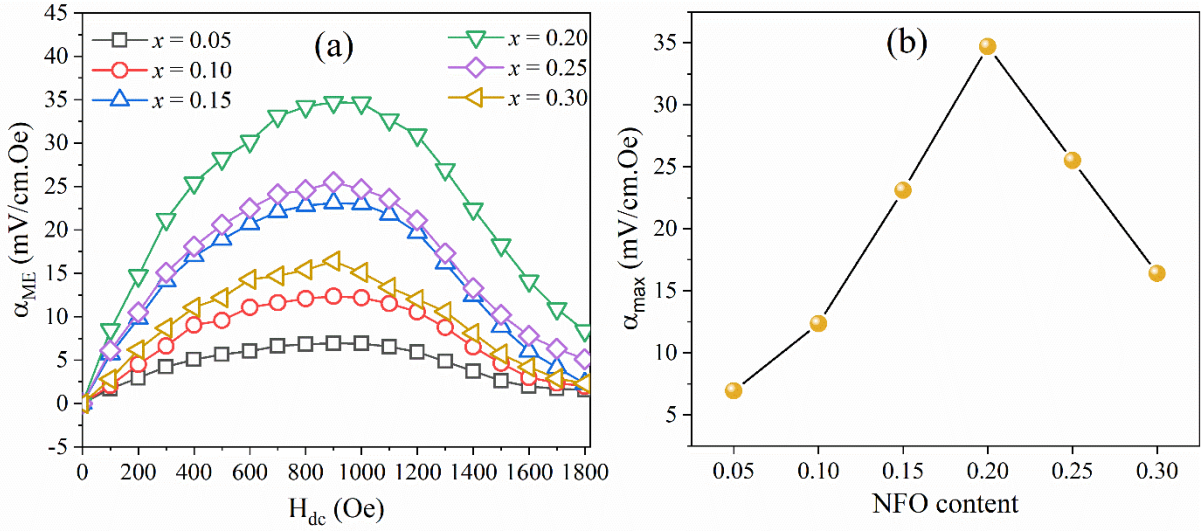

Figure 5.18. Change in α_{ME} with (a) H_{dc} at 3 Oe H_{ac} and 10 Hz frequency and (b) NFO content at 1000 Oe for (1-*x*)BNKMT-*x*NFO composites.

The α_{ME} increases with H_{dc} till 1000 Oe and decreases afterward that suggest the maximum strain mediated coupling occurred at 1000 Oe. As NFO content increases α_{ME} also increases upto $x = 0.20$ content and thereafter decreases (**Figure 5.18**(b)). The maximum obtained value of α_{ME} is 34.69 mV/cm.Oe for 0.80BNKMT-0.20NFO composite. For $x < 0.20$, the α_{ME} is low due to the small fraction of magnetostrictive phase. For $x > 0.20$, the excess amount of NFO content hinders the FE dipole alignments (already suggested by the FE measurements) that cause the lower value of α_{ME}. The observed value of α_{ME} in BNKMT-NFO is 7.4 times higher than the observed for BNT-NFO. This is due to the increase in the d_{33} values by the formation of solid solutions.

5.3 0.8BNKMT-0.2NZ$_x$FO composite

Amongst BNT-NFO and BNKMT-NFO, BNKMT-NFO depicts better *ME* coupling due to the higher d_{33} of BNKMT. Therefore, in this section, the effect of magnetostrictive phase (NZ$_x$FO) on *ME* coupling has been examined. The *ME* composite of consisting BNKMT as piezoelectric phase and NZ$_x$FO as magnetic phase has been prepared in a fixed weight ratio of 80:20 respectively (i.e., 0.8BNKMT-0.2NZ$_x$FO; $x = 0$, 0.1, 0.2, 0.3, 0.4 and 0.5) and sintered at 1050 °C for 1h. Further, their structural, magnetic and *ME* properties have been systematically examined.

5.3.1 Phase analysis

Figure 5.19 depicts the XRD pattern of 0.8BNKMT-0.2NZ$_x$FO composite specimens. The distinguishable diffraction peaks of both PE and magnetostrictive phases are matched with perovskite BNKMT (JCPDS: 36-0340) and cubic spinel NZ$_x$FO (JCPDS: 10-0325) ceramics respectively. The absence of any additional peak confirms the lack of chemical reaction at their interfaces.

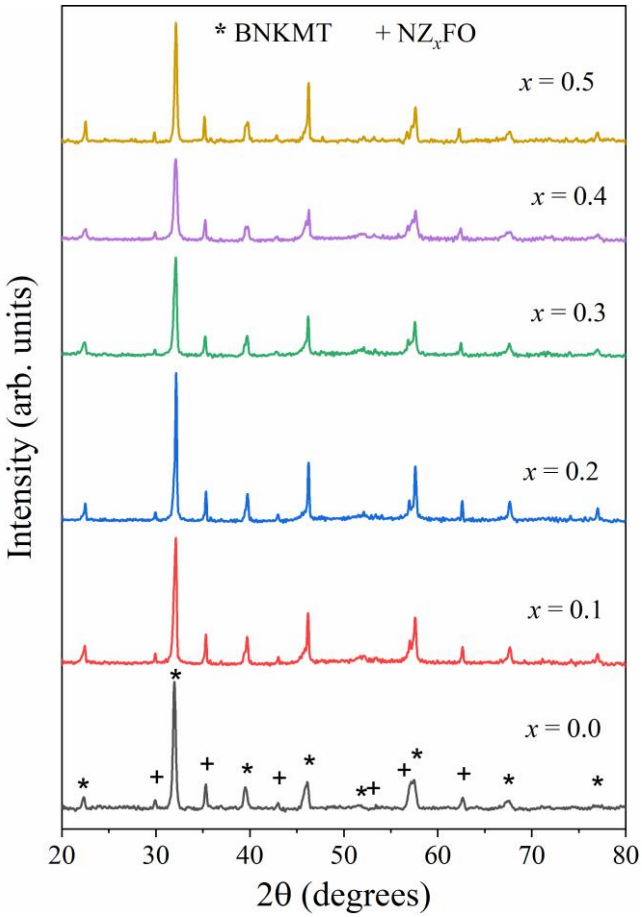

Figure 5.19. XRD pattern of sintered 0.8BNKMT-0.2NZ$_x$FO composites sintered at 1050 °C for 1h.

5.3.2 Microstructural analysis

Further, the microstructure of 0.8BNKMT-0.2NZ$_x$FO composites is depicted in **Figure 5.20**. For every composition, a dense microstructure has been observed, which is crucial in order to achieve good *ME* coupling. On the basis of their size and shape, the grains can be categorized into three types: smaller grains (0.5-1.5 μm), normal grains (1.5-7 μm), and unusual rod-like grains (> 7 μm). As already studied in the section 4.2.3, the normal and abnormal rod like grains attributes to the BNKMT and $K_4Ti_3O_8$ (induced during BNKMT phase formation within the used processing condition) phases respectively, whereas smaller grains reflect the magnetic phase.

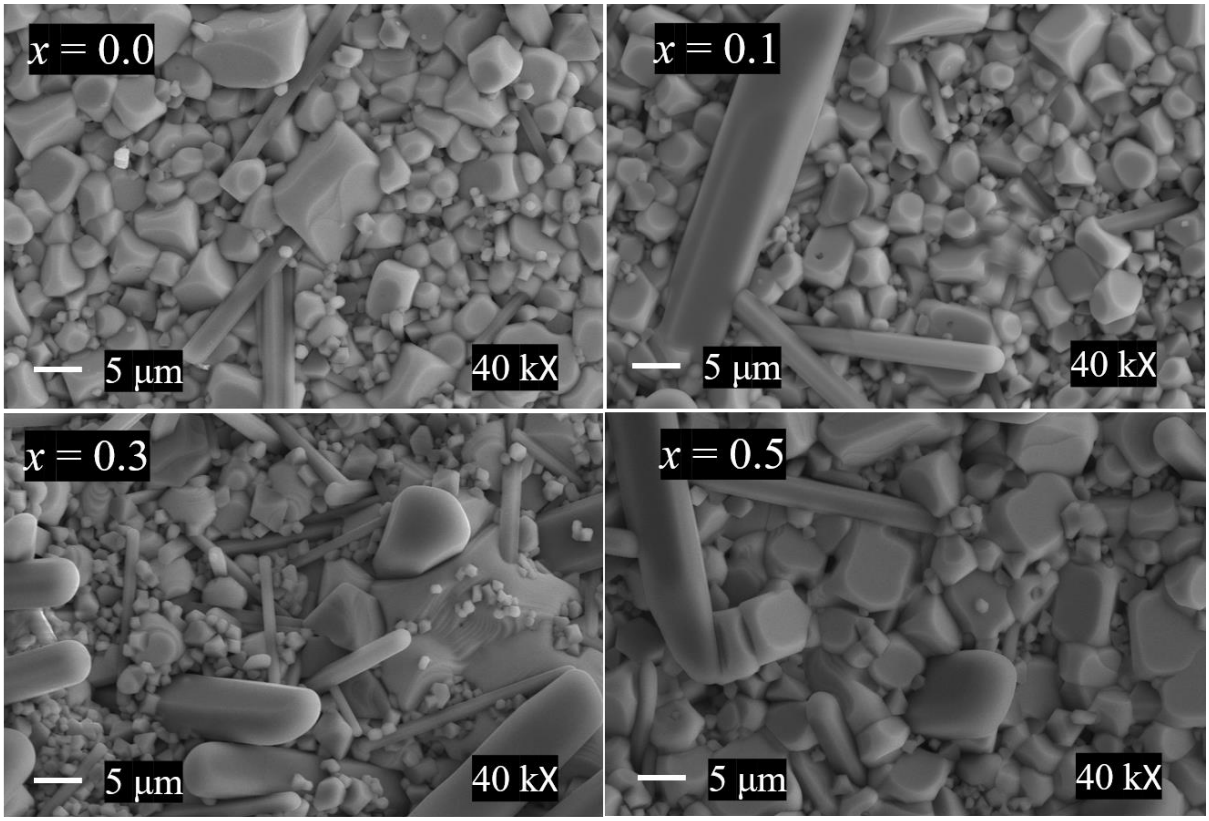

Figure 5.20. SEM micrographs of sintered 0.8BNKMT-0.2NZ$_x$FO composite specimens.

To confirm the same in this particulate composite series, a representative backscattered electron micrograph and elemental mapping of sintered 0.8BNKMT-0.2NZ$_{0.2}$FO composite has been recorded and shown in **Figure 5.21**. The backscattered electron micrograph suggests the dark color abnormal rod like grains and smaller grain reflects the one phase whereas bright normal grains reflect another phase as displayed in Figure 5.21(a). However, the elemental mapping of 0.8BNKMT-0.2NZ$_{0.2}$FO composite (**Figure 5.21**(b)) reveals that the smaller and normal size grains correspond to magnetic NFO and piezoelectric BNKMT phase respectively. Interestingly, an abnormal rod like grains pointed towards secondary phase of BNKMT that arises due to Bi and Na deficiency (already discussed in the phase analysis section 4.2.1 & 5.2.1). The elemental mapping of Na and Mg is not displayed as it beyond the detection limit of an instrument.

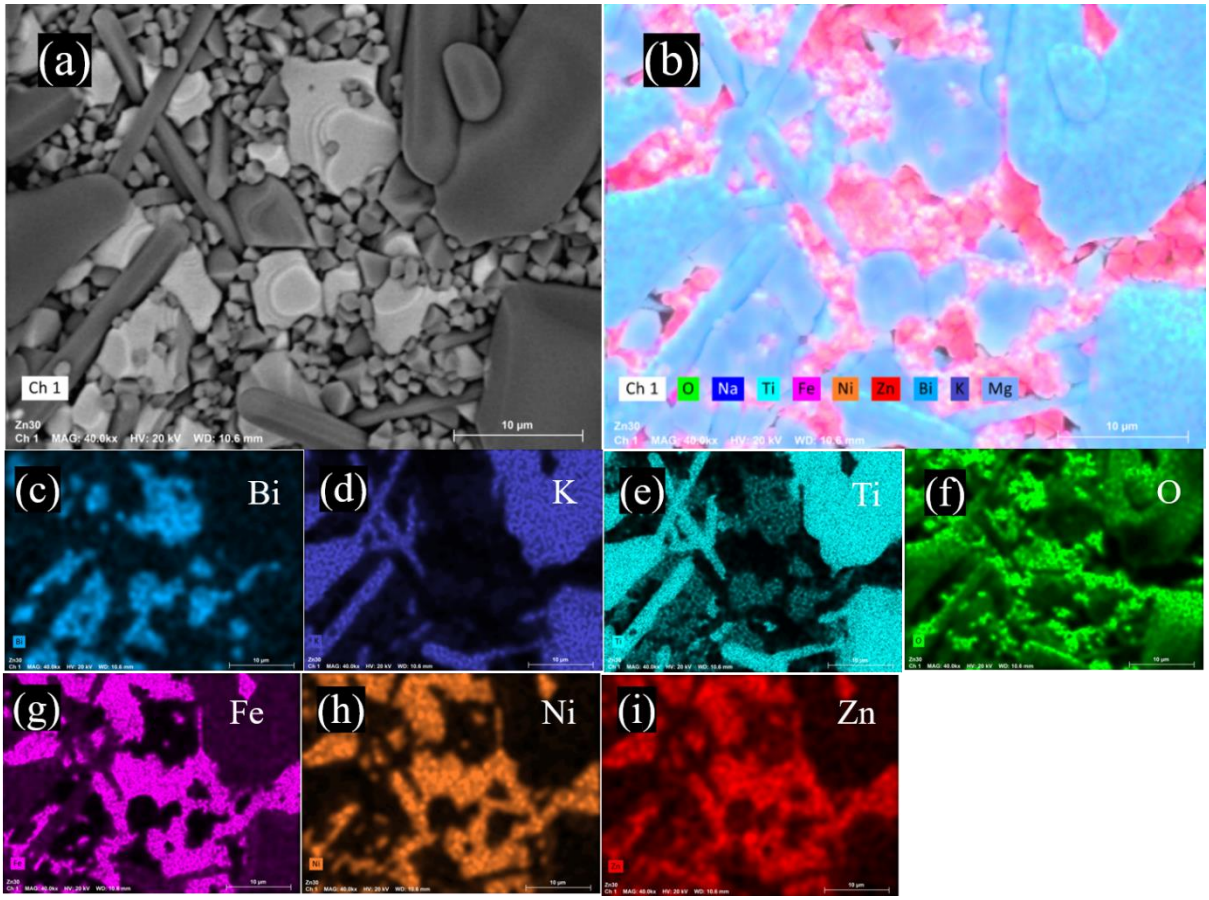

Figure 5.21. (a) Backscattered image and (b) elemental color mapping of 0.80BNKMT-0.20NZ$_{0.2}$FO composite. (c)- (i) Elemental mapping on the same surface for individual element.

5.3.3 Ferroelectric study

Further, *RT P-E* loops 0.8BNKMT-0.2NZ$_x$FO composites at 10 Hz are displayed in **Figure 5.22**(a). The FE loops have been observed for all the specimens. As the BNKMT is the FE phase and its composition is fixed in the composite. Therefore, no significant change in the P_r and P_s has been observed throughout the composite series. Further, their variation in *S-E* curves has been represented in the **Figure 5.22**(b). All samples exhibit butterfly loops. However, there has no significant change in the *S* has been observed (**Figure 5.22**(c)). Similar to the *P* and *S*, there has no remarkable change in the d_{33} is noticed (**Figure 5.22**(d)). All the composite specimens exhibit d_{33} ~ 80 pC/N.

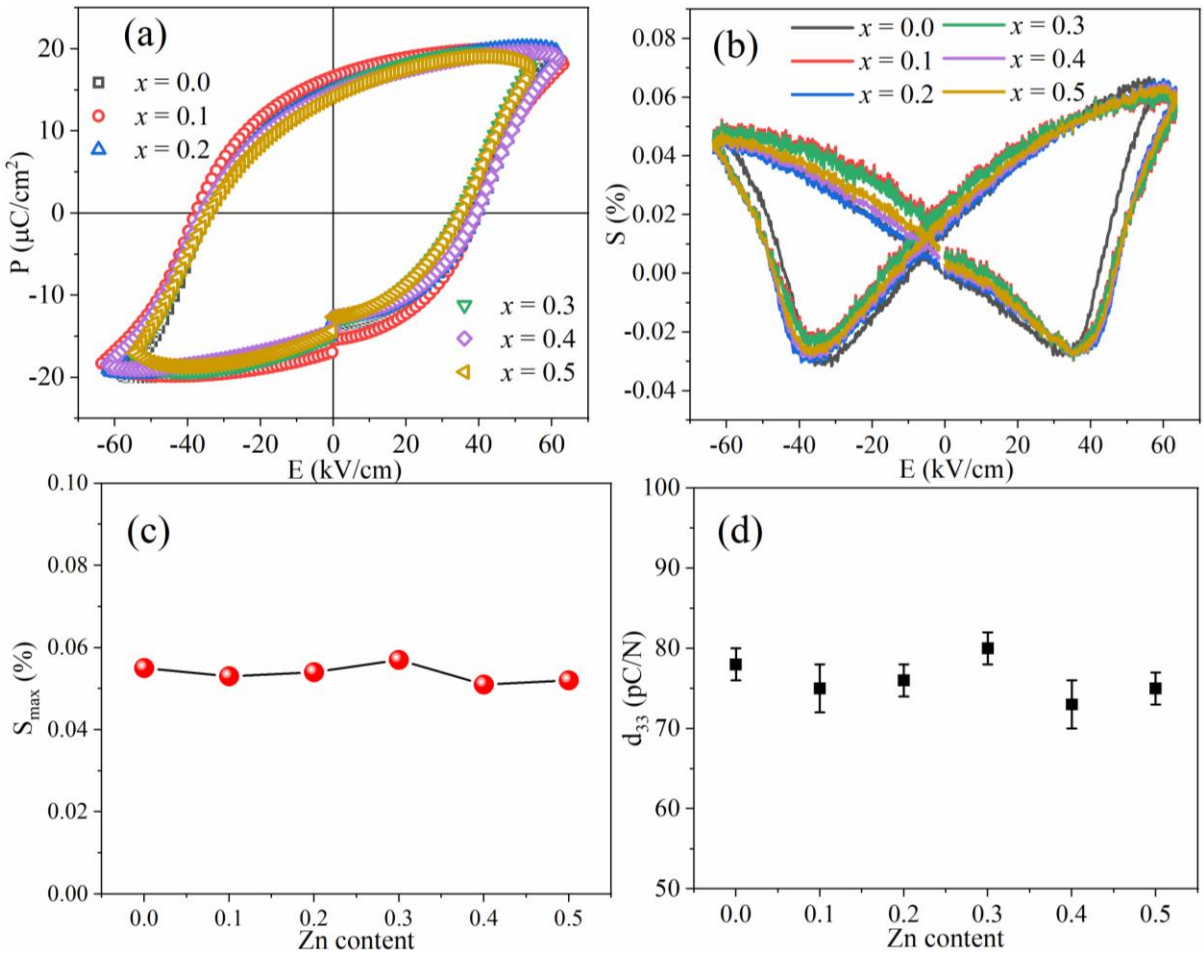

Figure 5.22. Variation in (a) *P-E* loops and (b) *S-E* curves in 0.8BNKMT-0.2NZ$_x$FO composites at 10 Hz. Influence of Zn substitution on (c) S_{max} and (d) d_{33} of the composites.

5.3.4 Magnetic behavior analysis

Further, the magnetic behavior of 0.8BNKMT-0.2NZ$_x$FO composites have been examined as shown in **Figure 5.23**. All the composites exhibit slim magnetic hysteresis behavior as illustrated in **Figure 5.23**(a). The inclusion of Zn enhances the M_s as displayed in **Figure 5.23**(b). Further, to analyze the qualitative PM coefficient, their dM^2/dH *vs* H plot has been investigated as shown in **Figure 5.23**(c). The dM^2/dH is found to increase with Zn substitution till x = 0.3 and decreases afterwards (**Figure 5.23**(d)). This is due to the variation in initial permeability of the NZ$_x$FO ceramics, which is already discussed in the magnetic behavior (section 4.4.4).

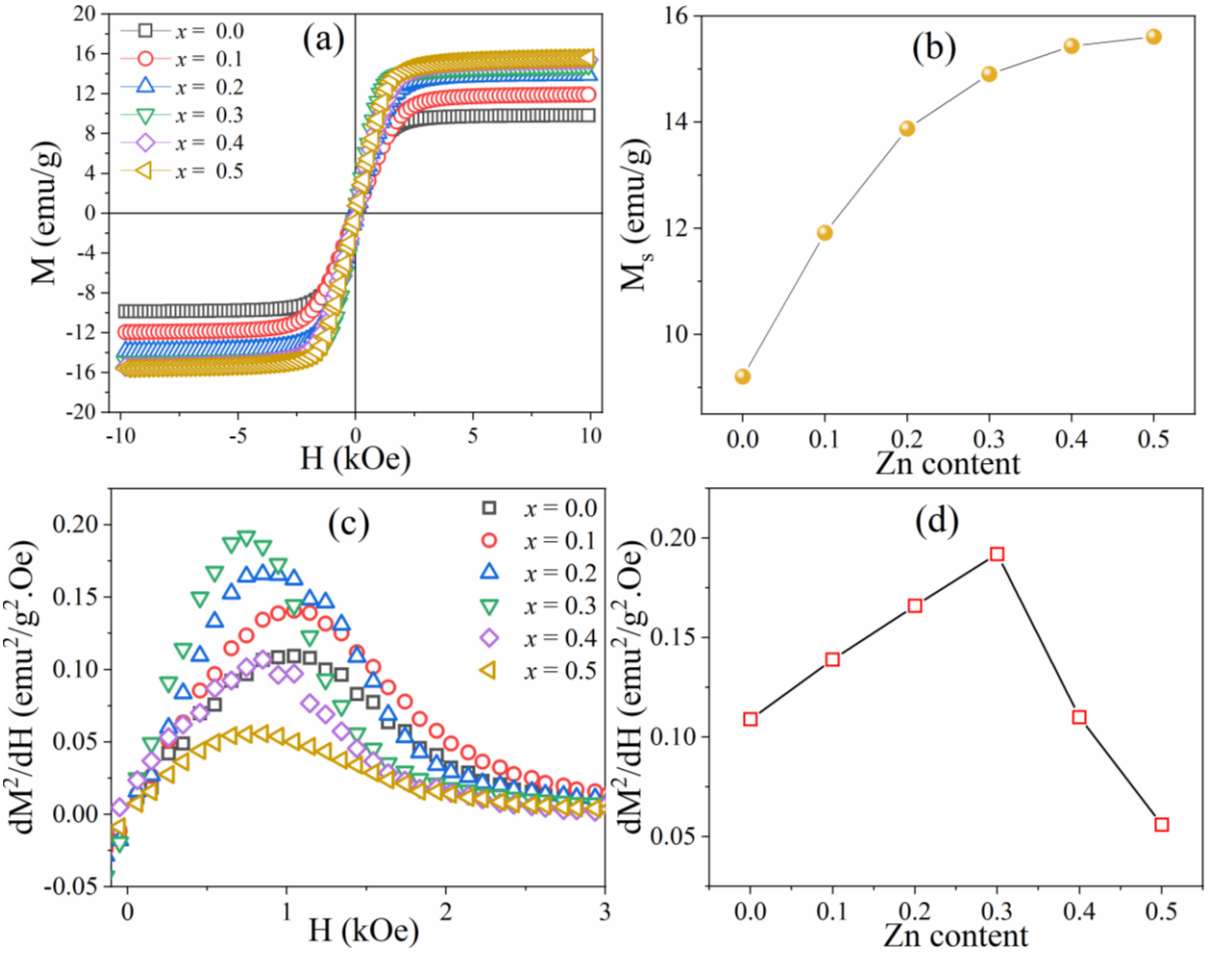

Figure 5.23. Variation in (a) *M*, (b) dM^2/dH with the variation in *H*. (c) M_s and (d) dM^2/dH versus Zn concentration for 0.8BNKMT-0.2NZ$_x$FO composites. Swap (b) and (c).

5.3.5 ME measurements

Further, the variation in α_{ME} with *H* for 0.8BNKMT-0.2NZ$_x$FO composites has been shown in **Figure 5.24**(a). The α_{ME} increases with *H* upto its peak value (α_{max}) and decreases afterwards. The Zn substitution enhances the α_{max} upto $x = 0.3$ followed by a subsequent decrease (**Figure 5.24**(b)), which indicates the modulation of *ME* coupling by an alteration of piezomagnetism. The highest obtained value (at ~ 800 Oe) of α_{ME} for 0.8BNKMT-0.2NZ$_{0.3}$FO composite is 58.12 mV/cm.Oe at 10 Hz, which has not been reported in the particulate composite so far at such low frequency operation (10 Hz). Moreover, the α_{ME} is 12.34 times higher than the BNT-NFO and 1.67 times higher than the BNKMT-NFO composites. This indicates that BNKMT-NZ$_{0.3}$FO composite could be viable candidate for the low frequency *ME* devices or energy harvesting applications.

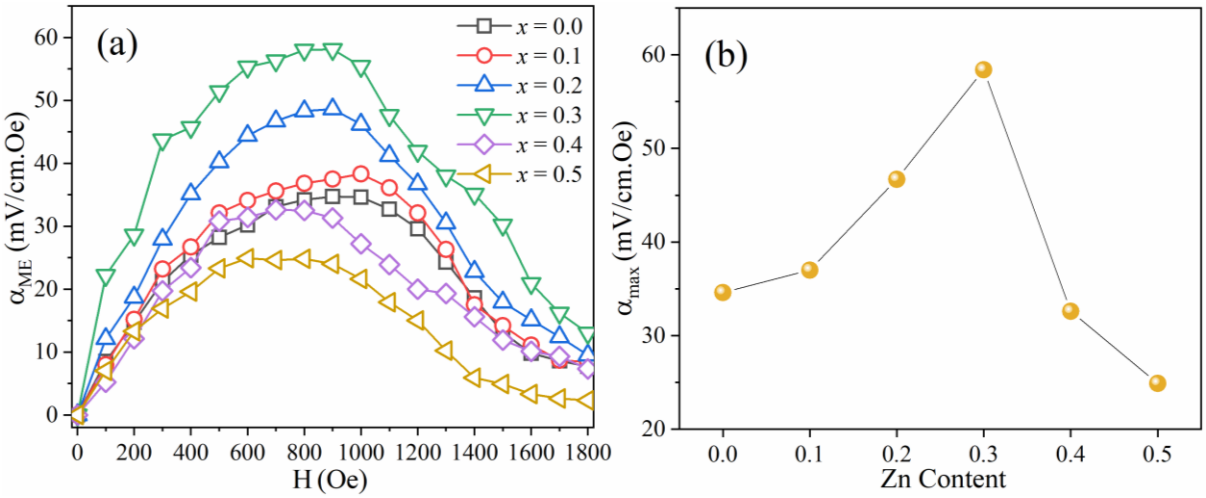

Figure 5.24. (a) Variation of α_{ME} with H at 10 Hz and 3 Oe H_{ac}. (b) α_{max} with Zn substitution in 0.8BNKMT-0.2NZ$_x$FO composites.

5.4 (1-*x*)BNKMT-*x*NZ$_{0.3}$FO composite

Based on the findings of the previous sections, it can be concluded that BNKMT is the promising piezoelectric phase, whereas NZ$_{0.3}$FO exhibits excellent q_s. Therefore, in this section, the *ME* coupling in their particulate composite has been examined by varying relative weight fraction. The *ME* particulate composite of (1-*x*)BNKMT-xNZ$_{0.3}$FO (x = 0.05 - 0.30; Δx = 0.05) has been prepared at 1050 °C for 1 h. Further, their structural, electrical, magnetic and *ME* properties have been systematically examined.

5.4.1 Phase analysis

Figure 5.25 shows the XRD pattern of sintered BNKMT, NZ$_{0.3}$FO and (1-*x*)BNKMT-xNZ$_{0.3}$FO composites. The diffraction peaks of BNKMT are matched with the JCPDS card number 36-0340, whereas NZ$_{0.3}$FO with JCPDS card: 10-0325 that reveals the formation of perovskite and inverse spinel structure, respectively. The observation of unwanted diffraction peak in BNKMT pattern reveals the formation of secondary phase (i.e., orthorhombic $K_4Ti_3O_8$ (JCPDS: 041-0167, denoted by * in XRD pattern), which is due to the volatility of Bi and Na elements) within the used sintering condition. Further, it can be noticed that the relative intensity of NZ$_{0.3}$FO peaks increase with its concentration in the composite.

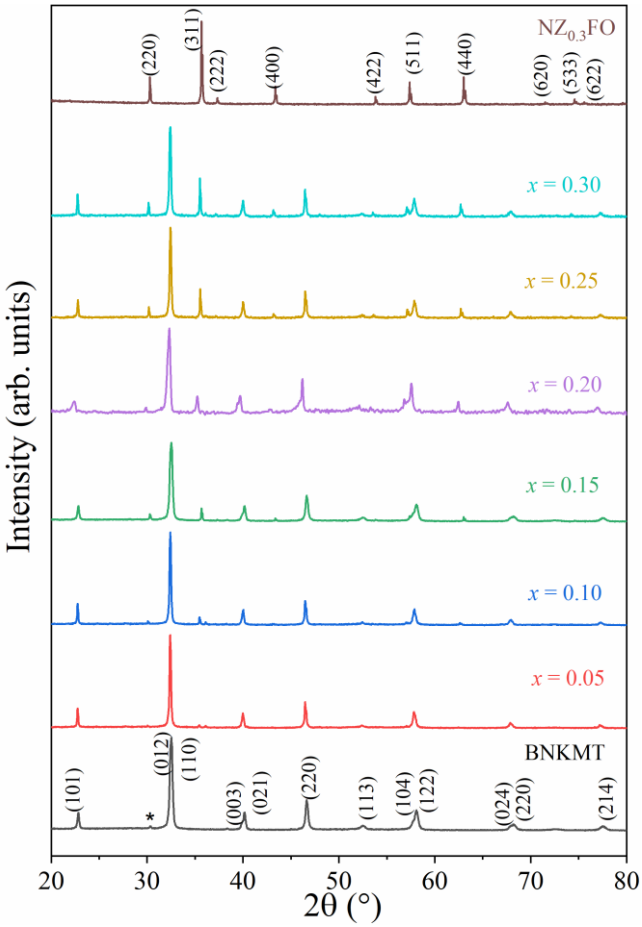

Figure 5.25. XRD pattern of sintered BNKMT, $NZ_{0.3}FO$ and composites (1-*x*)BNKMT-*x*$NZ_{0.3}FO$ specimens sintered at 1050 °C for 1h.

5.4.2 Raman study

The Raman spectra of BNKMT, $NZ_{0.3}FO$ and (1-*x*)BNKMT-*x*$NZ_{0.3}FO$ composites ranging from 100-800 cm^{-1} is shown in **Figure 5.26**. For pure BNKMT, three Raman bands has been observed similar to pristine BNT and designated as X, Y and Z. The X, Y and Z band reflects the A-O, B-O, and B-O_6 octahedra vibrations respectively for ABO_3-perovskite structure of BNKMT. On the other hand, three-Raman bands were observed for $NZ_{0.3}FO$ namely P, Q and R. The P and Q bands demonstrates the vibrations at octahedral site, whereas R corresponds to the vibrations at tetrahedral site [145]. In composite, the bands correspond to both phases coexists. However, the bands of $NZ_{0.3}FO$ merges are obscured under the BNKMT bands. The observation of lower intensity R band for $x > 0.1$ also support the relative phase fraction. Further, no significant change in the peak positions confirm the absence of micro-strain at the interphase boundaries.

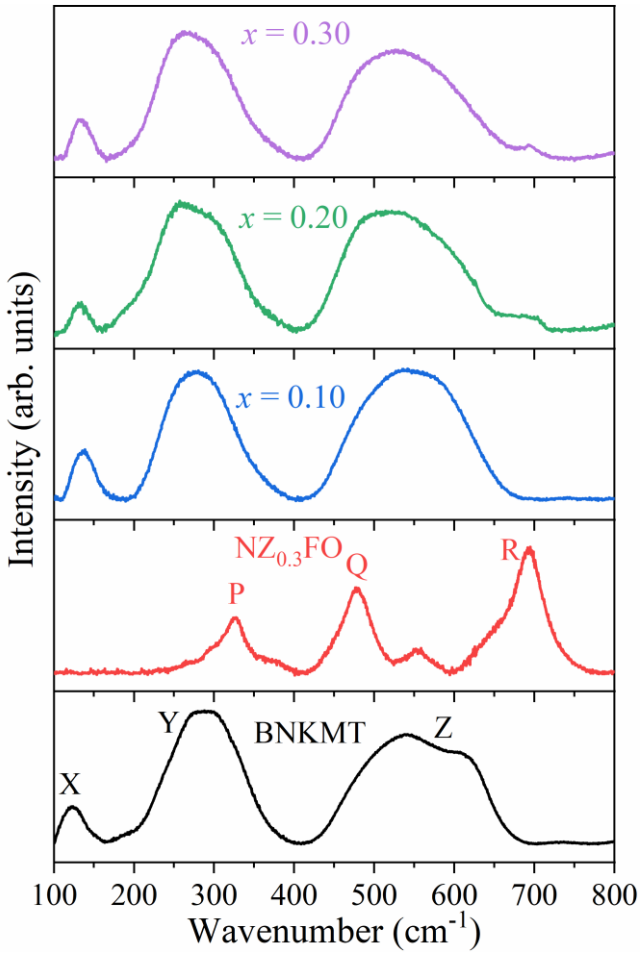

Figure 5.26. Raman spectra of pure BNKMT, NZFO and 0.80BNKMT-0.20$NZ_{0.3}$FO specimens.

5.4.3 Microstructural analysis

The SEM micrographs of the sintered (1-*x*)BNKMT-*x*$NZ_{0.3}$FO specimens has been represented in **Figure 5.27**. The BNKMT exhibits nearly cube like grains along with the abnormal rod like structure of the secondary phase (**Figure 5.27**(a)). On the other hand, $NZ_{0.3}$FO grains are relatively smaller (**Figure 5.27**(d)) than BNKMT. A well distinguishable larger BNKMT grains with small $NZ_{0.3}$FO grains has been observed in the composite specimens as depicted in **Figure 5.27**(b) & (c). It can be noticed that the number of smaller grains increase with $NZ_{0.3}$FO content that indicates the $NZ_{0.3}$FO grains are smaller in size.

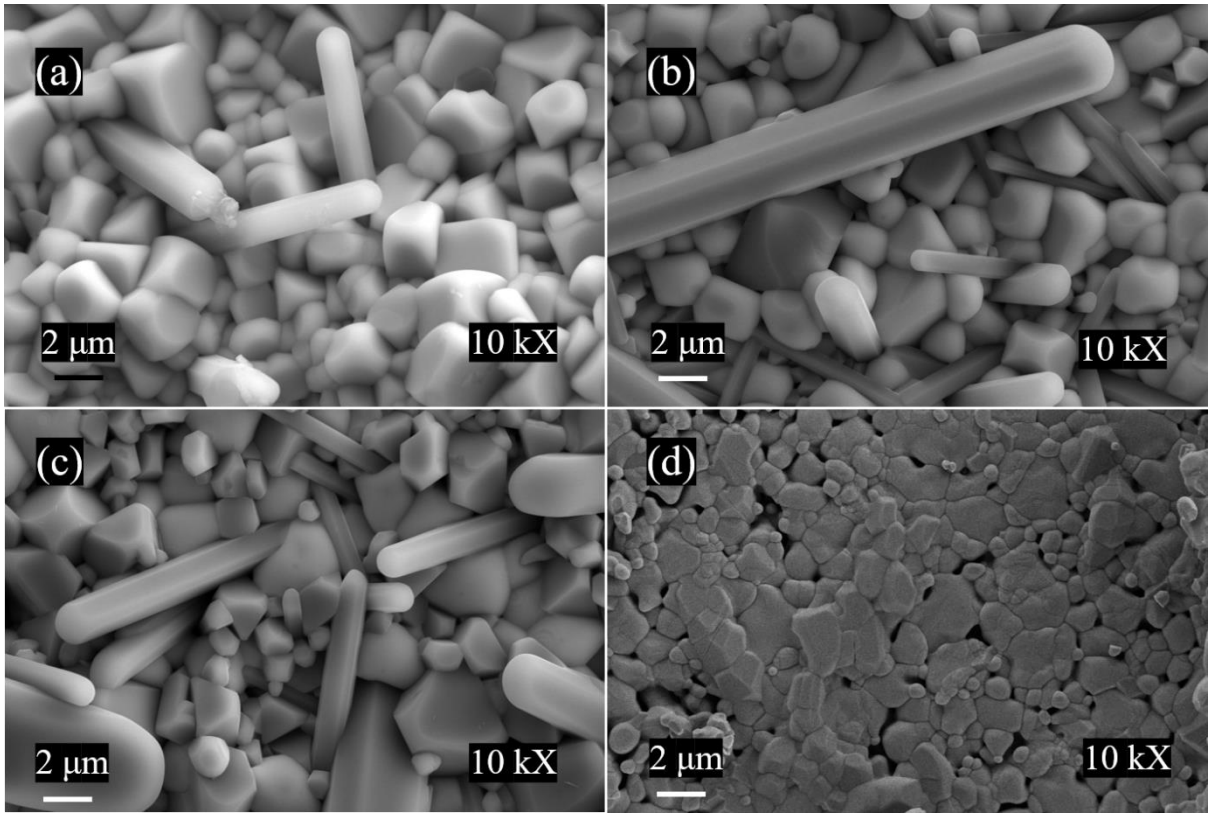

Figure 5.27. SEM micrographs of (1-*x*)BNKMT-*x*$NZ_{0.3}$FO sintered ceramics, where (a) $x = 0$, (b) $x = 0.10$, (c) $x = 0.30$, (d) $x = 1$.

For further clarification, a representative backscattered electron image and elemental mapping of sintered 0.80BNKMT-0.20$NZ_{0.3}$FO composite is displayed in **Figure 5.28**(a) & (b) respectively. The observation of bright and dark grains confirms the presence of distinct phases (**Figure 5.28**(a)). Further, elemental mapping reveals the bright grains correspond to BNKMT phase and smaller dark grains reflect the $NZ_{0.3}$FO phase. Interestingly, abnormal rod-like dark grains reflect the FE phase with Bi and Na deficiency, as already indicated by XRD pattern of BNKMT. The difference in the grain size of distinct phases indicates the simultaneous pinning effect, where the growth of one phase hinders the growth of another phase. As BNKMT is the major phase in composite and its pinning on NZFO is dominant over the NZFO on BNKMT [81]. Therefore, relatively larger grains have been observed BNKMT than NZFO. In the elemental mapping, Na and Mg are not displayed as they are beyond the detection limit of an instrument.

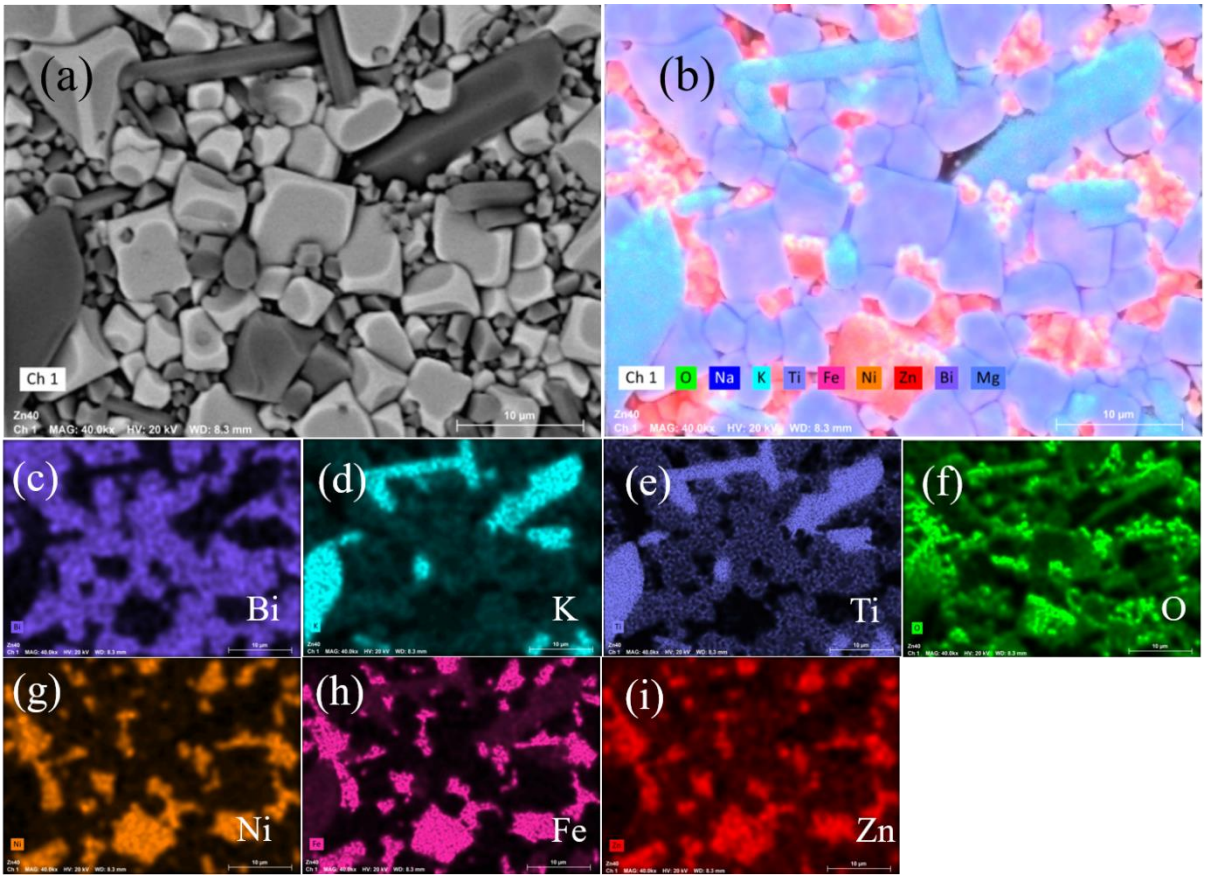

Figure 5.28. (a) Backscattered image and (b) elemental color mapping of 0.80BNKMT-0.20NZ$_{0.3}$FO composite. (c)- (i) Elemental mapping on the same surface for individual element.

5.4.4 Dielectric study

Figure 5.29 shows the *RT* dielectric behavior of the BNKMT and (1-x)BNKMT-*x*NZ$_{0.3}$FO composites in the *f* range of 10^2 Hz to 10^6 Hz. The ε_r decreases in the lower *f* range (10^2 - 10^4 Hz) and a gradual decrease within the higher *f* range (10^4 - 10^6 Hz). As per the concepts of Maxwell-Wagner polarization and Koop's two-layer model, the dielectric response at lower *f* is characterized by the presence of discrete grains and grain boundaries. Conversely, at higher *f*, only the grains themselves play a role in the polarization process [154]. As the concentration of ferrite increases, ε_r decreases and tan δ increases that indicates the induction of a phase that have relatively low resistivity.

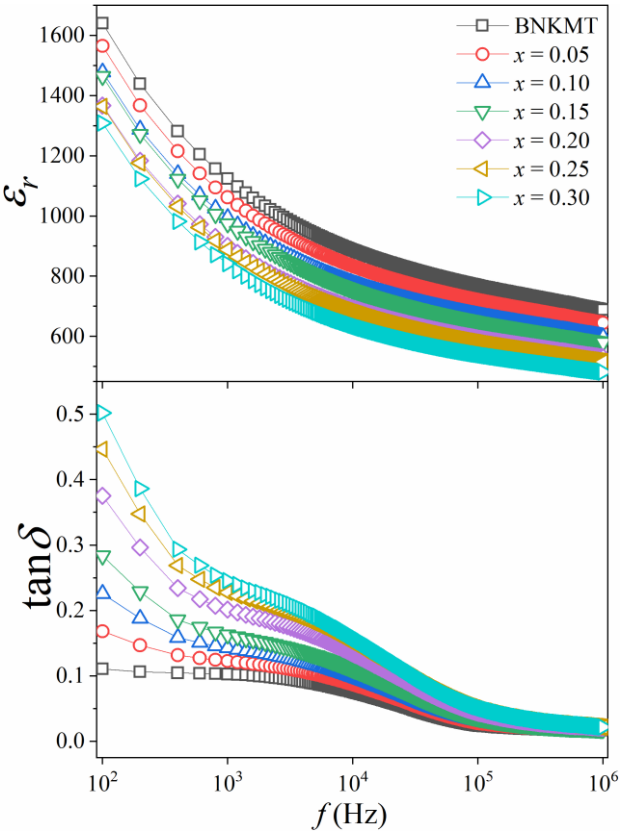

Figure 5.29. Variation in ε_r and tanδ for BNKMT and (1-x)BNKMT-xNZ$_{0.3}$FO composite specimens.

5.4.5 Leakage current measurement

Further, the low resistive behavior of NZ$_{0.3}$FO phase is confirmed by the increase in J as shown in **Figure 5.30**.

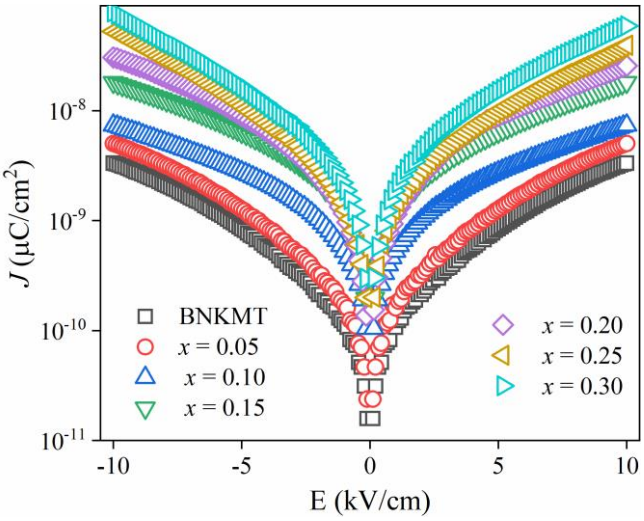

Figure 5.30. *J-E* curves for pure BNKMT and (1-x)BNKMT-xNZ$_{0.3}$FO composite specimens.

A sharp rise in *J* till 1 kV/cm reveals the contribution of space charges. Above 1 kV/cm, a gradual increase suggest the contribution of grain boundaries and Poole-Frenkel emission [136,137]. The increment in $NZ_{0.3}FO$ content is associated with a rise in *J*, indicating its comparatively lower resistivity in comparison to BNKMT. This change in *J* could have an adverse effect on the *P* of the composites. Therefore, achieving an ideal weight fraction within the 0-3 composite becomes crucial for maximizing the effectiveness of the *ME* coupling

5.4.6 Ferroelectric study

Further, **Figure 5.31**(a) illustrates the *RT P-E* loops of BNKMT and (1-*x*)BNKMT-*x*$NZ_{0.3}FO$ composites at 10 Hz. All the composites exhibit FE hysteresis loops due to the presence of FE BNKMT phase. The FE BNKMT exhibit good P_r (~ 9.98 μC/cm^2) and low E_c (~13.59 kV/cm).

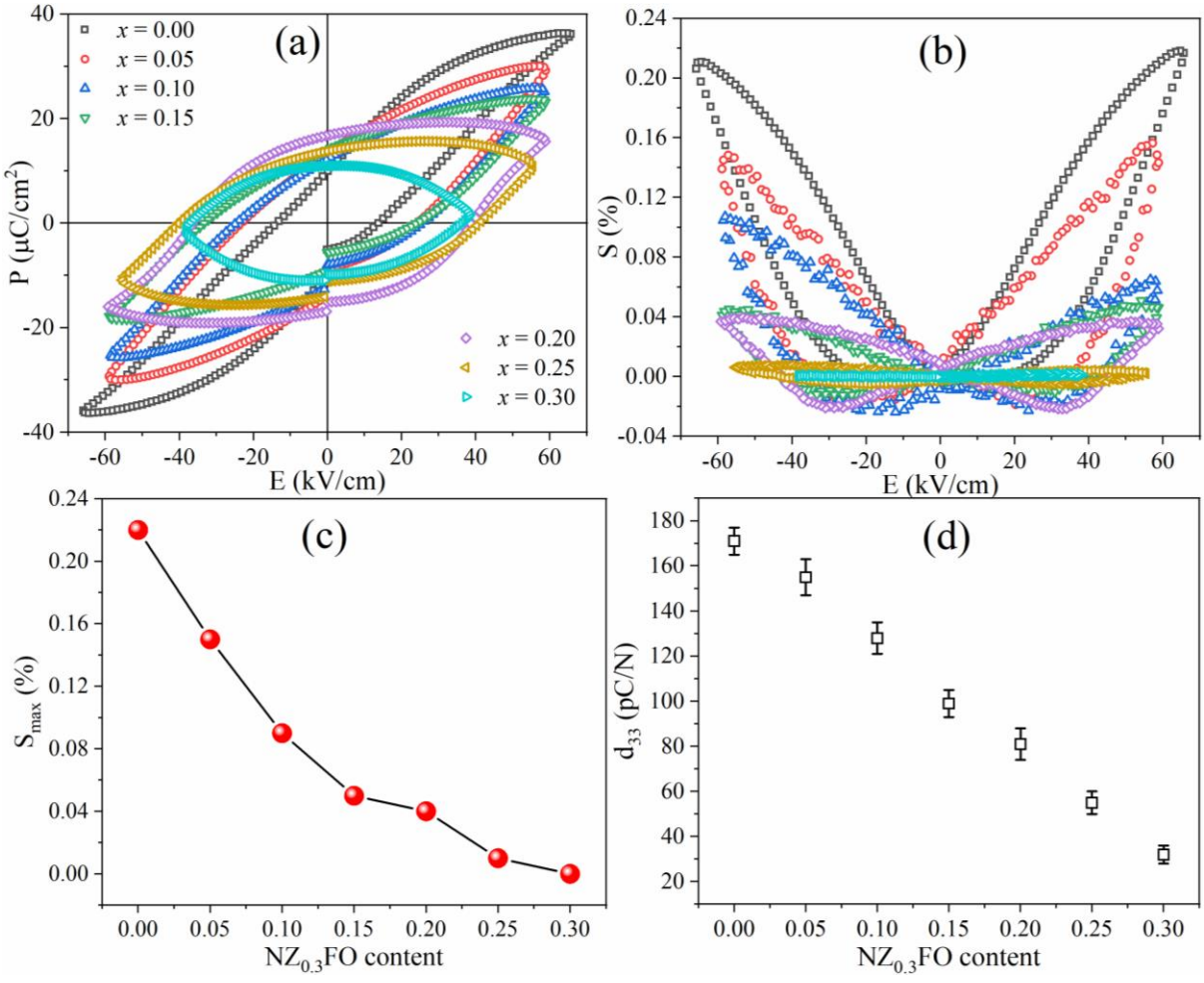

Figure 5.31. Variation in (a) *P-E* loops and (b) *S-E* curves of BNKMT and (1-*x*)BNKMT-*x*$NZ_{0.3}FO$ specimens. Influence of $NZ_{0.3}FO$ substitution on (c) S_{max} and (d) d_{33} of the BNKMT-$NZ_{0.3}FO$ specimens.

Furthermore, a noticeable reduction in P_s has been observed with the inclusion of non-FE $NZ_{0.3}FO$ content, which can be attributed to the relative decrease in the FE phase. Additionally, the introduction of a low-resistivity NFO content enhances the conduction losses within the composite material, which causes the lossy *P-E* loops (negative slope of *P* at high *E*). As a consequence, composites containing higher proportions of NFO are unable to resist high *E* effectively. Further, **Figure 5.31**(b) illustrates the bipolar *S-E* loops of BNKMT and (1-*x*)BNKMT-*x*$NZ_{0.3}FO$ composites at a *f* of 10 Hz. It can be observed that the incorporation of the non-piezoelectric $NZ_{0.3}FO$ phase results in a significant reduction in *S*, as depicted in **Figure 5.31**(c). Similarly, an evident decline in the d_{33} has been observed with $NZ_{0.3}FO$ content, as depicted in **Figure 5.31**(d).

5.4.7 Magnetic behavior analysis

Figure 5.32 illustrates the *RT M-H* hysteresis loops of composites (1-*x*)BNKMT-*x*$NZ_{0.3}FO$ under ±10 kOe. The slim magnetic hysteresis loop has been observed in all the composites, which is attributed to the presence magnetic $NZ_{0.3}FO$ phase. Therefore, an enhancement in the M_s of the composites has been observed with $NZ_{0.3}FO$ content. The inset of **Figure 5.32** represents the magnetic properties of $NZ_{0.3}FO$ that reveals its $M_s \sim 74.52$ emu/g.

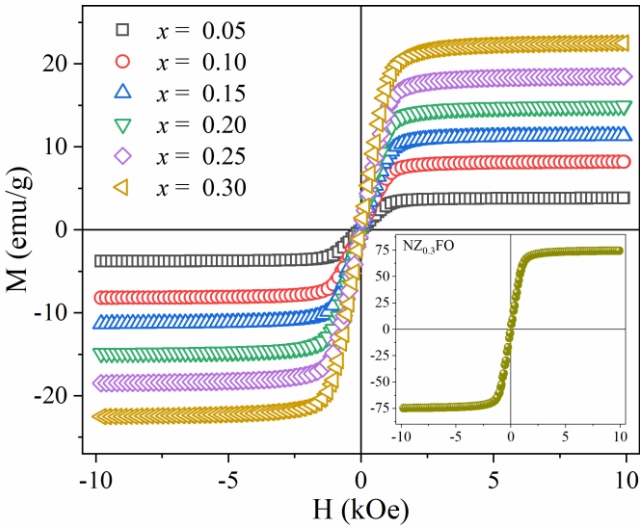

Figure 5.32. *M-H* loops of (1-*x*)BNKMT-*x*$NZ_{0.3}FO$ composites, where inset represents the magnetic behavior of pure $NZ_{0.3}FO$ ceramics.

5.4.8 ME measurements

The α_{ME} for (1-*x*)BNKMT-*x*$NZ_{0.3}FO$ composites as a function of H_{dc} at H_{ac} of 3 Oe and 10 Hz has shown in **Figure 5.33**(a).

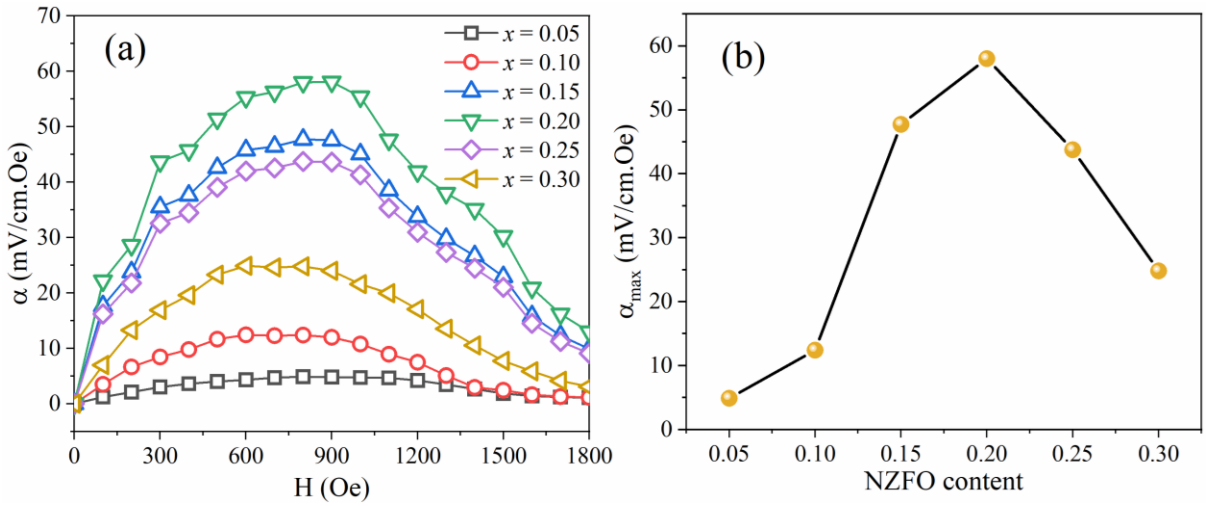

Figure 5.33. Variation in α_{ME} with (a) H_{dc} at 3 Oe H_{ac} and 10 Hz, (b) $NZ_{0.3}FO$ content at 800 Oe for (1-*x*)BNKMT-*x*NFO composites.

The α_{ME} increases with H_{dc} till 800 Oe and decreases afterward that suggest the maximum strain mediated coupling occurred at 800 Oe. As $NZ_{0.3}FO$ content increases, α_{ME} also increases till x = 0.20 content and thereafter decreases (**Figure 5.33**(b)). The maximum obtained value of α_{ME} is 58.12 mV/cm.Oe for 0.80BNKMT-0.20NFO composite, which has not been reported in the particulate composite so far at such low frequency operation. Moreover, the α_{ME} is 12.34 times higher than the BNT-NFO and 1.67 times higher than the BNKMT-NFO composites. This indicates that BNKMT-$NZ_{0.3}FO$ composite could be viable candidate for the low frequency *ME* devices. For $x < 0.20$, the α_{ME} is low due to the small fraction of magnetostrictive phase. For $x > 0.20$, the excess amount of NFO content hinders the FE dipole alignments (already suggested by *P-E* loop measurements) that cause the lower value of α_{ME}. A comparison of BNKMT-$NZ_{0.3}FO$ composite with other particulate composites are shown in **Table 5.1**.

Table 5.1. Comparison of α_{ME} for *ME* particulate composites at different frequencies.

Composite	***f* (Hz)**	**α_{ME} (mV/cm.Oe)**	**Ref.**
$0.68Pb(Zr_{0.52}Ti_{0.48})O_3$-$0.32NiFe_2O_4$	1000	80	[128]
$0.6(Ba_{0.85}Ca_{0.15})(Zr_{0.1}Ti_{0.9})O_3$-$0.4CoFe_2O_4$	1000	7.75	[155]
$0.8Pb(Zr_{0.52}Ti_{0.48})O_3$-$0.2CoFe_2O_4$	1000	1.6	[156]

$0.7Pb(Zr_{0.52}Ti_{0.48})O_3$-$0.3NiFe_2O_4$	1000	0.5	[157]
$0.6(Bi_{0.5}Na_{0.5}TiO_3)$-$0.4(Ni_{0.2}Co_{0.8}Fe_2O_4)$	999	7.54	[113]
$0.65(Bi_{0.5}Na_{0.5}TiO_3$-$Bi_{0.5}K_{0.5}TiO_3)$- $0.35(Ni_{0.8}Zn_{0.2}Fe_2O_4)$	1000	42.41	[158]
$0.8(Bi_{0.5}Na_{0.5}TiO_3)$-$0.2(Ni_{0.5}Zn_{0.5}Fe_2O_4)$	10	4.33	[108]
$0.5Ba_{0.85}Ca_{0.15}Zr_{0.10}Ti_{0.90}O_3$– $0.5Ni_{0.7}Zn_{0.3}Fe_2O_4$	1000	14.5	[159]
$Pb(Zr_{0.52}Ti_{0.48})O_3$–$Ni_{0.8}Zn_{0.2}Fe_2O_4$	1000	155	[160]
$0.8BNKMT$-$0.2NZ_{0.3}FO$	**10**	**58.12**	**This work**

Chapter 6

Results and discussion: Magnetoelectric 2-2 composites

Overview

In this chapter, the structural, FE, magnetic and *ME* properties of the laminate composite has been examined. The bilayer and trilayer laminate composites of BNKMT and $NZ_{0.3}FO$ are synthesized via novel direct diffusion bonding technique.

6.1 BNKMT/$NZ_{0.3}FO$ laminate composite

To further enhance the *ME* coupling in bulk ceramics, the 2-2 connectivity among the PE and magnetostrictive phases has been used. The bilayer and trilayer laminate composite comprising BNKMT and $NZ_{0.3}FO$ has been fabricated by using direct diffusion bonding technique in order to avoid the damping effect caused by conductive epoxy and limited optimum response of one phase by co-fired technique (discussed in section 2.3.1). The bilayer composite is BNKMT/$NZ_{0.3}FO$, whereas trilayer are BNKMT/$NZ_{0.3}FO$/BNKMT ($NZ_{0.3}FO$ is sandwiched between BNKMT phases) and $NZ_{0.3}FO$/BNKMT/$NZ_{0.3}FO$ (BNKMT is sandwiched between $NZ_{0.3}FO$ phases) composites as displayed in **Figure 6.1**. It is to be noted that the thickness of each layer is kept fixed at 0.65 mm. Further, the effect of the geometry on the *ME* properties of the composites has been investigated.

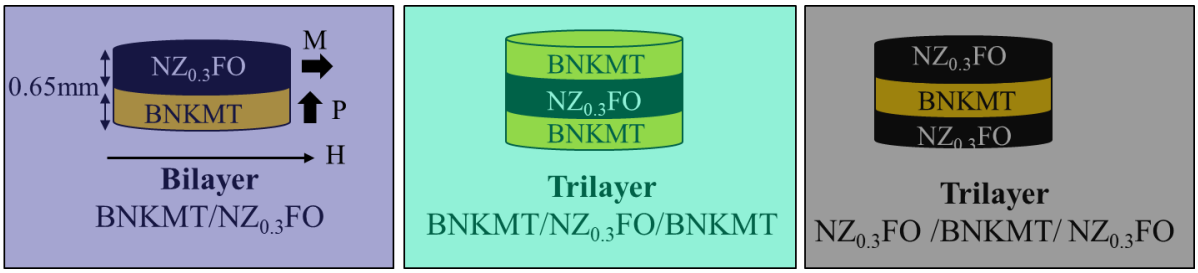

Figure 6.1. Schematic of bilayer BNKMT/$NZ_{0.3}FO$ and trilayer BNKMT/$NZ_{0.3}FO$/BNKMT and $NZ_{0.3}FO$/BNKMT/$NZ_{0.3}FO$ composites.

6.1.1 Phase analysis

The XRD pattern of BNKMT and $NZ_{0.3}FO$ side in bilayer BNKMT/$NZ_{0.3}FO$ composite is shown in **Figure 6.2**. The pattern of BNKMT exhibits characteristics diffraction peaks of the perovskite structure (matched with the JCPDS no. 36-0340). On the other hand, NZFO reveals the cubic structure (indexed with JCPDS card no. 10-0325). The absence of any extra peak in both phases indicates the lack of impurity phase within the used processing conditions.

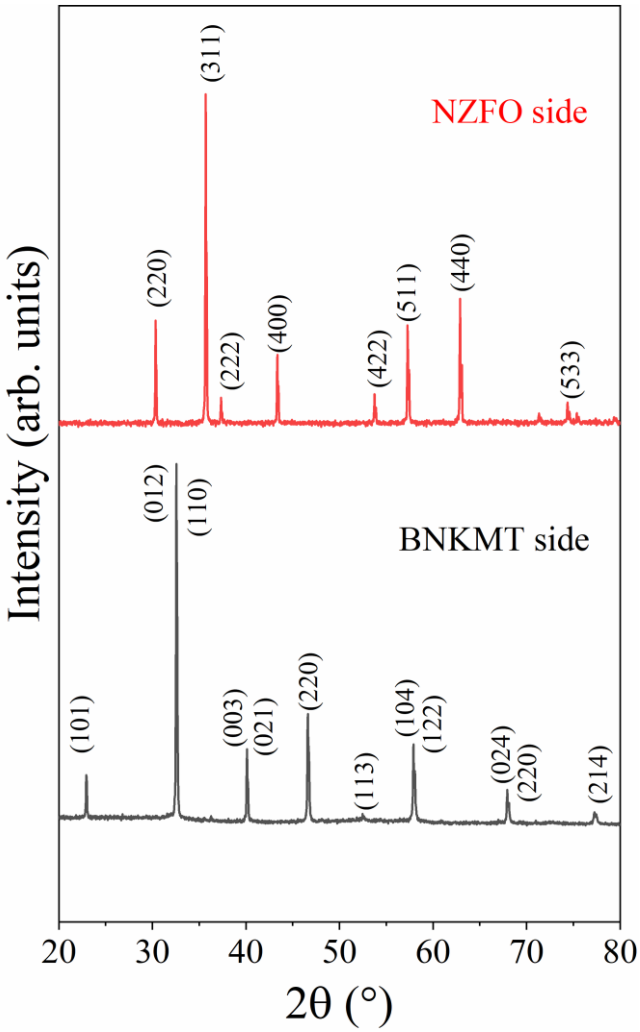

Figure 6.2. XRD pattern of BNKMT side and $NZ_{0.3}FO$ side of the BNKMT/$NZ_{0.3}FO$ bilayer composite.

6.1.2 Microstructural analysis

Further, the micrograph of BNKMT and $NZ_{0.3}FO$ side of laminate composite is depicted in **Figure 6.3**(a) & (b) respectively. A dense microstructure with cube shape grains for BNKMT and irregular large grains for $NZ_{0.3}FO$ has been observed. The average grain size of BNKMT (~ 0.64 μm) is smaller than $NZ_{0.3}FO$ (~ 2.08 μm) that support the relatively low temperature sintering conditions of BNKMT ceramics. Further, the cross-sectional view of fractured BNKMT/$NZ_{0.3}FO$ laminate at the interface is shown in **Figure 6.3**(c). A well distinguished phases can be seen in the micrograph without any porosity and cracks at their interface. The distinction between two phases is further confirmed by its backscattered electron micrograph (**Figure 6.3**(d)).

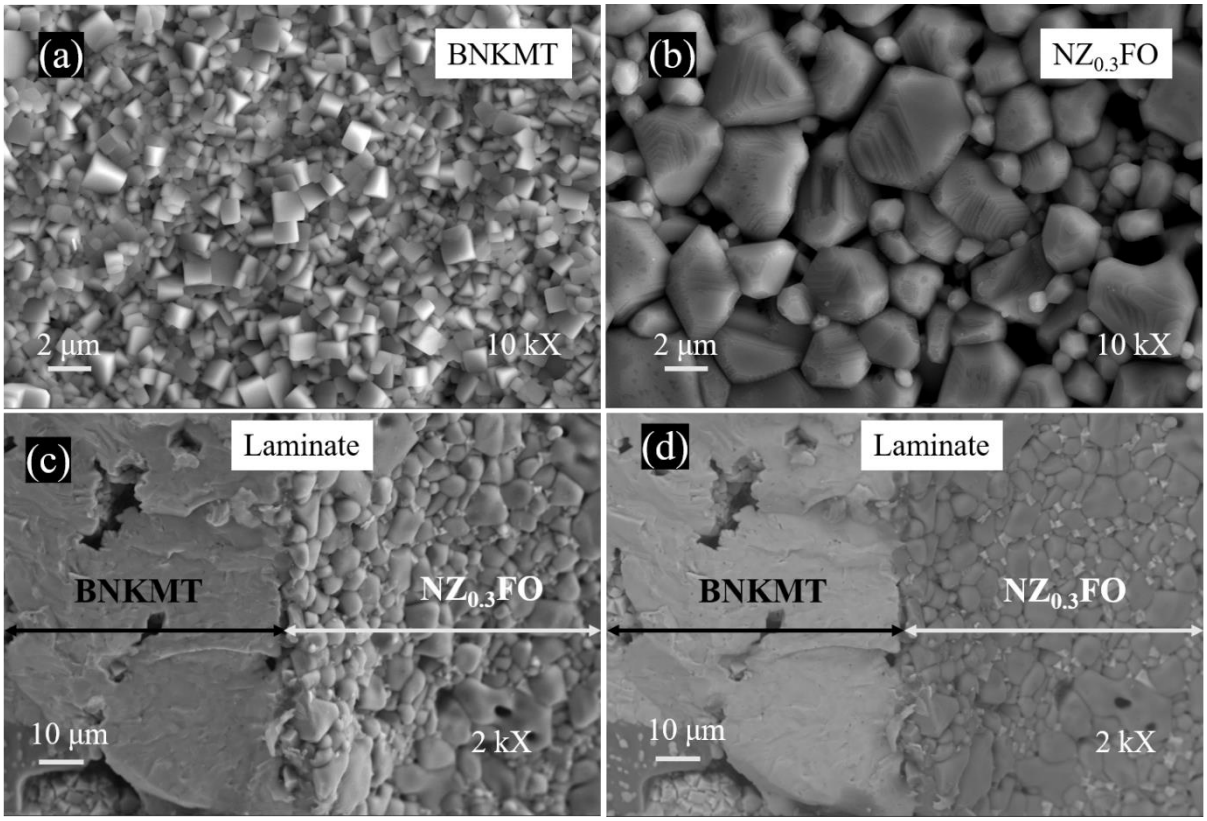

Figure 6.3. SEM micrograph of (a) BNKMT, (b) $NZ_{0.3}FO$ side in bilayer laminate composite. Cross-sectional (c) secondary electron and (d) backscattered electron image of fractured BNKMT/$NZ_{0.3}FO$ laminate.

The elemental mapping at 5 kX on its interface confirms the well separable BNKMT and $NZ_{0.3}FO$ phases with the inter-grain fusion between them at the interface as shown **Figure 6.4**.

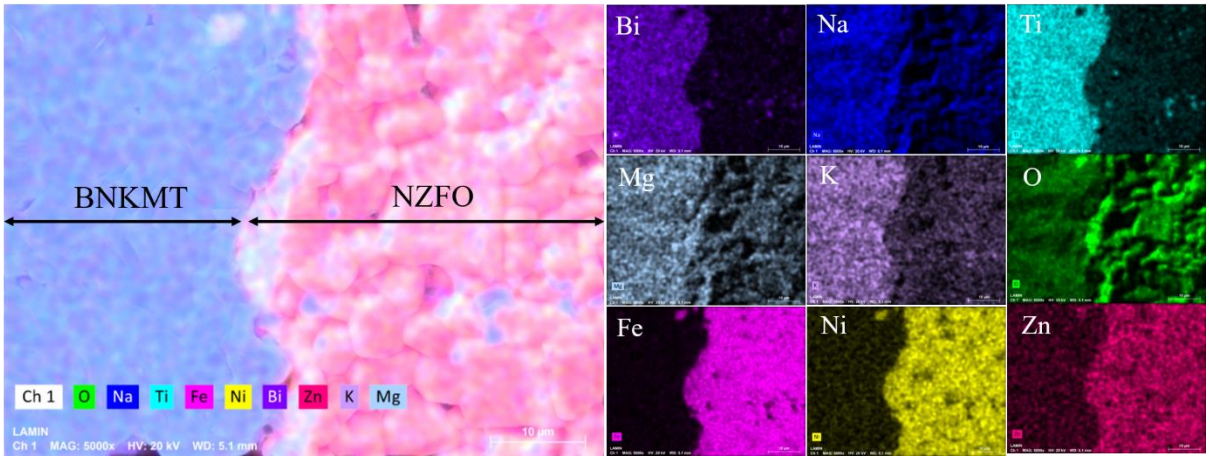

Figure 6.4. Elemental mapping of BNKMT/$NZ_{0.3}FO$ bilayer laminate at the interface.

6.1.3 Multiferroic study

Further, *P-E* and *I-E* has been examined for pure BNKMT at 10 Hz and represented in **Figure 6.5**(a).

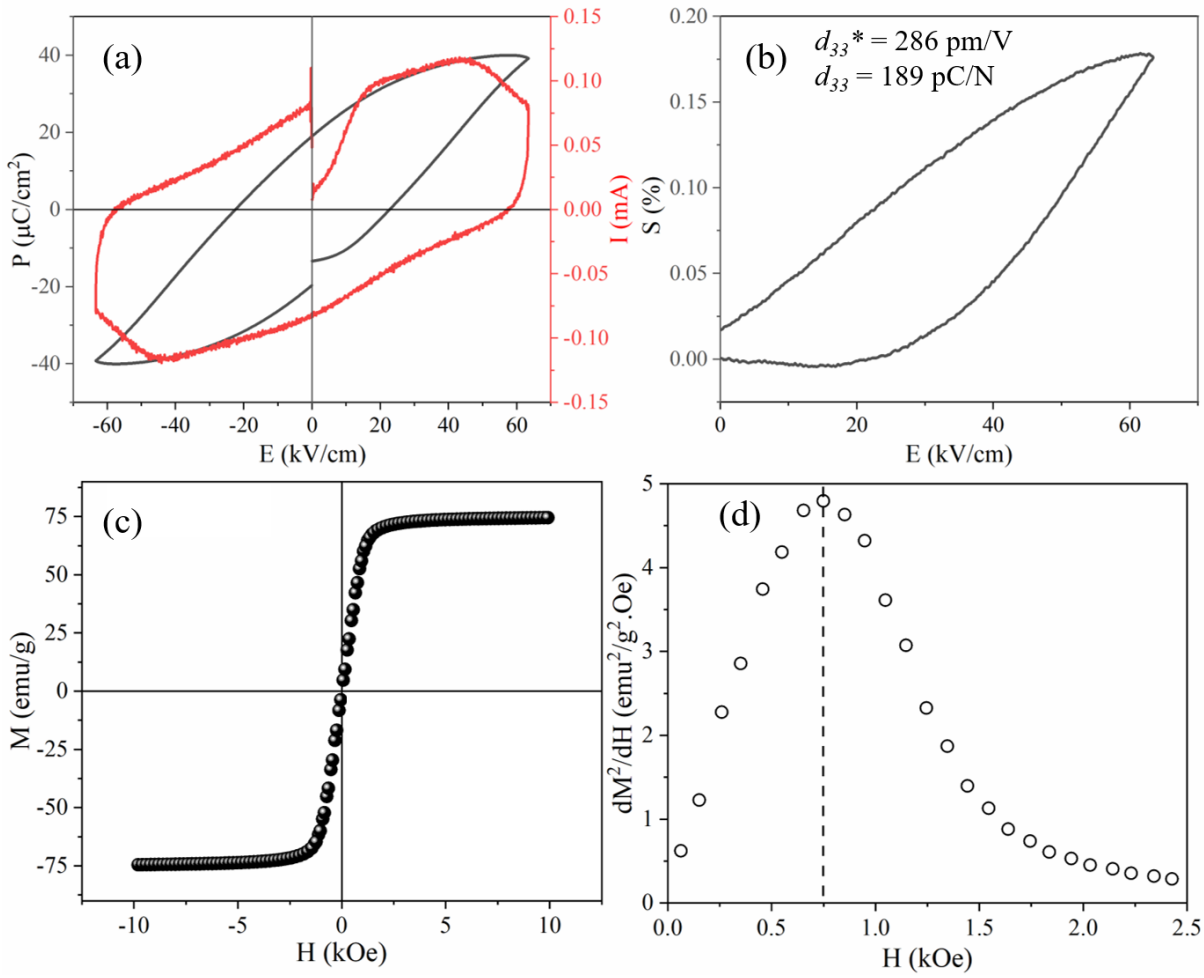

Figure 6.5. Variation in (a) *P*, *I* and (b) *S* with *E* at 10 Hz for BNKMT ceramics. (c) *M-H* loop and (d) dM^2/dH vs *H* plot of $NZ_{0.3}FO$ specimen.

A well saturated hysteresis has been observed for BNKMT with high saturation polarization (P_s ~ 40.01 μC/cm^2), good remanent polarization (P_r ~ 20.32 μC/cm^2) and low coercivity (E_c ~ 22.67 kV/cm). The *I-E* plot also confirmed the FE behavior of BNKMT, where maximum *I* has been obtained at 44.73 kV/cm suggesting the threshold field (where all ferroelectric domains are aligned in the direction of an applied *E*) of BNKMT. Further, the *S-E* plot of BNKMT is shown in **Figure 6.5**(b). A large value of *S* (~ 0.18 %) and d_{33}^* (~ 286 pm/V) has been observed for BNKMT along with observation of high d_{33} (~ 189 pC/N). A well saturated

magnetic hysteresis loop (*M-H*) has been observed for $NZ_{0.3}FO$ as depicted in **Figure 6.5**(c). The M_s ~ 74.52 emu/g and H_c of 9.17 Oe has been observed. Further, the *M-H* data is used to examine the qualitative q_s of $NZ_{0.3}FO$ by using equation 2.1. The dM^2/dH increases with *H* (suggest increase of strain sensitivity) up to its peak value (~ 4.8 emu^2/g^2.Oe at ~ 750 Oe) and decreases afterwards (decrease of strain sensitivity) as shown in **Figure 6.5**(d).

6.1.4 ME measurements

The α_{ME} *vs H* plot for bilayer and trilayer composites has follows the same trend of dM^2/dH *vs H* plot and depicted in **Figure 6.6**(a). The maximum α_{ME} for each laminate composite is observed around 750 Oe. The large α_{ME} has been observed for trilayer laminates than bilayer composites (**Figure 6.6**(b)) because an additional layer provides more interface, which improves interaction between distinct phases. For high output voltage response with applied *H*, appropriate choice of sample geometry is crucial.

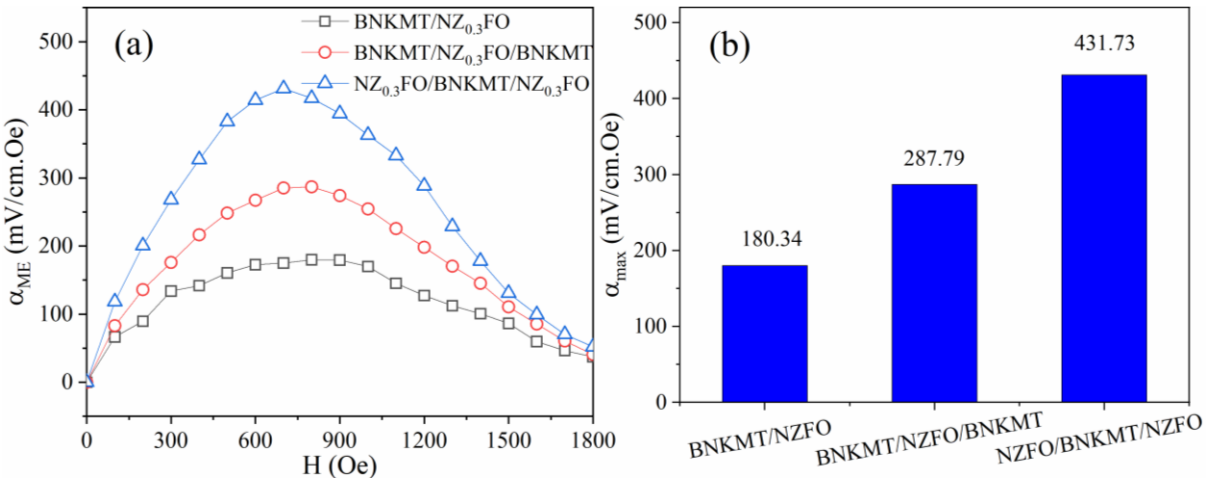

Figure 6.6. Variation in (a) α_{ME} with dc *H* at 3 Oe H_{ac} and 10 Hz frequency. (b) α_{max} for bilayer $BNKMT/NZ_{0.3}FO$ and trilayer $BNKMT/NZ_{0.3}FO/BNKMT$ and $NZ_{0.3}FO/BNKMT/NZ_{0.3}FO$ laminate composites.

In trilayer $NZ_{0.3}FO/BNKMT/NZ_{0.3}FO$ composite, magnetostrictive $NZ_{0.3}FO$ imparts strain on BNKMT from both sides. On the other hand, in trilayer $BNKMT/NZ_{0.3}FO/BNKMT$ composite, only one side of both BNKMT phases experiences the strain due to magnetostrictive $NZ_{0.3}FO$ phase that generates relatively low polarization in an applied *H*. However, $NZ_{0.3}FO/BNKMT/NZ_{0.3}FO$ trilayers shows higher α_{ME} than $BNKMT/NZ_{0.3}FO/BNKMT$ laminate as depicted in **Figure 6.6**(b). The observed α_{ME} for $NZ_{0.3}FO/BNKMT/NZ_{0.3}FO$ composite is higher as compared to the previously investigated PZT/NFO, $Ba_{0.9}Ca_{0.1}Ti_{0.9}Zr_{0.1}O_3/Co_{0.8}Ni_{0.1}Zn_{0.1}Fe_2O_4$,

$Li_{0.058}(Na_{0.535}K_{0.48})_{0.942}NbO_3/Co_{0.6}Zn_{0.4}Fe_{1.7}Mn_{0.3}O_4$, $[Ba(Zr_{0.2}Ti_{0.8})O_3\text{-}0.5(Ba_{0.7}Ca_{0.3})TiO_3]$ /$Ni_{0.8}Zn_{0.2}Fe_2O_4$ and $0.65Pb(Mg_{1/3}Nb_{2/3})O_3–0.35PbTiO_3$/ $Ni_{0.8}Zn_{0.2}Fe_2O_4$ laminate composites (2.3 – 406 mV/cm.Oe) [161–165] that suggest the material could be used for the practical devices (**Table 6.1**).

Table 6.1. Comparative α_{ME} of several laminate composites.

Composite	***f* (Hz)**	α_{ME} **(mV/cm.Oe)**	**References**
$PbZr_{0.53}Ti_{0.47}O_3/NiFe_2O_4$	1000	2.3	[161]
$Ba_{0.9}Ca_{0.1}Ti_{0.9}Zr_{0.1}O_3/Co_{0.8}Ni_{0.1}Zn_{0.1}Fe_2O_4$	1000	21.73	[162]
$Li_{0.058}(Na_{0.535}K_{0.48})_{0.942}NbO_3/Co_{0.6}Zn_{0.4}Fe_{1.7}Mn_{0.3}O_4$	1000	285	[163]
$BaZr_{0.2}Ti_{0.8}O_3$-0.5 $Ba_{0.7}Ca_{0.3}TiO_3/Ni_{0.8}Zn_{0.2}Fe_2O_4$	1000	320	[164]
$0.65PbMg_{1/3}Nb_{2/3}O_3–0.35PbTiO_3$/ $Ni_{0.8}Zn_{0.2}Fe_2O_4$	1000	406	[165]
$NZ_{0.3}FO/BNKMT/NZ_{0.3}FO$	**10**	**431.73**	**This work**

Chapter 7

Summary and Conclusions

Overview

A summary of the results from the experiments discussed in the previous chapters are presented in this chapter. Initially, the effect of varying relative weight fraction on *ME* coupling in 0-3 composites is outlined. The impact of bilayer and trilayer laminates on the *ME* coupling has been concluded. At the end, the potential avenues for further research are discussed.

7.1 Summary

In this work, the PE BNT and BNKMT ceramics and magnetostrictive NZ_xFO ceramics have been prepared by sol-gel and solid-state reaction route for making their particulate and laminate composites. The structural, electrical, magnetic and *ME* properties in the BNT-NFO and BNKMT-NFO particulate composites has been studied by varying their relative weight fraction. Further, the variation in magnetic and *ME* properties on Zn substitution in NFO coupled with BNKMT phase has been investigated. Furthermore, the *ME* properties in BNKMT-$NZ_{0.3}FO$ particulate composites by varying their relative weight fraction has been examined. The structural and *ME* properties has also conducted for the bilayer and trilayer laminate composite of BNKMT and $NZ_{0.3}FO$. The crucial findings of this work summarize as follows:

- An excellent FE (P_s ~ 40.01 μC/cm^2, P_r ~ 20.32 μC/cm^2 and E_c ~ 22.67 kV/cm) and PE properties (S ~ 0.18 %, d_{33}^* ~ 286 pm/V and d_{33} ~ 189 pC/N) for BNKMT and good magnetic properties (M_s ~ 74.52 emu/g, H_c ~ 9.17 Oe and dM^2/dH ~ 4.8 emu^2/g^2.Oe at 750 Oe) for $NZ_{0.3}FO$ has been observed.
- Initially, the *ME* coupling in (1-x)BNT-xNFO composites (x = 0.05 - 0.30; Δx = 0.05) have been investigated. The coexistence of both phases has been confirmed by XRD and FE-SEM. The Raman spectroscopy suggested absence of interfacial micro-strains between BNT and NFO phase. All samples showed good *ME* coupling and highest α_E ~ 4.71 mV/cm.Oe at 1000 Oe is obtained for 0.80BNT-0.20NFO at 10 Hz.
- Further, the *ME* coupling in (1-x)BNKMT-xNFO composites (x = 0.05 - 0.30; Δx = 0.05) have been investigated. The strong *ME* coupling is evident in all composite specimens, and the composition 0.80BNKMT-0.20NFO demonstrated the highest α_E ~ 34.69 mV/cm.Oe at 1000 Oe and 10 Hz. Among the BNT-NFO and BNKMT-NFO composites, the relatively better *ME* coupling has been observed in BNKMT-NFO composite due to the higher d_{33} of BNKMT.
- Furthermore, the effect of magnetostrictive phase (NZ_xFO; x = 0, 0.1, 0.2, 0.3, 0.4 and 0.5) on *ME* coupling has been examined by coupled it with BNKMT phase in the fixed weight ratio of 20:80 respectively. The Zn substitution enhances the M_s. The *ME* effect in 0.8BNKMT-0.2NZ_xFO composite series has been modulated by the mean of increase in piezomagnetism, where α_E has been found to increase with Zn substitution till x = 0.3 (i.e., 58.12 mV/cm.Oe at 10 Hz) and decrease thereafter. The same is correlated with the q_s

behavior, where its variation has been supported with initial permeability. The Raman spectroscopy revealed the distribution of Zn cations at both A and B-sites. The *ME* study of 0.8BNKMT-0.2NZ_xFO composite reveals the promising behavior of BNKMT as PE phase and $NZ_{0.3}$FO as magnetostrictive phase.

- The *ME* particulate composite of (1-*x*)BNKMT-*x*$NZ_{0.3}$FO (*x* = 0.05-0.30; Δ*x* = 0.05) were successfully synthesized and its structural, magnetic, FE and *ME* properties has been investigated. The addition of $NZ_{0.3}$FO caused the magnetic behavior of composite as it exhibited good M_s ~ 74.52 emu/g. An excellent *ME* response has been observed for all the specimens and obtained maximum for 0.80BNT-0.20NZFO, i.e., 58.12 mV/cm.Oe at low *H* (800 Oe) and *f* (10 Hz).
- Lastly, the *ME* study has been undertaken for the bilayer and trilayer laminates of BNKMT and $NZ_{0.3}$FO. These composites are successfully synthesized by the direct diffusion of the ceramics. The relatively higher α_E has been observed for trilayer $NZ_{0.3}$FO/BNKMT/$NZ_{0.3}$FO composite (~ 431.73 mV/cm.Oe) than bilayer BNKMT/$NZ_{0.3}$FO (~ 180.34 mV/cm.Oe) and trilayer BNKMT/$NZ_{0.3}$FO/BNKMT (~ 287.79 mV/cm.Oe). This suggest the PE phase should be sandwich between two magnetostrictive phases in order to achieve substantially large *ME* coupling.

The obtained *ME* coupling coefficient (α_E) among the studied composite series has been shown in the **Table 7.1**.

Table 7.1. Comparative α_E in the studied composite series.

Composite	**Connectivity**	**α_E (mV/cm.Oe)**
0.8BNT-0.2NFO	0-3	4.71
0.8BNKMT-0.2NFO	0-3	34.69
0.8BNKMT-0.2$NZ_{0.3}$FO	0-3	58.12
BNKMT/$NZ_{0.3}$FO	2-2	180.34
BNKMT/$NZ_{0.3}$FO/BNKMT	2-2	287.79
$NZ_{0.3}$FO/BNKMT/$NZ_{0.3}$FO	2-2	431.73

7.2 Conclusions

1. The d_{33} increases in BNT from 78 pC/N to 189 pC/N in BNKMT with the formation of solids solutions due to MPB.
2. The incorporation of Zn in the NFO enhances the PM coefficient due to the colinear magnetic ordering of the spins at B-site.
3. Zn substitution in the NFO also enhances the M_s as Zn^{2+} cations preferably occupy tetrahedral void positions.
4. The direct diffusion bonding could be better than the epoxy and co-firing technique as both phases are processed at their optimal sintering temperature.
5. Laminate composites possess better *ME* properties than particulate composites due to better connectivity and better strain transfer.

7.3 Future Scope

Undoubtedly, the remarkable *ME* coupling has been achieved in the BNKMT-$NZ_{0.3}FO$ particulate and laminate composites. However, there are few challenges still remain to explore, and can be addressed in future to improve *ME* properties for practical applications.

- ✓ The formation of abnormal rod-like grains hinders the piezoelectric response. However, for achieving good *ME* response in 0-3 composite, the relative density ~ 95 % is prerequisite, which can be achieved at high sintering temperature in the resistive furnace. To avoid this limitation, the composite specimen can be optimized using cold sintering technique.
- ✓ The *ME* study of both 0-3 and 2-2 composites has been conducted at off-resonant condition. However, the *ME* coupling can be obtained substantially large at resonant frequency and these composite warrant attention for the study at resonant conditions.
- ✓ The *ME* response observed in the trilayer laminate composite is relatively better than bi-layer composites, which can be further improved in the multilayer composites of more than three alternate phase layers.
- ✓ The texturing of BNKMT can be performed in order to improve d_{33}, which is directly corelated to the α_E.

List of Publications

1. **P. Singh,** R. Laishram, P. Sharma, J. Kolte, Electric field and temperature dependent ferroelectric behavior of $Bi_{0.5}Na_{0.5}TiO_3$-$Bi_{0.5}K_{0.5}TiO_3$-$BiMg_{0.5}Ti_{0.5}O_3$ piezoceramics. *Mater. Sci. Semicond. Process.* **167,** 107816 (2023). https://doi.org/10.1016/j.mssp.2023.107816.
2. **P. Singh**, R. Laishram, J. Kolte and P. Sharma, High magnetoelectric coupling in piezoelectric modified BNT and magnetic NZFO particulate composite. *Solid State Sci.* **148,** 107438 (2024). https://doi.org/10.1016/j.solidstatesciences.2024.107438.
3. **P. Singh**, R. Laishram, J. Kolte and P. Sharma, Low frequency magnetoelectric effect in $Bi_{0.5}Na_{0.5}TiO_3$-$Ni_{0.5}Zn_{0.5}Fe_2O_4$ particulate composites. *Electron. Mater. Lett.* **19**, 442-451 (2023). https://doi.org/10.1007/s13391-023-00423-6.
4. **P. Singh**, R. Laishram, P. Sharma and J. Kolte, Giant magnetocapacitance in magnetoelectric BNT/NFO particulate composites. *J Mater Sci: Mater Electron* **32,** 21288–21296 (2021). https://doi.org/10.1007/s10854-021-06631-w.
5. **P. Singh**, J. Kolte and P. Sharma, "Structural and electrical properties of lead-free (1-x)$Bi_{0.5}Na_{0.5}TiO_3$-x$Ni_{0.5}Zn_{0.5}Fe_2O_4$ based magnetoelectric composites," *2021 IEEE International Symposium on Applications of Ferroelectrics (ISAF)*, 2021, pp. 1-4, doi: 10.1109/ISAF51943.2021.9477314.

Other Publications

1. **P. Singh,** A. Sharma, P. Sharma and J. Kolte, Investigation of phase, structural, and electrical properties of BNT–BT solid solutions in the vicinity of MPB regime. *Appl. Phys. A* 129, 643 (2023). https://doi.org/10.1007/s00339-023-06933-2.

List of Publications (Under Review)

1. **P. Singh**, R. Laishram, P. Sharma and J. Kolte, Modulation of magnetoelectric coupling in the low frequency regime.
2. **P. Singh,** R. Laishram, P. Sharma, J. Kolte, Giant magnetoelectric coupling in modified BNT/NZFO laminates via direct diffusion bonding.

List of Conferences

1. Poster presentation in International Conference on *IEEE International Symposium on Applications of Ferroelectrics (ISAF)* at University of New South Wales, Sydney, Australia on 16-21 May, 2021.
2. Poster presentation in International Conference on Advanced Materials and Devices for Futuristic Applications (IC-AMDFA) at Chandigarh University, Chandigarh on 23-24 November, 2021.
3. Oral presentation in International Symposium on Advances in piezoelectrical (ISAP) at C-MET, Thrissur on 14-15 July, 2022.

Reference

[1] M. Fiebig, Revival of the magnetoelectric effect, J. Phys. D. Appl. Phys. 38 (2005) 123–152. https://doi.org/10.1088/0022-3727/38/8/R01.

[2] N. Hur, S. Park, P.A. Sharma, J.S. Ahn, S. Guha, S.W. Cheong, Electric polarization reversal and memory in a multiferroic material induced by magnetic fields, Nature. 429 (2004) 392–395. https://doi.org/10.1038/nature02572.

[3] R.P.S.M. Lobo, R.L. Moreira, D. Lebeugle, D. Colson, Infrared phonon dynamics of a multiferroic $BiFeO_3$ single crystal, Phys. Rev. B - Condens. Matter Mater. Phys. 76 (2007) 1–4. https://doi.org/10.1103/PhysRevB.76.172105.

[4] H. Schmid, Some symmetry aspects of ferroics and single phase multiferroics, J. Phys. Condens. Matter. 20 (2008) 1–24. https://doi.org/10.1088/0953-8984/20/43/434201.

[5] J. Ma, J. Hu, Z. Li, C.W. Nan, Recent progress in multiferroic magnetoelectric composites: From bulk to thin films, Adv. Mater. 23 (2011) 1062–1087. https://doi.org/10.1002/adma.201003636.

[6] B. Deka, S. Ravi, A. Perumal, D. Pamu, Ferromagnetism and ferroelectricity in Fe doped $BaTiO_3$, Phys. B Condens. Matter. 448 (2014) 204–206. https://doi.org/10.1016/j.physb.2014.03.069.

[7] Z. Chu, M. Pourhosseiniasl, S. Dong, Review of multi-layered magnetoelectric composite materials and devices applications, J. Phys. D. Appl. Phys. 51 (2018) 1–21. https://doi.org/10.1088/1361-6463/aac29b.

[8] C.W. Nan, M.I. Bichurin, S. Dong, D. Viehland, G. Srinivasan, Multiferroic magnetoelectric composites: Historical perspective, status, and future directions, J. Appl. Phys. 103 (2008) 1–35. https://doi.org/10.1063/1.2836410.

[9] A.J. Dos santos-García, E. Solana-Madruga, C. Ritter, A. Andrada-Chacón, J. Sánchez-Benítez, F.J. Mompean, M. Garcia-Hernandez, R. Sáez-Puche, R. Schmidt, Large Magnetoelectric Coupling Near Room Temperature in Synthetic Melanostibite Mn_2FeSbO_6, Angew. Chemie - Int. Ed. 56 (2017) 4438–4442. https://doi.org/10.1002/anie.201609762.

[10] J. Ryu, S. Priya, K. Uchino, H. Kim, Magnetoelectric Effect in Composites of Magnetostrictive and Piezoelectric Materials, J. Electroceramics. 8 (2002) 107–119. https://doi.org/10.1023/A:1020599728432.

[11] H. Trivedi, V. V. Shvartsman, D.C. Lupascu, M.S.A. Medeiros, R.C. Pullar, Stress

induced magnetic-domain evolution in magnetoelectric composites, Nanotechnology. 29 (2018) 1–9. https://doi.org/10.1088/1361-6528/aab181.

[12] Y. Wang, J. Li, D. Viehland, Magnetoelectrics for magnetic sensor applications: Status, challenges and perspectives, Mater. Today. 17 (2014) 269–275. https://doi.org/10.1016/j.mattod.2014.05.004.

[13] W.P. Wang, H. Yang, T. Xian, R.C. Yu, Observation of abnormal magnetoelectric behavior in 0-3 type $CoFe2O_4$-$BaTiO_3$ nanocomposites, Chem. Phys. Lett. 618 (2015) 72–77. https://doi.org/10.1016/j.cplett.2014.10.068.

[14] M. Islam, S. Adhikari, S. Pramanick, S. Chatterjee, A. Karmakar, Remarkable effects of dopant valency – a comparative study of $CaBaCo_{3.96}Cr_{0.04}O_7$ and $CaBaCo_{3.96}Ni_{0.04}O_7$, J. Magn. Magn. Mater. 529 (2021) 1–7. https://doi.org/10.1016/j.jmmm.2021.167847.

[15] V. Annapureddy, S.M. Na, G.T. Hwang, M.G. Kang, R. Sriramdas, H. Palneedi, W.H. Yoon, B.D. Hahn, J.W. Kim, C.W. Ahn, D.S. Park, J.J. Choi, D.Y. Jeong, A.B. Flatau, M. Peddigari, S. Priya, K.H. Kim, J. Ryu, Exceeding milli-watt powering magneto-mechano-electric generator for standalone-powered electronics, Energy Environ. Sci. 11 (2018) 818–829. https://doi.org/10.1039/c7ee03429f.

[16] W. Eerenstein, N.D. Mathur, J.F. Scott, Multiferroic and magnetoelectric materials, Nature. 442 (2006) 759–765. https://doi.org/10.1038/nature05023.

[17] X. Ren, Large electric-field-induced strain in ferroelectric crystals by point-defect-mediated reversible domain switching, Nat. Mater. 3 (2004) 91–94. https://doi.org/10.1038/nmat1051.

[18] T.R. Shrout, S.J. Zhang, Lead-free piezoelectric ceramics: Alternatives for PZT?, J. Electroceramics. 19 (2007) 111–124. https://doi.org/10.1007/s10832-007-9047-0.

[19] I.H. Lone, J. Aslam, N.R.E. Radwan, A.H. Bashal, A.F.A. Ajlouni, A. Akhter, Multiferroic ABO_3 Transition Metal Oxides: a Rare Interaction of Ferroelectricity and Magnetism, Nanoscale Res. Lett. 14 (2019) 1–12. https://doi.org/10.1186/s11671-019-2961-7.

[20] A. García-Arribas, Magnetostrictive Materials, MRS Bull. (1993) 34–41. https://doi.org/10.1007/978-3-030-70443-8_24.

[21] A.G. Olabi, A. Grunwald, Design and application of magnetostrictive materials, Mater. Des. 29 (2008) 469–483. https://doi.org/10.1016/j.matdes.2006.12.016.

[22] C.S. Schneider, Anisotropic cooperative theory of coaxial ferromagnetoelasticity, Phys. B Condens. Matter. 343 (2004) 65–74. https://doi.org/10.1016/j.physb.2003.08.040.

[23] J.M.D. Coey, History of Magnetism and Basic Concepts, in: Handb. Magn. Magn. Mater., Springer International Publishing, Cham, (2021) 1–49. https://doi.org/10.1007/978-3-030-63101-7_1-1.

[24] J. Atulasimha, A.B. Flatau, A review of magnetostrictive iron-gallium alloys, Smart Mater. Struct. 20 (2011) 1–15. https://doi.org/10.1088/0964-1726/20/4/043001.

[25] J.D. Verhoeven, E.D. Gibson, O.D. Mcmasters, J.E. Ostenson, Directional Solidification and Heat Treatment of TerfenoI-D Magnetostrictive Materials, 21 (1990) 2249–2255. https://doi.org/10.1007/BF02647887.

[26] R.W. Grimes, A.B. Anderson, A.H. Heuerg, Predictions of Cation Distributions in AB_2O_4 Spinels from Normalized Ion Energies, J. Am. Chem. Soc. 111 (1989) 1–7. https://doi.org/10.1021/ja00183a001.

[27] A.K. Das, R. Govindaraj, A. Srinivasan, Structural and magnetic properties of sol-gel derived $CaFe_2O_4$ nanoparticles, J. Magn. Magn. Mater. 451 (2018) 526–531. https://doi.org/10.1016/j.jmmm.2017.11.102.

[28] V.G. Harris, Societal Benefits of Ferrites, in: Mod. Ferrites, Wiley, 2022: pp. 9–20. https://doi.org/10.1002/9781118971499.ch2.

[29] R. Guo, L.E. Cross, S.E. Park, B. Noheda, D.E. Cox, G. Shirane, Origin of the high piezoelectric response in $PbZr_{1-x}Ti_xO_3$, Phys. Rev. Lett. 84 (2000) 5423–5426. https://doi.org/10.1103/PhysRevLett.84.5423.

[30] S. Gao, Functional-Material-Based Touch Interfaces for Multidimensional Sensing for Interactive Displays: A Review, Semicond. Sci. Inf. Devices. 1 (2019) 14–27. https://doi.org/10.30564/ssid.v1i1.1171.

[31] Y. Si, Y. Li, L. Li, H. Li, Z. Zhao, Y. Dai, Giant electro-strain in textured Li^+-doped 0.852BNT–0.11BKT–0.038BT ternary lead-free piezoelectric ceramics, J. Am. Ceram. Soc. 103 (2020) 1765–1772. https://doi.org/10.1111/jace.16853.

[32] P. Singh, R. Laishram, P. Sharma, J. Kolte, Giant magnetocapacitance in magnetoelectric BNT/NFO particulate composites, J. Mater. Sci. Mater. Electron. 32 (2021) 21288–21296. https://doi.org/10.1007/s10854-021-06631-w.

[33] M. Tyagi, M. Kumari, R. Chatterjee, P. Sharma, Large magnetoelectric response in modified BNT based ternary piezoelectric [$72.5(Bi_{1/2}Na_{1/2}TiO_3$)-$22.5(Bi_{1/2}K_{1/2}TiO_3$)-$5(BiMg_{1/2}Ti_{1/2}O_3$)]-magnetostrictive ($NiFe_2O_4$) particulate (0-3) composites, Appl. Phys. Lett. 106 (2015) 1–4. https://doi.org/10.1063/1.4921521.

[34] X. Tan, C. Ma, J. Frederick, S. Beckman, K.G. Webber, The antiferroelectric ↔

ferroelectric phase transition in lead-containing and lead-free perovskite ceramics, J. Am. Ceram. Soc. 94 (2011) 4091–4107. https://doi.org/10.1111/j.1551-2916.2011.04917.x.

[35] G. Jones, P.A. Thomas, Investigation of the structure and phase transitions in the novel A-site substituted distorted perovskite compound $Na_{0.5}Bi_{0.5}TiO_3$, Acta Crystallogr. Sect. B. 58 (2002) 168–178. https://doi.org/10.1107/S0108768101020845.

[36] S. Dash, D.K. Pradhan, S. Kumari, Ravikant, M.M. Rahaman, C. Cazorla, K. Brajesh, A. Kumar, R. Thomas, P.D. Rack, D.K. Pradhan, Enhanced ferroelectric and piezoelectric properties of BCT-BZT at the morphotropic phase boundary driven by the coexistence of phases with different symmetries, Phys. Rev. B. 104 (2021) 1–18. https://doi.org/10.1103/PhysRevB.104.224105.

[37] Q. Wang, J. Chen, L. Fan, H. Song, W. Gao, Y. Rong, L. Liu, L. Fang, X. Xing, Preparation and electric properties of $Bi_{0.5}Na_{0.5}TiO_3$-$Bi(Al_{0.5}Ga_{0.5})O_3$ lead-free piezoceramics, J. Am. Ceram. Soc. 96 (2013) 3793–3797. https://doi.org/10.1111/jace.12588.

[38] L. Jiao, F.F. Guo, J.F. Wang, Z. Bin Gu, S.T. Zhang, B. Yang, Morphotropic phase boundary and electric properties in (1-x)$Bi_{0.5}Na_{0.5}TiO_3$-x$BaSnO_3$ lead-free piezoelectric ceramics, J. Mater. Sci. Mater. Electron. 24 (2013) 4080–4084. https://doi.org/10.1007/s10854-013-1364-2.

[39] C. Zhou, X. Liu, Dielectric and piezoelectric properties of bismuth-containing complex perovskite solid solution of $Bi_{1/2}Na_{1/2}TiO_3$-$Bi(Mg_{2/3}Nb_{1/3})O_3$, J. Mater. Sci. 43 (2008) 1016–1019. https://doi.org/10.1007/s10853-007-2246-x.

[40] A. Ullah, M. Ishfaq, C. Won Ahn, A. Ullah, S. Ehsan Awan, I. Won Kim, Relaxor behavior and piezoelectric properties of $Bi(Mg_{0.5}Ti_{0.5})O_3$-modified $Bi_{0.5}Na_{0.5}TiO_3$ lead-free ceramics, Ceram. Int. 41 (2015) 10557–10564. https://doi.org/10.1016/j.ceramint.2015.04.150.

[41] J.U. Rahman, A. Hussain, A. Maqbool, T.K. Song, W.J. Kim, S.S. Kim, M.H. Kim, Dielectric, ferroelectric and field-induced strain response of lead-free $BaZrO_3$-modified $Bi_{0.5}Na_{0.5}TiO_3$ ceramics, Curr. Appl. Phys. 14 (2014) 331–336. https://doi.org/10.1016/j.cap.2013.12.009.

[42] T. Chen, T. Zhang, G. Wang, J. Zhou, J. Zhang, Y. Liu, Effect of $Li_{0.12}Na_{0.88}NbO_3$ content on the electrical properties of $Bi_{0.50}Na_{0.50}TiO_3$ lead-free piezoelectric ceramics, J. Alloys Compd. 520 (2012) 7–10. https://doi.org/10.1016/j.jallcom.2012.01.014.

[43] Y. Hiruma, H. Nagata, T. Takenaka, Detection of morphotropic phase boundary of $(Bi_{1/2}Na_{1/2})TiO_3$-$Ba(Al_{1/2}Sb_{1/2})O_3$ solid-solution ceramics, Appl. Phys. Lett. 95 (2009) 4–7. https://doi.org/10.1063/1.3194146.

[44] D. Lin, C. Xu, Q. Zheng, Y. Wei, D. Gao, Piezoelectric and dielectric properties of $Bi_{0.5}Na_{0.5}TiO_3$-$Bi_{0.5}Li_{0.5}TiO_3$ lead-free ceramics, J. Mater. Sci. Mater. Electron. 20 (2009) 393–397. https://doi.org/10.1007/s10854-008-9741-y.

[45] F. Li, R. Zuo, D. Zheng, L. Li, Phase-composition-dependent piezoelectric and electromechanical strain properties in $(Bi_{1/2}Na_{1/2})TiO_3$-$Ba(Ni_{1/2}Nb_{1/2})O_3$ lead-free ceramics, J. Am. Ceram. Soc. 98 (2015) 811–818. https://doi.org/10.1111/jace.13363.

[46] W. Bai, Y. Bian, J. Hao, B. Shen, J. Zhai, The composition and temperature-dependent structure evolution and large strain response in $(1-x)(Bi_{0.5}Na_{0.5})TiO_3$-$xBa(Al_{0.5}Ta_{0.5})O_3$ ceramics, J. Am. Ceram. Soc. 96 (2013) 246–252. https://doi.org/10.1111/jace.12039.

[47] L. Wang, C. Zhang, W.J. Ji, S.T. Zhang, Y.F. Chen, Morphotropic phase boundary in $(1-x)Bi_{0.5}Na_{0.5}TiO_3$-$x(Bi_{0.8}La_{0.2})FeO_3$ with improved depolarization temperature, Phys. Status Solidi - Rapid Res. Lett. 3 (2009) 245–247. https://doi.org/10.1002/pssr.200903189.

[48] H. Yu, Z.G. Ye, Dielectric, ferroelectric, and piezoelectric properties of the lead-free $(1-x)$ $(Na_{0.5}Bi_{0.5})TiO_3$-$xBiAlO_3$ solid solution, Appl. Phys. Lett. 93 (2008) 3–6. https://doi.org/10.1063/1.2967335.

[49] B. Parija, T. Badapanda, S. Panigrahi, Morphotropic phase boundary in BNT-BZT solid solution: A study by raman spectroscopy and electromechanical parameters, J. Ceram. Process. Res. 16 (2015) 565–571.

[50] Y. Hiruma, H. Nagata, T. Takenaka, Formation of morphotropic phase boundary and electrical properties of $(Bi_{1/2}Na_{1/2})TiO_3$-$Ba(Al_{1/2}Nb_{1/2})O_3$ solid solution ceramics, Jpn. J. Appl. Phys. 48 (2009). https://doi.org/10.1143/JJAP.48.09KC08.

[51] B. Parija, T. Badapanda, S. Panigrahi, T.P. Sinha, Ferroelectric and piezoelectric properties of $(1-x)(Bi_{0.5}Na_{0.5})TiO_3$-$xBaTiO_3$ ceramics, J. Mater. Sci. Mater. Electron. 24 (2013) 402–410. https://doi.org/10.1007/s10854-012-0764-z.

[52] Z. Yang, B. Liu, L. Wei, Y. Hou, Structure and electrical properties of $(1-x)Bi_{0.5}Na_{0.5}TiO_3$-$xBi_{0.5}K_{0.5}TiO_3$ ceramics near morphotropic phase boundary, Mater. Res. Bull. 43 (2008) 81–89. https://doi.org/10.1016/j.materresbull.2007.02.016.

[53] H. Lidjici, B. Lagoun, M. Berrahal, M. Rguitti, M.A. Hentatti, H. Khemakhem, XRD, Raman and electrical studies on the $(1-x)(Na_{0.5}Bi_{0.5})TiO_3$-$xBaTiO_3$lead free ceramics, J.

Alloys Compd. 618 (2015) 643–648. https://doi.org/10.1016/j.jallcom.2014.08.161.

[54] Y. Hiruma, H. Nagata, T. Takenaka, Phase diagrams and electrical properties of $(Bi_{0.5}Na_{0.5})TiO_3$-based solid solutions, J. Appl. Phys. 104 (2008) 1–7. https://doi.org/10.1063/1.3043588.

[55] C. Xu, D. Lin, K.W. Kwok, Structure, electrical properties and depolarization temperature of $(Bi_{0.5}Na_{0.5})TiO_3$-$BaTiO_3$ lead-free piezoelectric ceramics, Solid State Sci. 10 (2008) 934–940. https://doi.org/10.1016/j.solidstatesciences.2007.11.003.

[56] K. Yoshii, Y. Hiruma, H. Nagata, T. Takenaka, Electrical properties and depolarization temperature of $(Bi_{1/2}Na_{1/2})TiO_3$-$(Bi_{1/2}K_{1/2})TiO_3$ lead-free piezoelectric ceramics, Japanese J. Appl. Physics, Part 1 Regul. Pap. Short Notes Rev. Pap. 45 (2006) 4493–4496. https://doi.org/10.1143/JJAP.45.4493.

[57] G. Hernandez-Cuevas, J.R. Leyva Mendoza, P.E. García-Casillas, C.A. Rodríguez González, J.F. Hernandez-Paz, G. Herrera-Pérez, L. Fuentes-Cobas, S. Díaz de la Torre, O. Raymond-Herrera, H. Camacho-Montes, Effect of the sintering technique on the ferroelectric and d33 piezoelectric coefficients of $Bi_{0.5}(Na_{0.84}K_{0.16})_{0.5}TiO_3$ ceramic, J. Adv. Ceram. 8 (2019) 278–288. https://doi.org/10.1007/s40145-019-0314-8.

[58] Y. Li, W. Chen, Q. Xu, J. Zhou, Y. Wang, H. Sun, Piezoelectric and dielectric properties of CeO_2-doped $Bi_{0.5}Na_{0.44}K_{0.06}TiO_3$ lead-free ceramics, Ceram. Int. 33 (2007) 95–99. https://doi.org/10.1016/j.ceramint.2005.08.001.

[59] H.Y. Tian, D.Y. Wang, D.M. Lin, J.T. Zeng, K.W. Kwok, H.L.W. Chan, Diffusion phase transition and dielectric characteristics of $Bi_{0.5}Na_{0.5}TiO_3$-$Ba(Hf,Ti)O_3$ lead-free ceramics, Solid State Commun. 142 (2007) 10–14. https://doi.org/10.1016/j.ssc.2007.01.043.

[60] P. Fu, Z. Xu, R. Chu, X. Wu, W. Li, H. Zhang, Structure and electrical properties of the Ho_2O_3 doped $0.82Bi_{0.5}Na_{0.5}TiO_3$-$0.18Bi_{0.5}K_{0.5}TiO_3$ lead-free piezoelectric ceramics, J. Mater. Sci. Mater. Electron. 23 (2012) 2167–2172. https://doi.org/10.1007/s10854-012-0734-5.

[61] P. Fu, Z. Xu, H. Zhang, R. Chu, W. Li, M. Zhao, Structure and electrical properties of Er_2O_3 doped $0.82Bi_{0.5}Na_{0.5}TiO_3$-$0.18Bi_{0.5}K_{0.5}TiO_3$ lead-free piezoelectric ceramics, Mater. Des. 40 (2012) 373–377. https://doi.org/10.1016/j.matdes.2012.04.020.

[62] C. Zhi-Hui, D. Jian-Ning, M. Lin, Y. Ning-Yi, Z. Wei-Wei, Piezoelectric and dielectric properties of Dy_2O_3-Doped $Bi_{0.5}(Na_{0.82}K_{0.18})_{0.5}TiO_3$ lead-free ceramics, Ferroelectrics. 425 (2011) 63–71. https://doi.org/10.1080/00150193.2011.634752.

[63] X.Y. Zhou, H.S. Gu, Y. Wang, W.Y. Li, T.S. Zhou, Piezoelectric properties of Mn-doped $(Na_{0.5}Bi_{0.5})_{0.92}Ba_{0.08}TiO_3$ ceramics, Mater. Lett. 59 (2005) 1649–1652. https://doi.org/10.1016/j.matlet.2005.01.034.

[64] W.C. Lee, C.Y. Huang, L.K. Tsao, Y.C. Wu, Chemical composition and tolerance factor at the morphotropic phase boundary in $(Bi_{0.5}Na_{0.5})$TiO3-based piezoelectric ceramics, J. Eur. Ceram. Soc. 29 (2009) 1443–1448. https://doi.org/10.1016/j.jeurceramsoc.2008.08.028.

[65] J.Q. Hu, Z.W. Chen, Piezoelectric and Dielectric Properties of Bi_2O_3-Doped $(Bi_{0.5}Na_{0.5})_{0.94}Ba_{0.06}TiO_3$ Lead-Free Piezoelectric Ceramics, Key Eng. Mater. 368–372 (2008) 1915–1918. https://doi.org/10.4028/www.scientific.net/kem.368-372.1915.

[66] C. Zhi-Hui, D. Jian-Ning, M. Lin, Y. Ning-Yi, Z. Yuan-Yuan, Piezoelectric and dielectric properties of Dy_2O_3-doped $(Bi_{0.5}Na_{0.5})_{0.94}Ba_{0.06}TiO_3$ lead-free ceramics, J. Alloys Compd. 509 (2011) 482–485. https://doi.org/10.1016/j.jallcom.2010.09.070.

[67] B. Wu, D. Xiao, W. Wu, J. Zhu, Q. Chen, J. Wu, Microstructure and electrical properties of $(Ba_{0.98}Ca_{0.02})(Ti_{0.94}Sn_{0.06})O_3$-modified $Bi_{0.5}Na_{0.5}TiO_3$ lead-free ceramics, Ceram. Int. 38 (2012) 5677–5681. https://doi.org/10.1016/j.ceramint.2012.04.011.

[68] W.H. Han, J.H. Koh, Shrinkage mechanism and enhanced piezoelectric properties of Ta doped 0.94 $Bi_{0.5}Na_{0.5}TiO_3$–0.06$BaTiO_3$ lead free ceramics, Ceram. Int. 44 (2018) 5352–5358. https://doi.org/10.1016/j.ceramint.2017.12.155.

[69] X. Zhang, G. Jiang, F. Guo, D. Liu, S. Zhang, B. Yang, W. Cao, Mn doping effects on electric properties of 0.93$(Bi_{0.5}Na_{0.5})TiO_3$-0.07$Ba(Ti_{0.945}Zr_{0.055})O_3$ ceramics, J. Am. Ceram. Soc. 101 (2018) 2996–3004. https://doi.org/10.1111/jace.15457.

[70] P. Fu, Z. Xu, R. Chu, W. Li, G. Zang, J. Hao, Piezoelectric, ferroelectric and dielectric properties of Nd_2O_3-doped $(Bi_{0.5}Na_{0.5})$0.94$Ba_{0.06}TiO_3$ lead-free ceramics, Mater. Sci. Eng. B Solid-State Mater. Adv. Technol. 167 (2010) 161–166. https://doi.org/10.1016/j.mseb.2010.01.057.

[71] Q. Xu, D.P. Huang, M. Chen, W. Chen, H.X. Liu, B.H. Kim, Effect of bismuth excess on ferroelectric and piezoelectric properties of a $(Na_{0.5}Bi_{0.5})TiO_3$-$BaTiO_3$ composition near the morphotropic phase boundary, J. Alloys Compd. 471 (2009) 310–316. https://doi.org/10.1016/j.jallcom.2008.03.078.

[72] M.S. Yoon, Y.G. Lee, S.C. Ur, Effects of co-doped CaO/MnO on the piezoelectric/dielectric properties and phase transition of lead-Free $(Bi_{0.5}Na_{0.5})$ 0.94$Ba_{0.06}TiO_3$ piezoelectric ceramics, J. Electroceramics. 23 (2009) 564–571.

https://doi.org/10.1007/s10832-008-9548-5.

[73] Y. Liao, D. Xiao, D. Lin, J. Zhu, P. Yu, L. Wu, X. Wang, Synthesis and properties of $Bi_{0.5}(Na_{1-x-y}K_xAg_y)_{0.5}TiO_3$ lead-free piezoelectric ceramics, Ceram. Int. 33 (2007) 1445–1448. https://doi.org/10.1016/j.ceramint.2006.05.004.

[74] C. Zhou, X. Liu, W. Li, Dielectric and piezoelectric properties of $BiFeO_3$ modified B $Bi_{0.5}Na_{0.5}TiO_3$-$Bi_{0.5}K_{0.5}TiO_3$ lead-free piezoelectric ceramics, Mater. Sci. Eng. B Solid-State Mater. Adv. Technol. 153 (2008) 31–35. https://doi.org/10.1016/j.mseb.2008.09.032.

[75] L. Wu, D. Xiao, F. Zhou, Y. Teng, Y. Li, Microstructure, ferroelectric, and piezoelectric properties of (1-x-y)$Bi_{0.5}Na_{0.5}TiO_3$-x$BaTiO_3$-y$Bi_{0.5}Ag_{0.5}TiO_3$ lead-free ceramics, J. Alloys Compd. 509 (2011) 466–470. https://doi.org/10.1016/j.jallcom.2010.09.062.

[76] Y. Hiruma, H. Nagata, T. Takenaka, Depolarization temperature and piezoelectric properties of $(Bi_{1/2}Na_{1/2})TiO_3$-$(Bi_{1/2}Li_{1/2})TiO_3$-$(Bi_{1/2}K_{1/2})TiO_3$ lead-free piezoelectric ceramics, Ceram. Int. 35 (2009) 117–120. https://doi.org/10.1016/j.ceramint.2007.10.023.

[77] X.Y. Wang, C.L. Wang, M.L. Zhao, J.F. Wang, K. Yang, J.C. Li, Ferroelectric properties of lithia-doped $(Bi_{0.95}Na_{0.75}K_{0.20})_{0.5}Ba_{0.05}TiO_3$ ceramics, Mater. Lett. 61 (2007) 3847–3850. https://doi.org/10.1016/j.matlet.2006.12.045.

[78] C. Zhou, X. Liu, W. Li, C. Yuan, Microstructure and electrical properties of B $Bi_{0.5}Na_{0.5}TiO_3$-$Bi_{0.5}K_{0.5}TiO_3$-$LiNbO_3$ lead-free piezoelectric ceramics, J. Phys. Chem. Solids. 70 (2009) 541–545. https://doi.org/10.1016/j.jpcs.2008.12.013.

[79] D. Lin, K.W. Kwok, H.L.W. Chan, Structure and electrical properties of $Bi_{0.5}Na_{0.5}TiO_3$-$BaTiO_3$-$Bi_{0.5}Li_{0.5}TiO_3$ lead-free piezoelectric ceramics, Solid State Ionics. 178 (2008) 1930–1937. https://doi.org/10.1016/j.ssi.2007.12.096.

[80] G. Fan, W. Lu, X. Wang, F. Liang, Morphotropic phase boundary and piezoelectric properties of $(Bi_{1/2}Na_{1/2})TiO_3$-$(Bi_{1/2}K_{1/2})TiO_3$ -$KNbO_3$ lead-free piezoelectric ceramics, Appl. Phys. Lett. 91 (2007) 3–6. https://doi.org/10.1063/1.2815918.

[81] M. Tyagi, P. Sharma, M. Kumari, M. Thakur, Improved magnetoelectric effect in lead free [72.5$(Bi_{1/2}Na_{1/2}TiO_3)$–22.5$(Bi_{1/2}K_{1/2}TiO_3)$–5$(BiMg_{1/2}Ti_{1/2}O_3)$]:$CoFe_2O_4$ particulate nanocomposites prepared by sol–gel method, J. Mater. Sci. Mater. Electron. 28 (2017) 2812–2816. https://doi.org/10.1007/s10854-016-5862-x.

[82] P. Jarupoom, E. Patterson, B. Gibbons, G. Rujijanagul, R. Yimnirun, D. Cann, Lead-free ternary perovskite compounds with large electromechanical strains, Appl. Phys.

Lett. 99 (2011) 1–4. https://doi.org/10.1063/1.3647627.

[83] M. Bichurin, V. Petrov, A. Zakharov, D. Kovalenko, S.C. Yang, D. Maurya, V. Bedekar, S. Priya, Magnetoelectric interactions in lead-based and lead-free composites, Materials (Basel). 4 (2010) 651–702. https://doi.org/10.3390/ma4040651.

[84] S.D. Bhame, P.A. Joy, Tuning of the magnetostrictive properties of $CoFe_2O_4$ by Mn substitution for Co, J. Appl. Phys. 100 (2006) 1-4. https://doi.org/10.1063/1.2401648.

[85] M. Atif, M. Nadeem, R. Grössinger, R.S. Turtelli, Studies on the magnetic, magnetostrictive and electrical properties of sol-gel synthesized Zn doped nickel ferrite, J. Alloys Compd. 509 (2011) 5720–5724. https://doi.org/10.1016/j.jallcom.2011.02.163.

[86] S.A. Mazen, N.I. Abu-Elsaad, A.E. Khadour, A comparative study of the structural and magnetic properties for Zn^{2+} and Ge^{4+} ions substituted nickel ferrites, J. Magn. Magn. Mater. 491 (2019) 165562. https://doi.org/10.1016/j.jmmm.2019.165562.

[87] M.M.L. Sonia, S. Anand, V.M. Vinosel, M. Asisi Janifer, S. Pauline, Effect of lattice strain on structural, magnetic and dielectric properties of sol–gel synthesized nanocrystalline Ce^{3+} substituted nickel ferrite, J. Mater. Sci. Mater. Electron. 29 (2018) 15006–15021. https://doi.org/10.1007/s10854-018-9639-2.

[88] M.A. Gabal, Y.M.A. Angari, Effect of chromium ion substitution on the electromagnetic properties of nickel ferrite, Mater. Chem. Phys. 118 (2009) 153–160. https://doi.org/10.1016/j.matchemphys.2009.07.025.

[89] S.M. Patange, S.E. Shirsath, B.G. Toksha, S.S. Jadhav, S.J. Shukla, K.M. Jadhav, Cation distribution by Rietveld, spectral and magnetic studies of chromium-substituted nickel ferrites, Appl. Phys. A Mater. Sci. Process. 95 (2009) 429–434. https://doi.org/10.1007/s00339-008-4897-0.

[90] Y. Sandeep, T. Rambabu, L. Kunja, O. Borang, G. Aravind, A. Dode, V. Nathanial, Low sintering effect on structural, electrical and magnetic properties of rare-earth metal ion Er^{3+}-substituted nickel–zinc spinal ferrites, J. Mater. Sci. Mater. Electron. 33 (2022) 635–651. https://doi.org/10.1007/s10854-021-07332-0.

[91] M.M.L. Sonia, S. Anand, V.M. Vinosel, M.A. Janifer, S. Pauline, A. Manikandan, Effect of lattice strain on structure, morphology and magneto-dielectric properties of spinel $NiGd_xFe_{2-x}O_4$ ferrite nano-crystallites synthesized by sol-gel route, J. Magn. Magn. Mater. 466 (2018) 238–251. https://doi.org/10.1016/j.jmmm.2018.07.017.

[92] B.P. Jacob, S. Thankachan, S. Xavier, E.M. Mohammed, Effect of Tb^{3+} substitution on

structural, electrical and magnetic properties of sol-gel synthesized nanocrystalline nickel ferrite, J. Alloys Compd. 578 (2013) 314–319. https://doi.org/10.1016/j.jallcom.2013.04.147.

[93] S. Kamali, Spin structure, magnetism, and cation distributions of $NiFe_{2-x}Al_xO_4$ solid solutions, J. Magn. Magn. Mater. 433 (2017) 155–161. https://doi.org/10.1016/j.jmmm.2017.03.010.

[94] Z.K. Heiba, M.B. Mohamed, A.M. Wahba, M.I. Almalowi, Effect of vanadium doping on structural and magnetic properties of defective nano-nickel ferrite, Appl. Phys. A Mater. Sci. Process. 124 (2018) 1–9. https://doi.org/10.1007/s00339-018-1721-3.

[95] T.J. Shinde, A.B. Gadkari, P.N. Vasambekar, Influence of Nd^{3+} substitution on structural, electrical and magnetic properties of nanocrystalline nickel ferrites, J. Alloys Compd. 513 (2012) 80–85. https://doi.org/10.1016/j.jallcom.2011.10.001.

[96] M.A. Almessiere, Y. Slimani, S. Güner, A. Baykal, I. Ercan, Effect of dysprosium substitution on magnetic and structural properties of $NiFe_2O_4$ nanoparticles, J. Rare Earths. 37 (2019) 871–878. https://doi.org/10.1016/j.jre.2018.10.009.

[97] S.E. Shirsath, B.G. Toksha, K.M. Jadhav, Structural and magnetic properties of In3+ substituted $NiFe_2O_4$, Mater. Chem. Phys. 117 (2009) 163–168. https://doi.org/10.1016/j.matchemphys.2009.05.027.

[98] J. Balavijayalakshmi, N. Suriyanarayanan, R. Jayaprakash, Role of copper on structural, magnetic and dielectric properties of nickel ferrite nano particles, J. Magn. Magn. Mater. 385 (2015) 302–307. https://doi.org/10.1016/j.jmmm.2015.03.036.

[99] S.S. Thomas, B. Jacob, M. Mohan, K.C. Dhanyaprabha, I.A. Al-Omari, S.H. Al-Harthi, M.T.Z. Myint, H. Thomas, Study on the microstructural and magnetic properties of nickel - Calcium ferrites, Phys. Scr. 97 (2022). https://doi.org/10.1088/1402-4896/ac5d71.

[100] M. Rahimi, M. Eshraghi, P. Kameli, Structural and magnetic characterizations of Cd substituted nickel ferrite nanoparticles, Ceram. Int. 40 (2014) 15569–15575. https://doi.org/10.1016/j.ceramint.2014.07.033.

[101] Y. Slimani, M.A. Almessiere, M. Nawaz, A. Baykal, S. Akhtar, I. Ercan, I. Belenli, Effect of bimetallic (Ca, Mg) substitution on magneto-optical properties of $NiFe_2O_4$ nanoparticles, Ceram. Int. 45 (2019) 6021–6029. https://doi.org/10.1016/j.ceramint.2018.12.072.

[102] K.P. Chae, W.O. Choi, J.G. Lee, B.S. Kang, S.H. Choi, Crystallographic and magnetic

properties of Nickel substituted manganese ferrites synthesized by sol-gel method, J. Magn. 18 (2013) 21–25. https://doi.org/10.4283/JMAG.2013.18.1.021.

[103] P. Chavan, L.R. Naik, P.B. Belavi, G. Chavan, C.K. Ramesha, R.K. Kotnala, Studies on Electrical and Magnetic Properties of Mg-Substituted Nickel Ferrites, J. Electron. Mater. 46 (2017) 188–198. https://doi.org/10.1007/s11664-016-4886-6.

[104] M.K. Anupama, N. Srinatha, S. Matteppanavar, B. Angadi, B. Sahoo, B. Rudraswamy, Effect of Zn substitution on the structural and magnetic properties of nanocrystalline $NiFe_2O_4$ ferrites, Ceram. Int. 44 (2018) 4946–4954. https://doi.org/10.1016/j.ceramint.2017.12.087.

[105] S.K. Mandal, G. Sreenivasulu, V.M. Petrov, G. Srinivasan, Flexural deformation in a compositionally stepped ferrite and magnetoelectric effects in a composite with piezoelectrics, Appl. Phys. Lett. 96 (2010) 1–3. https://doi.org/10.1063/1.3428774.

[106] R. V. Krishnaiah, A. Srinivas, S. V. Kamat, T. Karthik, S. Asthana, Effect of $CoFe_2O_4$ mole percentage on multiferroic and magnetoelectric properties of $Na_{0.5}Bi_{0.5}TiO_3/CoFe_2O_4$ particulate composites, Ceram. Int. 40 (2014) 7799–7804. https://doi.org/10.1016/j.ceramint.2013.12.123.

[107] S. Dagar, A. Hooda, S. Khasa, M. Malik, Structural refinement, investigation of dielectric and magnetic properties of NBT doped $BaFe_{12}O_{19}$ novel composite system, J. Alloys Compd. 826 (2020) 154214. https://doi.org/10.1016/j.jallcom.2020.154214.

[108] P. Singh, R. Laishram, J. Kolte, P. Sharma, Low Frequency Magnetoelectric Effect in $Bi_{0.5}Na_{0.5}TiO_3$–$Ni_{0.5}Zn_{0.5}Fe_2O_4$ Particulate Composites, Electron. Mater. Lett. 19 (2023) 442–451. https://doi.org/10.1007/s13391-023-00423-6.

[109] Manjusha, K.L. Yadav, N. Adhlakha, J. Shah, R.K. Kotnala, Strain mediated magnetoelectric coupling induced in (x) $Bi_{0.5}Na_{0.5}TiO_3$-(1−x)$MgFe_2O_4$ composites, Phys. B Condens. Matter. 514 (2017) 41–50. https://doi.org/10.1016/j.physb.2017.03.027.

[110] C. Kornphom, K. Saenkam, P. Jantaratana, S. Pinitsoontorn, T. Bongkarn, Investigations on the Multiferroic Properties of Lead Free BNT-BCTS:MFO Ceramic Composites Fabricated by the Solid-State Combustion Technique, Jom. 75 (2023) 2669–2683. https://doi.org/10.1007/s11837-023-05835-1.

[111] M. Thakur, P. Sharma, M. Kumari, A.P. Singh, M. Tyagi, Magnetoelectric effect in lead free piezoelectric $Bi_{1/2}Na_{1/2}TiO_3$–modified CFO based magnetostrictive ($Co_{0.6}Zn_{0.4}Fe_{1.7}Mn_{0.3}O_4$) particulate nanocomposite prepared by sol-gel method, J.

Magn. Magn. Mater. 426 (2017) 753–756. https://doi.org/10.1016/j.jmmm.2016.10.130.

[112] Y. Kumar, K.L. Yadav, J. Shah, R.K. Kotnala, Investigation of magnetoelectric effect in $Bi_{0.5}Na_{0.5}TiO_3$-$CoMn_{0.2}Fe_{1.8}O_4$ composites, IEEE Trans. Dielectr. Electr. Insul. 26 (2019) 561–567. https://doi.org/10.1109/TDEI.2019.007577.

[113] Y. Kumar, K.L. Yadav, Manjusha, J. Shah, R.K. Kotnala, Structural, dielectric, magnetic and magnetoelectric properties of (x)$Bi_{0.5}Na_{0.5}TiO_3$-(1-x)$Ni_{0.2}Co_{0.8}Fe_2O_4$ composites, Mater. Res. Express. 3 (2016) 1–9. https://doi.org/10.1088/2053-1591/3/6/065701.

[114] E.V. Ramana, A. Mahajan, M.P.F. Graça, A. Srinivas, M.A. Valente, Ferroelectric and magnetic properties of magnetoelectric $(Na_{0.5}Bi_{0.5})TiO_3$-$BiFeO_3$ synthesized by acetic acid assisted sol-gel method, J. Eur. Ceram. Soc. 34 (2014) 4201–4211. https://doi.org/10.1016/j.jeurceramsoc.2014.06.027.

[115] S. Liu, L. Deng, S. Yan, H. Luo, L. Yao, L. He, Y. Li, M. Wu, S. Huang, Magnetoelectric properties of lead-free (80$Bi_{0.5}Na_{0.5}TiO_3$-20$Bi_{0.5}K_{0.5}TiO_3$)-$Ni_{0.8}Zn_{0.2}Fe_2O_4$ particulate composites prepared by in situ sol-gel, J. Appl. Phys. 122 (2017) 1–6. https://doi.org/10.1063/1.4994172.

[116] M. Tyagi, M. Kumari, R. Chatterjee, P. Sharma, Large magnetoelectric response in modified BNT based ternary piezoelectric [72.5($Bi_{1/2}Na_{1/2}TiO_3$)-22.5($Bi_{1/2}K_{1/2}TiO_3$)-5($BiMg_{1/2}Ti_{1/2}O_3$)]-magnetostrictive ($NiFe_2O_4$) particulate (0-3) composites, Appl. Phys. Lett. 106 (2015) 1–4. https://doi.org/10.1063/1.4921521.

[117] A.H. Pandey, P. Varade, K. Miriyala, N.S. Sowmya, A. Kumar, A. Arockiarajan, A.R. Kulkarni, N. Venkataramani, Magnetoelectric response in lead-free $Na_{0.4}K_{0.1}Bi_{0.5}TiO_3$/$NiFe_2O_4$ laminated composites, Mater. Today Commun. 26 (2021) 101898. https://doi.org/10.1016/j.mtcomm.2020.101898.

[118] S. Liu, S. Yan, H. Luo, L. Yao, Y. Li, J. He, L. He, S. Huang, L. Deng, Magnetoelectric Effect in Cofired Lead-Free Laminated ($Bi_{0.5}Na_{0.5}TiO_3$-$Bi_{0.5}K_{0.5}TiO_3$)/($Ni_{0.8}Zn_{0.2}$)Fe_2O_4 Composites, Phys. Status Solidi Appl. Mater. Sci. 214 (2017) 1–7. https://doi.org/10.1002/pssa.201700533.

[119] Q. Dai, K. Guo, M. Zhang, R. Cui, C. Deng, Magnetoelectric properties of $NiFe_2O_4$ /0.65$BaTiO_3$–0.35$Na_{0.5}Bi_{0.5}TiO_3$ bilayer thin films deposited via pulsed laser deposition, Ceram. Int. 45 (2019) 8448–8453. https://doi.org/10.1016/j.ceramint.2019.01.154.

[120] M. Kumari, A. Singh, A. Gupta, C. Prakash, R. Chatterjee, Self-biased large magnetoelectric coupling in co-sintered $Bi_{0.5}Na_{0.5}TiO_3$ based piezoelectric and $CoFe_2O_4$

based magnetostrictive bilayered composite, J. Appl. Phys. 116 (2014) 0–5. https://doi.org/10.1063/1.4904758.

[121] T.C. Darvade, P.S. Kadhane, B.G. Baraskar, A.R. James, V.R. Reddy, R.C. Kambale, Structural and multiferroic properties of trilayer green magnetoelectric $Co_{0.8}Ni_{0.2}Fe_2O_4/K_{0.25}Na_{0.75}NbO_3/Co_{0.8}Ni_{0.2}Fe_2O_4$ composite structure, J. Magn. Magn. Mater. 505 (2020) 166733. https://doi.org/10.1016/j.jmmm.2020.166733.

[122] J. Ryu, A.V. Carazo, K. Uchino, H.E. Kim, Magnetoelectric properties in piezoelectric and magnetostrictive laminate composites, Japanese J. Appl. Physics, Part 1 Regul. Pap. Short Notes Rev. Pap. 40 (2001) 4948–4951. https://doi.org/10.1143/jjap.40.4948.

[123] J. Ryu, S. Priya, A. Vázquez Carazo, K. Uchino, H.E. Kim, Effect of the Magnetostrictive Layer on Magnetoelectric Properties in Lead Zirconate Titanate/Terfenol-D Laminate Composites, J. Am. Ceram. Soc. 84 (2001) 2905–2908. https://doi.org/10.1111/j.1151-2916.2001.tb01113.x.

[124] S. Dinesh Kumar, J. Magesh, V. Subramanian, Temperature dependent magnetoelectric studies in co-fired bilayer laminate composites, J. Alloys Compd. 753 (2018) 595–600. https://doi.org/10.1016/j.jallcom.2018.04.275.

[125] R.A. Islam, S. Priya, Large magnetoelectric coefficient in Co-fired $Pb(Zr_{0.52}Ti_{0.48})O_3$-$Pb(Zn_{1/3}Nb_{2/3})O_3$-$Ni_{0.6}Cu_{0.2}Zn_{0.2}Fe_2O_4$ trilayer magnetoelectric composites, J. Mater. Sci. 43 (2008) 2072–2076. https://doi.org/10.1007/s10853-007-2442-8.

[126] S. Liu, S. Liao, H. Zou, B. Qin, L. Deng, Transition-Layer Implantation for Improving Magnetoelectric Response in Co-fired Laminated Composite, Magnetochemistry. 9 (2023) 1–11. https://doi.org/10.3390/magnetochemistry9020050.

[127] P. Praveen J, V.R. Monaji, S.D. Kumar, V. Subramanian, D. Das, Enhanced magnetoelectric response from lead-free $(Ba_{0.85}Ca_{0.15})(Zr_{0.1}Ti_{0.9})O_3$–$CoFe_2O_4$ laminate and particulate composites, Ceram. Int. 44 (2018) 4298–4306. https://doi.org/10.1016/j.ceramint.2017.12.018.

[128] J. Zhai, N. Cai, Z. Shi, Y. Lin, C.W. Nan, Magnetic-dielectric properties of $NiFe_2O_4$/PZT particulate composites, J. Phys. D. Appl. Phys. 37 (2004) 823–827. https://doi.org/10.1088/0022-3727/37/6/002.

[129] Y. Shi, Y.W. Gao, Theoretical study on nonlinear magnetoelectric effect and harmonic distortion behavior in laminated composite, J. Alloys Compd. 646 (2015) 351–359. https://doi.org/10.1016/j.jallcom.2015.05.229.

[130] T.Z. Wang, Y.H. Zhou, A theoretical study of nonlinear magnetoelectric effect in

magnetostrictive-piezoelectric trilayer, Compos. Struct. 93 (2011) 1485–1492. https://doi.org/10.1016/j.compstruct.2010.12.003.

[131] I. Bichurin, A. Filippov, M. Petrov, M. Laletsin, N. Paddubnaya, G. Srinivasan, Resonance magnetoelectric effects in layered magnetostrictive-piezoelectric composites, Phys. Rev. B - Condens. Matter Mater. Phys. 68 (2003) 10–13. https://doi.org/10.1103/PhysRevB.68.132408.

[132] P. Pahuja, C. Prakash, R.P. Tandon, Comparative study of magnetoelectric composite system $Ba_{0.95}Sr_{0.05}TiO_3$-$Ni_{0.8}Co_{0.2}Fe_2O_4$ with ferrite prepared by different methods, Ceram. Int. 40 (2014) 5731–5743. https://doi.org/10.1016/j.ceramint.2013.11.012.

[133] J. Kreiselt, A.M. Glazer, G. Jones, P.A. Thomas, L. Abello, G. Lucazeau, An x-ray diffraction and Raman spectroscopy investigation of A-site substituted perovskite compounds: The $(Na_{1-x}K_x)_{0.5}Bi_{0.5}TiO_3$ ($0 \leq x \leq 1$) solid solution, J. Phys. Condens. Matter. 12 (2000) 3267–3280. https://doi.org/10.1088/0953-8984/12/14/305.

[134] J. Petzelt, T. Ostapchuk, I. Gregora, P. Kuzel, J. Liu, Z. Shen, Infrared and Raman studies of the dead grain-boundary layers in $SrTiO_3$ fine-grain ceramics, J. Phys. Condens. Matter. 19 (2007). https://doi.org/10.1088/0953-8984/19/19/196222.

[135] N. Yousefi, X. Sun, X. Lin, X. Shen, J. Jia, B. Zhang, B. Tang, M. Chan, J.K. Kim, Highly aligned graphene/polymer nanocomposites with excellent dielectric properties for high-performance electromagnetic interference shielding, Adv. Mater. 26 (2014) 5480–5487. https://doi.org/10.1002/adma.201305293.

[136] G.W. Dietz, W. Antpöhler, M. Klee, R. Waser, Electrode influence on the charge transport through $SrTiO_3$ thin films, J. Appl. Phys. 78 (1995) 6113–6121. https://doi.org/10.1063/1.360553.

[137] G. Li, X. Wu, W. Ren, P. Shi, Effect of excessive K and Na on the dielectric properties of $(K,Na)NbO_3$ thin films, Thin Solid Films. 548 (2013) 556–559. https://doi.org/10.1016/j.tsf.2013.09.027.

[138] T. Karthik, S. Rayaprol, V. Siruguri, S. Asthana, Origin of enhanced piezoelectric properties revealed through electric field driven studies in $0.94(Na_{0.5}Bi_{0.5}TiO_3)$-$0.06(Ba_{0.85}Ca_{0.15}Ti_{0.9}Zr_{0.1}O_3)$ ceramics, J. Appl. Phys. 127 (2020) 0–11. https://doi.org/10.1063/1.5136293.

[139] N. Masaki, S. Uchida, H. Yamane, T. Sato, Hydrothermal synthesis of potassium titanates in Ti-KOH-H_2O system, J. Mater. Sci. 35 (2000) 3307–3311. https://doi.org/10.1023/A:1004835724752.

[140] S. Sayyad, S. Acharya, Low temperature synthesis of complex solid solution (1-x) $Bi_{0.5}Na_{0.5}TiO_3$–x$BaTiO_3$ system: BT induced structural and dielectric anomalies in NBT, Ferroelectrics. 537 (2018) 112–132. https://doi.org/10.1080/00150193.2018.1528950.

[141] S. Pachari, S.K. Pratihar, B.B. Nayak, Microstructure driven magnetodielectric behavior in ex-situ combustion derived $BaTiO_3$-ferrite multiferroic composites, J. Magn. Magn. Mater. 505 (2020) 1–10. https://doi.org/10.1016/j.jmmm.2020.166741.

[142] S.S.N. Bharadwaja, S.B. Krupanidhi, Backward switching phenomenon from field forced ferroelectric to antiferroelectric phases in antiferroelectric $PbZrO_3$ thin films, J. Appl. Phys. 89 (2001) 4541–4547. https://doi.org/10.1063/1.1331659.

[143] J. Wu, A. Mahajan, L. Riekehr, H. Zhang, B. Yang, N. Meng, Z. Zhang, H. Yan, Perovskite $Sr_x(Bi_{1-x}Na_{0.97-x}Li_{0.03})_{0.5}TiO_3$ ceramics with polar nano regions for high power energy storage, Nano Energy. 50 (2018) 723–732. https://doi.org/10.1016/j.nanoen.2018.06.016.

[144] Y. Jia, H. Fan, A. Zhang, H. Wang, L. Lei, Q. Quan, G. Dong, W. Wang, Q. Li, Giant electro-induced strain in lead-free relaxor ferroelectrics via defect engineering, J. Eur. Ceram. Soc. 43 (2023) 947–956. https://doi.org/10.1016/j.jeurceramsoc.2022.10.058.

[145] J. Jadhav, S. Biswas, A.K. Yadav, S.N. Jha, D. Bhattacharyya, Structural and magnetic properties of nanocrystalline Ni-Zn ferrites: In the context of cationic distribution, J. Alloys Compd. 696 (2017) 28–41. https://doi.org/10.1016/j.jallcom.2016.11.163.

[146] P. Xvli, V. Onderzoek, D.N.V.P. Gloeilampcnfabrieken, THE MAGNETIZATION PROCESS IN FERRITES, (1951) 976–992.

[147] N.S.S. Murthy, M.G. Natera, S.I. Youssef, R.J. Begum, C.M. Srivastava, Yafet-kittel angles in zinc-nickel ferrites, Phys. Rev. 181 (1969) 969–977. https://doi.org/10.1103/PhysRev.181.969.

[148] A.C.F.M. Costa, V.J. Silva, D.R. Cornejo, M.R. Morelli, R.H.G.A. Kiminami, L. Gama, Magnetic and structural properties of $NiFe_2O_4$ ferrite nanopowder doped with Zn^{2+}, J. Magn. Magn. Mater. 320 (2008) 370–372. https://doi.org/10.1016/j.jmmm.2008.02.159.

[149] M.A. Gabal, Y.M. Al Angari, Effect of diamagnetic substitution on the structural, magnetic and electrical properties of $NiFe_2O_4$, Mater. Chem. Phys. 115 (2009) 578–584. https://doi.org/10.1016/j.matchemphys.2008.12.032.

[150] A.S. Albuquerque, J.D. Ardisson, W.A.A. Macedo, M.C.M. Alves, Nanosized powders of NiZn ferrite: Synthesis, structure, and magnetism, J. Appl. Phys. 87 (2000) 4352–

4357. https://doi.org/10.1063/1.373077.

[151] M.K. Niranjan, T. Karthik, S. Asthana, J. Pan, U. V. Waghmare, Theoretical and experimental investigation of Raman modes, ferroelectric and dielectric properties of relaxor $Na_{0.5}Bi_{0.5}TiO_3$, J. Appl. Phys. 113 (2013) 1–7. https://doi.org/10.1063/1.4804940.

[152] M. Sahu, T. Karthik, A. Srinivas, S. Asthana, Structural and microstructural correlation with ferroelectric and dielectric properties of nanostructured $Na_{0.5}Bi_{0.5}TiO_3$ ceramics, J. Mater. Sci. Mater. Electron. 26 (2015) 9741–9746. https://doi.org/10.1007/s10854-015-3643-6.

[153] S. Thakur, K. Parmar, S. Sharma, N.S. Negi, Structural, Magnetic, and Electrical Properties of $(1-x)Na_{0.5}Bi_{0.5}TiO_3$–$(x)NiFe_2O_4$ (x = 0.1, 0.3, 0.5, 0.7, and 0.9) Multiferroic Particulate Composite, J. Supercond. Nov. Magn. 4 (2020) 1–7. https://doi.org/10.1007/s10948-020-05696-8.

[154] C.G. Koops, On the dispersion of resistivity and dielectric constant of some semiconductors at audiofrequencies, Phys. Rev. 83 (1951) 121–124. https://doi.org/10.1103/PhysRev.83.121.

[155] M.V. Reddy, J.P. Paul, N.S. Sowmya, A. Srinivas, D. Das, Magneto-electric properties of in-situ prepared $xCoFe_2O_4$-$(1-x)(Ba_{0.85}Ca_{0.15})(Zr_{0.1}Ti_{0.9})O_3$ particulate composites, Ceram. Int. 42 (2016) 17827–17833. https://doi.org/10.1016/j.ceramint.2016.08.112.

[156] C.P. Fernández, F.L. Zabotto, D. Garcia, R.H.G.A. Kiminami, In situ sol–gel co-synthesis under controlled pH and microwave sintering of PZT/$CoFe_2O_4$ magnetoelectric composite ceramics, Ceram. Int. 42 (2016) 3239–3249. https://doi.org/10.1016/j.ceramint.2015.10.115.

[157] C.E. Ciomaga, M. Airimioaei, V. Nica, L.M. Hrib, O.F. Caltun, A.R. Iordan, C. Galassi, L. Mitoseriu, M.N. Palamaru, Preparation and magnetoelectric properties of $NiFe_2O_4$-PZT composites obtained in-situ by gel-combustion method, J. Eur. Ceram. Soc. 32 (2012) 3325–3337. https://doi.org/10.1016/j.jeurceramsoc.2012.03.041.

[158] S. Liu, L. Deng, S. Yan, H. Luo, L. Yao, L. He, Y. Li, M. Wu, S. Huang, Magnetoelectric properties of lead-free $(80Bi_{0.5}Na_{0.5}TiO_3$-$20Bi_{0.5}K_{0.5}TiO_3)$-$Ni_{0.8}Zn_{0.2}Fe_2O_4$ particulate composites prepared by in situ sol-gel, J. Appl. Phys. 457 (2014) 356–359. https://doi.org/10.7868/s0869565214210269.

[159] I. Coondoo, Magnetoelectric coupling studies in lead-free multiferroic $(Ba_{0.85}Ca_{0.15})(Zr_{0.1}Ti_{0.9})O_3$–$(Ni_{0.7}Zn_{0.3})Fe_2O_4$ ceramic composites, Ceram. Int. 48 (2022) 24439–

24453.

[160] R.A. Islam, S. Priya, Effect of piezoelectric grain size on magnetoelectric coefficient of $Pb(Zr_{0.52}Ti_{0.48})O_3$-$Ni_{0.8}Zn_{0.2}Fe_2O_4$ particulate composites, J. Mater. Sci. 43 (2008) 3560–3568. https://doi.org/10.1007/s10853-008-2562-9.

[161] W.S. Rosa, M. Venet, Exploring the processing conditions to optimize the interface in 2-2 composites based on $Pb(Zr,Ti)O_3$ and $NiFe_2O_4$, Ceram. Int. 42 (2016) 7980–7986. https://doi.org/10.1016/j.ceramint.2016.01.196.

[162] Y. Wang, Y. Pu, Y. Tian, X. Li, Z. Wang, Y. Shi, J. Zhang, G. Zhang, Enhanced magnetoelectric properties of the laminated $Ba_{0.9}Ca_{0.1}Ti_{0.9}Zr_{0.1}O_3$/$Co_{0.8}Ni_{0.1}Zn_{0.1}Fe_2O_4$ composites, J. Alloys Compd. 696 (2017) 1307–1313. https://doi.org/10.1016/j.jallcom.2016.11.242.

[163] H. Yang, J. Zhang, Y. Lin, T. Wang, High Curie temperature and enhanced magnetoelectric properties of the laminated $Li_{0.058}(Na_{0.535}K_{0.48})_{0.942}NbO_3$/$Co_{0.6}Zn_{0.4}Fe_{1.7}Mn_{0.3}O_4$ composites, Sci. Rep. 7 (2017) 1–10. https://doi.org/10.1038/srep44855.

[164] J. Rani, V.K. Kushwaha, P.K. Patel, C. V. Tomy, Room temperature magnetoelectric properties of $[Ba(Zr_{0.2}Ti_{0.8})O_3$-$0.5(Ba_{0.7}Ca_{0.3})TiO_3]$/$Ni_{0.8}Zn_{0.2}Fe_2O_4$ bilayer thin films deposited by laser ablation, Mater. Chem. Phys. 256 (2020) 1–8. https://doi.org/10.1016/j.matchemphys.2020.123692.

[165] S. Yu, H. Huang, L. Zhou, Y. Ye, S. Ke, Structure and properties of PMN-PT/NZFO laminates and composites, Ceram. Int. 34 (2008) 701–704. https://doi.org/10.1016/j.ceramint.2007.09.011.